

**High-redshift Post-starburst Galaxies from
the Sloan Digital Sky Survey**

Petchara Pattarakijwanich

A DISSERTATION
PRESENTED TO THE FACULTY
OF PRINCETON UNIVERSITY
IN CANDIDACY FOR THE DEGREE
OF DOCTOR OF PHILOSOPHY

RECOMMENDED FOR ACCEPTANCE
BY THE DEPARTMENT OF
ASTROPHYSICAL SCIENCES

Advisers: Michael A. Strauss

September 2015

© Copyright by Petchara Pattarakijwanich, 2015.

All rights reserved.

Abstract

Post-starburst galaxies are a rare class of galaxy that show the spectral signature of recent, but not ongoing, star-formation activity, and are thought to have their star formation suddenly quenched within the one billion years preceding the observations. In other words, these are galaxies in the transitional stage between blue, star-forming galaxies and red, quiescent galaxies, and therefore hold important information regarding our understanding of galaxy evolution. This class of objects can be used to study the mechanisms responsible for star-formation quenching, which is an important unsettled question in galaxy evolution.

In this thesis, we study this class of galaxies through a number of different approaches. First of all, we systematically selected a large, statistical sample of post-starburst galaxies from the spectroscopic dataset of the Sloan Digital Sky Survey (SDSS). This sample contains 13219 objects in total, with redshifts ranging from local universe to $z \sim 1.3$ and median redshift $z_{\text{median}} = 0.59$. This is currently the largest sample of post-starburst galaxies available in the literature.

Using this sample, we calculated the luminosity functions for a number of redshift bins. A rapid downsizing redshift evolution of the luminosity function is observed, whereby the number density of post-starburst galaxies at fixed luminosity is larger at higher redshift. From the luminosity functions, we calculated the amount of star-formation quenching accounted for in post-starburst galaxies, and compared to the amount required by the global decline of star-formation rate of the universe. We found that only a small fraction ($\sim 0.2\%$) of all star-formation quenching in the universe goes through the post-starburst galaxy channel, at least for the luminous sources in our sample.

We also searched the SDSS spectroscopic database the post-starburst quasars, which are an even more special class of objects that show both a post-starburst stellar population and AGN activity in the same object. Given that AGN feedback is thought to be a likely mechanism responsible for quenching star-formation, post-starburst quasars provide ideal laboratory for

studying this link. We explored various ways to identify post-starburst quasars, and construct our sample with more than 600 objects at high-redshift. This is the largest sample of post-starburst quasars available in the literature, and will be useful for AGN feedback studies.

Finally, we studied the clustering properties of post-starburst galaxies through cross-correlation with CMASS galaxies. The real-space cross correlation function is a power-law with correlation length $r_0 \sim 9.2$ Mpc, and power-law index $\gamma \sim 1.8$. We also measure the linear bias of post-starburst galaxies to be $b_{\text{PSG}} \sim 1.74$ at redshift $z = 0.62$, corresponding to a dark matter halo mass of $M_{\text{halo}} \sim 1.5 \times 10^{13} M_{\odot}$. We found no evidence for redshift evolution in clustering properties for post-starburst galaxies.

Acknowledgments

First of all, I would like to express my sincere gratitude to my advisor, Prof. Michael Strauss, for his continuous support throughout the years. Without his guidance, motivation, patience and immense knowledge, this thesis would not have been possible. I could not imagine having a better Ph.D. advisor than this.

Besides my advisor, I would also like to thank the rest of my thesis committee, Prof. Jim Gunn, Prof. Jenny Greene, Dr. Robert Lupton and Dr. Renyue Cen, for their advice and encouragement. Their insights have widened my perspectives and motivated countless ideas.

I am deeply grateful to Prof. Jill Knapp and Prof. Jenny Greene, for being wonderful Directors of Graduate Studies. On top of their duty to make sure that us graduate students make satisfactory academic progress, they work tirelessly to ensure that, more importantly, we are being happy. I also want to thank the faculty and staff of this department in general for the supportive, welcoming and intellectually stimulating atmosphere in this department that they have collectively created.

Despite the amazing support I received from my advisor and the department, completing a Ph.D. thesis is naturally a difficult process, with endless stress, self-doubt, frustration and disappointment. I managed to survive this, in large part, thanks to the support from fellow graduate students, and a number of undergraduates and visiting students, with whom I was fortunate enough to spend time with in the windowless basement of Peyton Hall. I would like to thank them for their endless willingness to listen to and encourage me, and for all the fun we shared. Their friendship and company make the bad times a little more endurable, and the good times even more memorable.

Another group of friends that have been a big part of my life in Princeton is the small community of Thai students here. I would like to thank them for all the good times we shared at the Thai table and elsewhere, and for making me feel a little more at home. While it is difficult to

find any US college with smaller Thai community than Princeton, it is even more difficult to find anywhere with a warmer and more closely-connected Thai community than this one.

For the past three years, I took Japanese language classes with the Department of East Asian Studies, for no particular reason other than fun and my personal interest in Japanese Anime and Manga. I would like to thank the teachers in the Japanese Language Program for their fascinating classes, and my classmates for all the fun and pleasant struggles we shared while learning the language. I would also like to thank the Anime-Manga club at Princeton and its members, who, not surprisingly, are mostly also classmates in the Japanese classes, for the fun activities they organized throughout the years. Learning Japanese language, although somewhat time-consuming, has been very enjoyable and rewarding, and will certainly be continued.

I was fortunate enough to have made a number of good friends throughout school and college years. Although we drifted apart as lives moved on, it is reassuring to know that their support will always come pouring in any time of need, across vast distances and many time zones. I also enjoy the infrequent but meaningful conversations and meetings we have had, and hope they will continue for a long time to come, just like our friendships.

While all friends, colleagues, teachers and mentors I have been fortunate enough to meet have contributed in some way in shaping me into the person I am now, two people were particularly influential. I would like to thank my middle school science teacher, Ms. Mantanee Tantisewee and my then high school principal, Dr. Thongchai Chewprecha, for fostering and supporting my love for sciences. For some reasons, science is not a popular college major in Thailand, and students choosing it over medicine or engineering will face enormous social pressure. Without their encouragement, I would have made a very different life choice and would never have discovered the joy of astrophysics.

I am deeply honored and privileged to have been awarded the Development and Promotion of Science and Technology Talent Project (DPST) Scholarship by the Royal Thai Government. This opportunity to study abroad in prestigious, world-class universities would not have been imaginable without the support from this program. I will make sure that my end of the contract – to return to and advance my home country – is fulfilled.

Finally, I would like to thank my parents and my sister, Mr. Permsin, Mrs. Narumon and Miss. Pattarin Pattarakijwanich, for being the best family I could ever have. Without their influence as role models, their encouragement and their everlasting support in anything I do, this thesis, and whatever success I have ever accomplished in life, would not have been possible.

Preface

This thesis is organized into five chapters, including introduction, and is based on a paper that has been submitted to The Astrophysical Journal and a collection of unpublished works. Chapter 1 is a general introduction to the field. Chapter 2 is based on the said paper (first author) which has been submitted to the Astrophysical Journal for publication and is in the middle of review process. Chapter 3 through Chapter 5 are based on unpublished works. The results from Chapter 2 have been presented at the SDSS Collaboration Meeting in Park City, Utah in July 2014. The works presented in every chapter of this thesis used the data from the Sloan Digital Sky Survey (SDSS) as a primary source of data.

Funding for SDSS-III has been provided by the Alfred P. Sloan Foundation, the Participating Institutions, the National Science Foundation, and the U.S. Department of Energy Office of Science. The SDSS-III web site is <http://www.sdss3.org/>.

SDSS-III is managed by the Astrophysical Research Consortium for the Participating Institutions of the SDSS-III Collaboration including the University of Arizona, the Brazilian Participation Group, Brookhaven National Laboratory, Carnegie Mellon University, University of Florida, the French Participation Group, the German Participation Group, Harvard University, the Instituto de Astrofisica de Canarias, the Michigan State/Notre Dame/JINA Participation Group, Johns Hopkins University, Lawrence Berkeley National Laboratory, Max Planck Institute for Astrophysics, Max Planck Institute for Extraterrestrial Physics, New Mexico State University, New York University, Ohio State University, Pennsylvania State University, University of Portsmouth, Princeton University, the Spanish Participation Group, University of Tokyo,

University of Utah, Vanderbilt University, University of Virginia, University of Washington, and Yale University.

Chapter 1

This chapter is a general introduction to the field, surveying the literature broadly, and highlighting all relevant past works regarding various aspects of post-starburst galaxy studies. This was originally written as the introduction to a paper that eventually became the material presented in Chapter 2, and was shortened significantly in response to the referee's suggestion to only keep relevant materials. The introduction presented here is taken from the version prior to the shortening, and is intended to have broader coverage. It has been modified to include more recent references to be up-to-date at the time of thesis submission.

Chapter 2

This chapter presents the post-starburst galaxy selection, post-starburst galaxy luminosity function and its redshift evolution. These are the results presented in the paper Pattarakijwanich et al. (2014), which I am the lead author and is co-authored by Michael Strauss, Shirley Ho and Nicholas Ross. This paper has been submitted for publication in *The Astrophysical Journal* and is currently under review. The co-authors contributed ideas and discussions, but the vast majority of calculations and writings are done by me. All co-authors have approved the use of this work as part of this thesis. Part of the data used in this paper is based on observations obtained with the Apache Point Observatory 3.5-meter telescope, which is owned and operated by the Astrophysical Research Consortium.

Chapter 3

This chapter presents an updated post-starburst galaxy sample selection and luminosity function. The methods used in this chapter are mostly similar to those used in chapter 2, but are applied to larger dataset from the Sloan Digital Sky Survey that has become available since the

time of writing of Pattarakijwanich et al. (2014). This work is not yet published. All calculations and writings in this chapter are done by me.

Chapter 4

This chapter presents an attempt at selecting post-starburst quasars from the SDSS spectroscopic database. Various different approaches in post-starburst quasar selection are explored, and the final samples are presented. This work is not yet published. All calculations and writings in this chapter are done by me.

Chapter 5

This chapter presents the clustering analysis of post-starburst galaxies, through cross-correlation with the SDSS-III BOSS CMASS galaxy population. The linear bias factor, and the corresponding dark matter halo mass of post-starburst galaxies are calculated. This work is not yet published. All calculations and writings in this chapter are done by me.

Bibliography

Pattarakijwanich, P., Strauss, M. A., Ho, S., & Ross, N. P. 2014, ArXiv e-prints

Contents

Abstract	iii
Acknowledgments	v
Preface	viii
Bibliography	x
1 Introduction	1
Bibliography	9
2 The Evolution of Post-Starburst Galaxies from $z \sim 1$ to the Present	16
1 Introduction	17
2 Data	21
2.1 SDSS and BOSS Surveys	21
2.2 SDSS Magnitude System	22
2.3 Small Sample of Post-Starburst Galaxies	22
3 Selection of post-starburst galaxies	23
3.1 Spectral Templates	23
3.2 Selection Methods	23
4 Sample Properties	30
4.1 Coadded Spectra	31
4.2 Spectroscopic Target Selection	38
4.3 Comparison to the Pipeline Redshifts	40
4.4 H α Equivalent Width	43
4.5 Potential Biases in Selection	47

5	Luminosity Function	48
5.1	Synthetic Spectrophotometry	48
5.2	Magnitude and Color in Fiducial Bands	49
5.3	SDSS Main Galaxy Sample	51
5.4	BOSS CMASS Sample	53
5.5	Self-Consistency Test of Luminosity Function from the BOSS CMASS Sample	64
5.6	Comparison to Global Star Formation Rate	69
6	Discussion	72
6.1	Sample	72
6.2	Evolution of the Luminosity Function	74
6.3	Mechanisms Responsible for Quenching	76
6.4	Improvement to Selection Method	78
7	Conclusion	79
	Bibliography	82
3	Post-starburst Galaxies from DR12	98
1	Introduction	98
2	Modified Selection Method	99
3	Sample	100
4	Luminosity Function	101
	Bibliography	103
4	Search for Post-starburst Quasars	109
1	Introduction	109
2	Post-starburst Quasar Selection	111
2.1	Search for Post-starburst Quasars from the Post-starburst Galaxy Sample . .	112
2.2	Search for Post-starburst Quasars from the SDSS Quasar Catalog	118
2.3	Search for Post-starburst Quasars from the SDSS-III BOSS Spectroscopic Database	120

3	Comparing Different Post-starburst Quasar Samples	122
4	SDSS J125942.80+121312.5: A Quasar with Strange Spectroscopic Properties	126
5	Discussions and Conclusions	131
	Bibliography	132
5	Clustering Analysis of Post-starburst Galaxies	135
1	Introduction	135
2	Sample	137
3	Cross-correlation Function	140
3.1	Redshift-space Cross-correlation Function	140
3.2	Semi-projected Cross-correlation Function	140
3.3	Real-space Correlation Function	144
4	Evolution of Clustering Properties with Redshift	145
5	Bias and Dark Matter Halo Mass	150
6	Discussion and Conclusions	152
	Bibliography	154

Introduction

Post-starburst galaxies were first identified by Dressler & Gunn (1983) as a distinct class of galaxies. Their main spectroscopic characteristics are strong Balmer absorption lines with a lack of emission lines due to star formation. The physical explanation of these properties is that these galaxies had a large burst of star formation about 10^{8-9} years before the observation that suddenly was quenched, with very little ongoing star formation. This stellar population is old enough that the short-lived O- and B-stars have all died (thus no nebular emission lines), and young enough that the optical spectrum is dominated by A-stars (thus the strong Balmer absorption). Given the stellar population properties, one possible explanation is that these objects are in a transitional stage between star-forming blue cloud galaxies and quiescent red sequence galaxies.

The global star formation rate over the entire universe is found to have dropped by about an order of magnitude since redshift $z \sim 1$ (Madau & Dickinson, 2014). This implies that the galaxy population changed drastically between redshift $z \sim 1$ and the present time. The heavily star-forming galaxies that are abundant at high redshift must be quenched and evolve to the red, passive elliptical galaxies. If this quenching is sudden, then they will pass through the post-starburst phase in between. Therefore, we expect that the post-starburst galaxy population in this redshift range would reflect this change in the global star formation rate. In order to understand this, one needs a large, statistical sample of post-starburst galaxies that are selected with a uniform and well-understood selection method across this large range of redshift.

The terminology in post-starburst galaxy studies is rather rich and confusing. There are three common names found in the literature for this type of galaxy: “Post-starburst”, “E+A” and “K+A”. The names “E+A” and “K+A” come from the fact that the spectra of these galaxies can

be decomposed into a linear combination of an “A”-star spectrum and the spectrum of the old population, denoted either by “E” for elliptical galaxy or “K” for K-giant star, which is the dominant component of light from elliptical galaxies. Some authors have also defined a number of subclasses such as E+a (Choi et al., 2009) and post-quenching (Quintero et al., 2004). This is closely related to the “green valley” galaxies that lie between the blue cloud and the red sequence in the color-magnitude diagram, although not all green valley galaxies have the spectroscopic signature of post-starburst galaxies (Wong et al., 2012). In this thesis we will make no distinction between these names and just call all objects with strong Balmer absorption and weak emission lines “post-starburst”.

Two main scenarios have been proposed to explain the formation of post-starburst galaxies, which predict different detailed properties of these galaxies. While it is likely that both mechanisms contribute to the formation of post-starburst galaxies to some degree, the relative importance of the two mechanisms is far from clear. Moreover, the relative importance of each mechanism can potentially be a function of redshift and galaxy mass.

The first scenario is a cluster-related mechanism such as ram-pressure stripping. In this picture, gas-rich star-forming galaxies fall into galaxy clusters and their gas is removed by the interaction with the hot intra-cluster medium, suddenly quenching their star formation (Gunn & Gott, 1972; Balogh et al., 2000). According to this scenario, the resulting post-starburst galaxies would be found predominantly in dense environments such as galaxy groups and clusters. They would still resemble disk galaxies, since nothing apart from gas loss would disturb their morphology. This idea was first proposed by Dressler & Gunn (1983) because the first post-starburst galaxies they found were in clusters, and they therefore hypothesized that these objects lay exclusively in overdense region. It was only found later that these objects are also present in the field (Zabludoff et al., 1996; Quintero et al., 2004; Blake et al., 2004). This scenario is also proposed as a possible way to form S0 galaxies.

The other camp proposes that post-starburst galaxies are associated with galaxy interactions, mergers or AGN feedback. In this scenario, when gas-rich galaxies go through a merger phase, the gas is disturbed and collapses to form stars, leading to a large scale starburst. The same

disturbance also funnels the gas to the galactic center, resulting in both a central starburst and AGN activity. The galaxy then either runs out of gas and stops forming stars, or the rest of the gas receives enough heating from either supernova or AGN feedback that it becomes too hot to collapse further or is expelled altogether. Either way, the galaxy goes through a starburst phase that stops quickly. This picture makes a number of predictions about the properties of post-starburst galaxies. The first is that it naturally explains the observations of post-starburst galaxies in lower density regions such as poor groups and the field. Their morphologies should show prominent signs of recent interactions such as tidal tails (Zabludoff et al., 1996; Yang et al., 2004, 2008; Blake et al., 2004; Tran et al., 2004; Goto, 2005). Post-starburst galaxies might also generally coincide with AGN in the central supermassive black hole, since both starburst and AGN activity are likely triggered by the same mechanisms, although these processes might work on different timescales. Also, the post-starburst stellar population is predicted to be centrally concentrated in their galaxies because the gas is driven toward the center in a merger, making the post-starburst galaxies appear more compact than elliptical galaxies at similar redshift. Observations show that this indeed is the case (Pracy et al., 2012; Swinbank et al., 2011; Whitaker et al., 2012).

The picture that gas-rich mergers drive both star formation and AGN activity is supported by theoretical work as early as, for example, Sanders et al. (1988) and Mihos & Hernquist (1994). More recent simulation work that studies this scenario includes, for example, Hopkins et al. (2006, 2008); Bekki et al. (2001, 2005, 2010) and Snyder et al. (2011). Their models suggest that the spectra of the merging systems start with strong Balmer absorption with a moderate amount of emission lines, then go through a post-starburst phase when the emission lines fade out. After about 1 Gyr, after the A-stars fade, the galaxy becomes dominated by an elliptical-like population.

There are also other models that attempt to explain this post-starburst phenomenon. Miller & Owen (2001) suggest that post-starburst galaxies are in fact dust-enshrouded starburst galaxies. In this picture, the ongoing star formation is hidden behind a large amount of dust and gas and therefore the emission lines are completely extincted. Balmer absorption lines, on the other hand,

originate from A stars, which are long-lived enough to migrate out of the star-forming gas cloud and become visible. This idea can be tested at far-infrared or radio continuum wavelengths, at which one can measure the star formation rate independent of dust and gas extinction. Various authors have carried out this test and the conclusion is that even though a small number of post-starburst galaxies may include dust-enshrouded starbursts, this model does not explain the majority of the post-starburst galaxy population (Miller & Owen, 2001; Goto, 2004; Chang et al., 2001; Nielsen et al., 2012).

With these pictures in mind, various authors have studied various aspects of post-starburst galaxies. The results of these observations are reviewed below.

The first important aspect is the selection of the sample itself. Post-starburst galaxies are typically selected spectroscopically, with the requirement that the Balmer absorption, usually represented by $H\delta$, is strong. $H\delta$ absorption is commonly used for this because nebular gas emission from star formation tends to be quite weak in this line, unlike $H\alpha$ or $H\beta$. It also does not have other major lines in its immediate vicinity, making the equivalent width measurement easy. The nebular emission lines, commonly represented by $H\alpha$ and $[OII]\lambda 3727$, are required to be weak. Goto (2005, 2007) selected ~ 500 low-redshift post-starburst galaxies from the Sloan Digital Sky Survey (SDSS; York et al. (2000)). The cuts used in Goto (2005, 2007) were based on rest-frame Equivalent Width (EW) as follows: $H\alpha EW < -2.5\text{\AA}$, $H\delta EW > 5\text{\AA}$ and $[OII]\lambda 3727 EW < -3\text{\AA}$. Various authors have used different values for these thresholds to select post-starburst galaxies. For objects at higher redshift, $H\alpha$ drops out of the wavelength coverage of optical instruments and therefore the selection is usually done on the $H\delta$ and $[OII]$ lines alone. Yan et al. (2006) pointed out that the selection based on these two lines might be incomplete because many post-starburst galaxies may have significant $[OII]$ emission from LINERs, leading to their exclusion from the samples, even though the line is in fact due to the central AGN and not the stellar population of the galaxy. On the other hand, there are also objects with strong $H\alpha$ emission but no $[OII]$ emission which would be selected as post-starburst galaxies if $H\alpha$ is not observable. Goto (2007) found that these extra objects included due to the lack of information about $H\alpha$ can erroneously double the size of a sample.

A number of other methods have been used to select post-starburst galaxies. Blake et al. (2004) used a combination of the absorption strength of three Balmer lines ($H\beta$, $H\gamma$ and $H\delta$ instead of relying on $H\delta$ alone). Quintero et al. (2004) fit the spectra to a linear combination of template spectra as part of their sample selection. Choi et al. (2009) explored the possibility of using the UV-optical color as a selection method for post-starburst galaxies.

Early studies of post-starburst galaxies usually had samples of only a handful of objects, too small to represent a statistical population. More recently, however, post-starburst samples have been selected from large spectroscopic surveys. Low-redshift post-starburst galaxies have been selected from the Las Campanas Redshift Survey (Zabludoff et al., 1996), the Sloan Digital Sky Survey (Goto, 2005, 2007; Quintero et al., 2004), and the 2dF Galaxy Redshift Survey (Blake et al., 2004) with samples numbering usually in hundreds. At high redshifts, $z \sim 0.8$ post-starburst galaxies have been selected from the DEEP2 survey (Yan et al., 2009) and the zCOSMOS survey (Vergani et al., 2010) with samples of a few tens of objects. These large samples are very important to understand the properties of the population as a whole.

The global properties of the sample can give insights about the physical nature of these objects. Blake et al. (2004) found that the luminosity function of this population is similar to that of elliptical galaxies. Krause et al. (2013) studied the clustering of the green valley galaxies and found that the satellite fraction and characteristic halo mass of this population are intermediate to those of red and blue galaxies. The environments in which the post-starburst galaxies live can be quantified in terms of the number of neighbors on different length scales (Zabludoff et al., 1996; Galaz, 2000; Blake et al., 2004; Balogh et al., 2005; Hogg et al., 2006; Yan et al., 2009; Poggianti et al., 2009). The individual results of this environmental studies vary and are hard to compare due to different sample selection, but it is clear that the post-starburst galaxies exist in a wide range of environments.

More detailed studies of individual galaxies in these samples can further reveal their physical properties. The detailed morphologies can be studied using high-resolution images from the Hubble Space Telescope, or ground-based telescopes for nearby galaxies. This reveals the surface brightness profile and any features due to mergers or tidal interactions. This has been done by,

for example, Belloni (1997); Caldwell et al. (1999); Tran et al. (2003, 2004); Blake et al. (2004); Yang et al. (2004, 2008) and Cales et al. (2011). The results again vary due to small numbers of objects, but it seems that the post-starburst galaxies span a range of morphologies from being disk-like to bulgy, with a significant fraction showing signs of disturbance. Trouille et al. (2013) visually classified the morphologies of about 3000 post-starburst galaxies from SDSS, and found that those with large stellar mass ($> 10^{10.5} M_{\odot}$) are more likely to show signs of mergers in their morphologies, and also more likely to have AGN. Due to the short AGN duty cycle (10^7 years), they concluded that the AGN is triggered after the star formation is quenched, and plays a maintenance role to keep the gas hot rather than quenching the star formation itself.

The two-dimensional color profile and spatially resolved spectroscopic data can also be used to understand the distribution of stellar populations. This can distinguish whether the objects resulted from mergers (blue core) or whether the starburst and quenching happen globally (no color gradient). Caldwell et al. (1996) studied a number of long slit spectra of post-starburst galaxies in the Coma cluster. It was found that the objects have rotation and surface brightness profiles consistent with being a disk. The post-starburst stellar population is distributed over a large range of radii. This gives support to the picture that the quenching is due to interaction with the galaxy clusters. Norton et al. (2001); Goto (2005) and Yagi & Goto (2006) found similarly that the post-starburst stellar population is distributed throughout the galaxy, indicating that the quenching is a global phenomenon related to the evolution of these galaxies. However, Yang et al. (2008) used two-band HST photometry to show that a small, but not negligible fraction of post-starburst galaxies have blue cores, suggesting that a central starburst happens in some cases. Pracy et al. (2005, 2009, 2010, 2012, 2013); Goto et al. (2008) and Swinbank et al. (2011) obtained integral field spectra of a number of post-starburst galaxies. Their results showed various behaviors, with the post-starburst stellar population concentrating at the core for some objects, and distributed throughout the galaxy for others. They also found that a significant fraction of post-starburst galaxies are fast rotators, which disfavors the picture that post-starburst galaxies are caused by major mergers. These IFU studies tend not to probe the outer parts of galaxies due to the small field of view of the IFU. Moreover, spatially resolved

spectra of post-starburst galaxies have only been obtained for a small number of objects, and any interpretation of the results are limited by small number statistics.

The study of gas properties in post-starburst galaxies is also important in many aspects. The dense neutral gas is the potential fuel for star formation, while the hot, ionized gas can give clues on feedback. This line of study started with Israel & van Driel (1990), who obtained an HI column density map for a local post-starburst galaxy. They found a hole approximately 200 pc across near the center of the galaxy which was thought to host a luminous star cluster. This hole is likely due to feedback from this central object. Rubin et al. (2010) inferred a significant amount of cold gas in the halo at large transverse distance of 16.5 kpc from a post-starburst galaxy, by absorption imprinted in the background galaxy spectrum. A likely scenario is that this cold gas was stripped and driven out of the post-starburst galaxy during the recent starburst episode. Zwaan et al. (2013) and French et al. (2015) detected a large amount of gas, comparable to star-forming galaxies, in tens of local post-starburst galaxies (in HI and CO respectively). It is unclear how these post-starburst galaxies have low star-formation rate despite a significant amount of gas available. A possible explanation is given by Kohno et al. (2002), who observed another local post-starburst galaxy in sub-millimeter wavelengths to obtain CO and HCN maps, and found a lack of dense molecular gas (indicated by low HCN/CO) in this post-starburst galaxy compared to typical starburst galaxies. This suggests that star formation might be quenched despite a large amount of gas available, as long as the dense molecular gas core is destroyed by some feedback mechanism.

Post-starburst galaxies often show outflows, indicated by blue-shifted metal absorption lines. The lines commonly used are MgI, MgII and FeII, which are only visible in the optical spectra for moderately high redshift galaxies. The outflow velocity can shed light on the process driving the outflow itself, which is likely related to the feedback process that quenches the star formation in the galaxy in the first place. Tripp et al. (2011) used UV absorption spectroscopy to measure the mass in the warm and hot phase in the outflows from post-starburst galaxies and found that a significant amount of mass is removed from these post-starburst galaxies through this phase. Coil et al. (2011) studied the outflow in a sample of several post-starburst galaxies in the redshift

range $0.2 < z < 0.8$ and found that the outflow is present in most objects, but the speed is low and is more consistent with supernova and not AGN. Tremonti et al. (2007), on the other hand, discovered several post-starburst galaxies at similar redshift with outflow velocities of ~ 1000 km/s, presumably driven out in the recent past from the central supermassive black hole at the peak of its AGN activity.

Another interesting aspect of the study of post-starburst galaxies is the relation of the phenomenon with nuclear activity. We observe this relationship in a class of objects called “post-starburst quasars”, which show the spectroscopic signature of both a post-starburst galaxy and AGN activity. This relationship is expected in the interaction/merger scenario because the same disturbance that creates large starbursts will also direct gas to the center of the galaxy to fuel the supermassive black hole. Also, the AGN feedback is thought to be responsible for the star-formation quenching in galaxies. Therefore the post-starburst quasars should provide an ideal laboratory for studying this relationship directly. The prototype of post-starburst quasars was first identified by Brotherton et al. (1999) and studied in more detail in Brotherton et al. (2002) and Canalizo et al. (2000). This object was found to have disturbed morphology and a merging companion, suggesting that the merger is the trigger to both star formation and AGN activity. Cales et al. (2011) and Cales et al. (2013) studied a sample of several tens of post-starburst quasars with HST imaging and optical spectral modeling. They found that a significant fraction of post-starburst quasars have disturbed morphologies, and that post-starburst quasars in massive elliptical host galaxies tend to have younger starburst age, brighter AGN luminosity and emission line ratio diagnostics consistent with gas ionized by AGN. This agrees with results from Brown et al. (2009), who showed that low-luminosity post-starburst galaxies rarely host AGN, while luminous ones often do, and suggested that the feedback from AGN may only be relevant for bright post-starburst galaxies. Swinbank et al. (2011) found that other properties of post-starburst galaxies do not depend on whether they are radio-loud or radio-quiet, suggesting that AGNs only have a minor effect on galaxy evolution. Shin et al. (2011) studied the timescale of these processes and found that the radio-emitting AGN is triggered after the end of the recent starburst, therefore it cannot be the main star-formation quenching mechanism.

Matsuoka et al. (2015) modeled high signal-to-noise SDSS spectra from quasars with repeated observations, and found the stellar population of the host galaxies to often be in post-starburst phase, agreeing with the overall picture.

In this thesis, we present our studies of this rich and complicated class of objects called post-starburst galaxies using various approaches. In chapter 2, we first tackle this problem at the key limitation of previous studies - small sample size - by identifying a large number of post-starburst galaxies up to high redshifts from the Sloan Digital Sky Survey (SDSS). Luminosity functions of the post-starburst galaxy population, and their redshift evolution, are also investigated in this chapter. In chapter 3, we repeat the key results from chapter 2 but using a larger amount of spectroscopic data available, which results in a factor of three increase in the sample size. In chapter 4, we present our search for post-starburst quasars, which is a special class of objects with both post-starburst stellar population and AGN activity indicated by broad line emission. These objects are ideal laboratories for studying the effects of AGN on the galaxy. In chapter 5, we present the clustering analysis of our post-starburst galaxies, where cross-correlation between post-starburst galaxies and CMASS galaxies is performed, allowing us to measure the bias and dark matter halo mass of the sample.

Bibliography

- Balogh, M. L., Miller, C., Nichol, R., Zabludoff, A., & Goto, T. 2005, MNRAS, 360, 587
- Balogh, M. L., Navarro, J. F., & Morris, S. L. 2000, ApJ, 540, 113
- Bekki, K., Couch, W. J., Shioya, Y., & Vazdekis, A. 2005, MNRAS, 359, 949
- Bekki, K., Owers, M. S., & Couch, W. J. 2010, ApJ, 718, L27
- Bekki, K., Shioya, Y., & Couch, W. J. 2001, ApJ, 547, L17
- Belloni, P. 1997, in *Galaxy Scaling Relations: Origins, Evolution and Applications*, ed. L. N. da Costa & A. Renzini, 319

- Blake, C., Pracy, M. B., Couch, W. J., Bekki, K., Lewis, I., Glazebrook, K., Baldry, I. K., Baugh, C. M., Bland-Hawthorn, J., Bridges, T., Cannon, R., Cole, S., Colless, M., Collins, C., Dalton, G., De Propris, R., Driver, S. P., Efstathiou, G., Ellis, R. S., Frenk, C. S., Jackson, C., Lahav, O., Lumsden, S., Maddox, S., Madgwick, D., Norberg, P., Peacock, J. A., Peterson, B. A., Sutherland, W., & Taylor, K. 2004, *MNRAS*, 355, 713
- Brotherton, M. S., Grabelsky, M., Canalizo, G., van Breugel, W., Filippenko, A. V., Croom, S., Boyle, B., & Shanks, T. 2002, *PASP*, 114, 593
- Brotherton, M. S., van Breugel, W., Stanford, S. A., Smith, R. J., Boyle, B. J., Miller, L., Shanks, T., Croom, S. M., & Filippenko, A. V. 1999, *ApJ*, 520, L87
- Brown, M. J. I., Moustakas, J., Caldwell, N., Palamara, D., Cool, R. J., Dey, A., Hickox, R. C., Jannuzi, B. T., Murray, S. S., & Zaritsky, D. 2009, *ApJ*, 703, 150
- Caldwell, N., Rose, J. A., & Dendy, K. 1999, *AJ*, 117, 140
- Caldwell, N., Rose, J. A., Franx, M., & Leonardi, A. J. 1996, *AJ*, 111, 78
- Cales, S. L., Brotherton, M. S., Shang, Z., Bennert, V. N., Canalizo, G., Stoll, R., Ganguly, R., Vanden Berk, D., Paul, C., & Diamond-Stanic, A. 2011, *ApJ*, 741, 106
- Cales, S. L., Brotherton, M. S., Shang, Z., Runnoe, J. C., DiPompeo, M. A., Bennert, V. N., Canalizo, G., Hiner, K. D., Stoll, R., Ganguly, R., & Diamond-Stanic, A. 2013, *ApJ*, 762, 90
- Canalizo, G., Stockton, A., Brotherton, M. S., & van Breugel, W. 2000, *AJ*, 119, 59
- Chang, T.-C., van Gorkom, J. H., Zabludoff, A. I., Zaritsky, D., & Mihos, J. C. 2001, *AJ*, 121, 1965
- Choi, Y., Goto, T., & Yoon, S.-J. 2009, *MNRAS*, 395, 637
- Coil, A. L., Weiner, B. J., Holz, D. E., Cooper, M. C., Yan, R., & Aird, J. 2011, *ApJ*, 743, 46
- Dressler, A. & Gunn, J. E. 1983, *ApJ*, 270, 7

- French, K. D., Yang, Y., Zabludoff, A., Narayanan, D., Shirley, Y., Walter, F., Smith, J.-D., & Tremonti, C. A. 2015, *ApJ*, 801, 1
- Galaz, G. 2000, *AJ*, 119, 2118
- Goto, T. 2004, *A&A*, 427, 125
- Goto, T. 2005, *MNRAS*, 357, 937
- Goto, T. 2007, *MNRAS*, 381, 187
- Goto, T., Yagi, M., & Yamauchi, C. 2008, *MNRAS*, 391, 700
- Gunn, J. E. & Gott, III, J. R. 1972, *ApJ*, 176, 1
- Hogg, D. W., Masjedi, M., Berlind, A. A., Blanton, M. R., Quintero, A. D., & Brinkmann, J. 2006, *ApJ*, 650, 763
- Hopkins, P. F., Hernquist, L., Cox, T. J., Di Matteo, T., Robertson, B., & Springel, V. 2006, *ApJS*, 163, 1
- Hopkins, P. F., Hernquist, L., Cox, T. J., & Kereš, D. 2008, *ApJS*, 175, 356
- Israel, F. P. & van Driel, W. 1990, *A&A*, 236, 323
- Kohno, K., Tosaki, T., Matsushita, S., Vila-Vilaó, B., Shibatsuka, T., & Kawabe, R. 2002, *PASJ*, 54, 541
- Krause, E., Hirata, C. M., Martin, C., Neill, J. D., & Wyder, T. K. 2013, *MNRAS*, 428, 2548
- Madau, P. & Dickinson, M. 2014, *ARA&A*, 52, 415
- Matsuoka, Y., Strauss, M. A., Shen, Y., Brandt, W. N., Greene, J. E., Ho, L. C., Schneider, D. P., Sun, M., & Trump, J. R. 2015, *ArXiv e-prints*
- Mihos, J. C. & Hernquist, L. 1994, *ApJ*, 431, L9
- Miller, N. A. & Owen, F. N. 2001, *ApJ*, 554, L25

- Nielsen, D. M., Ridgway, S. E., De Propris, R., & Goto, T. 2012, *ApJ*, 761, L16
- Norton, S. A., Gebhardt, K., Zabludoff, A. I., & Zaritsky, D. 2001, *ApJ*, 557, 150
- Poggianti, B. M., Aragón-Salamanca, A., Zaritsky, D., De Lucia, G., Milvang-Jensen, B., Desai, V., Jablonka, P., Halliday, C., Rudnick, G., Varela, J., Bamford, S., Best, P., Clowe, D., Noll, S., Saglia, R., Pelló, R., Simard, L., von der Linden, A., & White, S. 2009, *ApJ*, 693, 112
- Pracy, M. B., Couch, W. J., Blake, C., Bekki, K., Harrison, C., Colless, M., Kuntschner, H., & de Propris, R. 2005, *MNRAS*, 359, 1421
- Pracy, M. B., Couch, W. J., & Kuntschner, H. 2010, *PASA*, 27, 360
- Pracy, M. B., Croom, S., Sadler, E., Couch, W. J., Kuntschner, H., Bekki, K., Owers, M. S., Zwaan, M., Turner, J., & Bergmann, M. 2013, *MNRAS*, 432, 3131
- Pracy, M. B., Kuntschner, H., Couch, W. J., Blake, C., Bekki, K., & Briggs, F. 2009, *MNRAS*, 396, 1349
- Pracy, M. B., Owers, M. S., Couch, W. J., Kuntschner, H., Bekki, K., Briggs, F., Lah, P., & Zwaan, M. 2012, *MNRAS*, 420, 2232
- Quintero, A. D., Hogg, D. W., Blanton, M. R., Schlegel, D. J., Eisenstein, D. J., Gunn, J. E., Brinkmann, J., Fukugita, M., Glazebrook, K., & Goto, T. 2004, *ApJ*, 602, 190
- Rubin, K. H. R., Prochaska, J. X., Koo, D. C., Phillips, A. C., & Weiner, B. J. 2010, *ApJ*, 712, 574
- Sanders, D. B., Soifer, B. T., Elias, J. H., Madore, B. F., Matthews, K., Neugebauer, G., & Scoville, N. Z. 1988, *ApJ*, 325, 74
- Shin, M.-S., Strauss, M. A., & Tojeiro, R. 2011, *MNRAS*, 410, 1583
- Snyder, G. F., Cox, T. J., Hayward, C. C., Hernquist, L., & Jonsson, P. 2011, *ApJ*, 741, 77
- Swinbank, M., Balogh, M., Bower, R., Zabludoff, A., Lucey, J., McGee, S., Miller, C., & Nichol, R. 2011, ArXiv e-prints

- Tran, K.-V. H., Franx, M., Illingworth, G., Kelson, D. D., & van Dokkum, P. 2003, *ApJ*, 599, 865
- Tran, K.-V. H., Franx, M., Illingworth, G. D., van Dokkum, P., Kelson, D. D., & Magee, D. 2004, *ApJ*, 609, 683
- Tremonti, C. A., Moustakas, J., & Diamond-Stanic, A. M. 2007, *ApJ*, 663, L77
- Tripp, T. M., Meiring, J. D., Prochaska, J. X., Willmer, C. N. A., Howk, J. C., Werk, J. K., Jenkins, E. B., Bowen, D. V., Lehner, N., Sembach, K. R., Thom, C., & Tumlinson, J. 2011, *Science*, 334, 952
- Trouille, L., Tremonti, C. A., Chen, Y.-M., Crowley-Farenga, J., Rice, W., & Loftus, P. 2013, in *Astronomical Society of the Pacific Conference Series*, Vol. 477, *Galaxy Mergers in an Evolving Universe*, ed. W.-H. Sun, C. K. Xu, N. Z. Scoville, & D. B. Sanders, 211
- Vergani, D., Zamorani, G., Lilly, S., Lamareille, F., Halliday, C., Scodreggio, M., Vignali, C., Ciliegi, P., Bolzonella, M., Bondi, M., Kovač, K., Knobel, C., Zucca, E., Caputi, K., Pozzetti, L., Bardelli, S., Mignoli, M., Iovino, A., Carollo, C. M., Contini, T., Kneib, J.-P., Le Fèvre, O., Mainieri, V., Renzini, A., Bongiorno, A., Coppa, G., Cucciati, O., de la Torre, S., de Ravel, L., Franzetti, P., Garilli, B., Kampczyk, P., Le Borgne, J.-F., Le Brun, V., Maier, C., Pello, R., Peng, Y., Perez Montero, E., Ricciardelli, E., Silverman, J. D., Tanaka, M., Tasca, L., Tresse, L., Abbas, U., Bottini, D., Cappi, A., Cassata, P., Cimatti, A., Guzzo, L., Koekemoer, A. M., Leauthaud, A., Maccagni, D., Marinoni, C., McCracken, H. J., Memeo, P., Meneux, B., Oesch, P., Porciani, C., Scaramella, R., Capak, P., Sanders, D., Scoville, N., & Taniguchi, Y. 2010, *A&A*, 509, A42
- Whitaker, K. E., Kriek, M., van Dokkum, P. G., Bezanson, R., Brammer, G., Franx, M., & Labbé, I. 2012, *ApJ*, 745, 179
- Wong, O. I., Schawinski, K., Kaviraj, S., Masters, K. L., Nichol, R. C., Lintott, C., Keel, W. C., Darg, D., Bamford, S. P., Andreescu, D., Murray, P., Raddick, M. J., Szalay, A., Thomas, D., & Vandenberg, J. 2012, *MNRAS*, 420, 1684
- Yagi, M. & Goto, T. 2006, *AJ*, 131, 2050

- Yan, R., Newman, J. A., Faber, S. M., Coil, A. L., Cooper, M. C., Davis, M., Weiner, B. J., Gerke, B. F., & Koo, D. C. 2009, *MNRAS*, 398, 735
- Yan, R., Newman, J. A., Faber, S. M., Konidaris, N., Koo, D., & Davis, M. 2006, *ApJ*, 648, 281
- Yang, Y., Zabludoff, A. I., Zaritsky, D., Lauer, T. R., & Mihos, J. C. 2004, *ApJ*, 607, 258
- Yang, Y., Zabludoff, A. I., Zaritsky, D., & Mihos, J. C. 2008, *ApJ*, 688, 945
- York, D. G., Adelman, J., Anderson, Jr., J. E., Anderson, S. F., Annis, J., Bahcall, N. A., Bakken, J. A., Barkhouser, R., Bastian, S., Berman, E., Boroski, W. N., Bracker, S., Briegel, C., Briggs, J. W., Brinkmann, J., Brunner, R., Burles, S., Carey, L., Carr, M. A., Castander, F. J., Chen, B., Colestock, P. L., Connolly, A. J., Crocker, J. H., Csabai, I., Czarapata, P. C., Davis, J. E., Doi, M., Dombeck, T., Eisenstein, D., Ellman, N., Elms, B. R., Evans, M. L., Fan, X., Federwitz, G. R., Fiscelli, L., Friedman, S., Frieman, J. A., Fukugita, M., Gillespie, B., Gunn, J. E., Gurbani, V. K., de Haas, E., Haldeman, M., Harris, F. H., Hayes, J., Heckman, T. M., Hennessy, G. S., Hindsley, R. B., Holm, S., Holmgren, D. J., Huang, C.-h., Hull, C., Husby, D., Ichikawa, S.-I., Ichikawa, T., Ivezić, Ž., Kent, S., Kim, R. S. J., Kinney, E., Klaene, M., Kleinman, A. N., Kleinman, S., Knapp, G. R., Korienek, J., Kron, R. G., Kunszt, P. Z., Lamb, D. Q., Lee, B., Leger, R. F., Limmongkol, S., Lindenmeyer, C., Long, D. C., Loomis, C., Loveday, J., Lucinio, R., Lupton, R. H., MacKinnon, B., Mannery, E. J., Mantsch, P. M., Margon, B., McGehee, P., McKay, T. A., Meiksin, A., Merelli, A., Monet, D. G., Munn, J. A., Narayanan, V. K., Nash, T., Neilsen, E., Neswold, R., Newberg, H. J., Nichol, R. C., Nicinski, T., Nonino, M., Okada, N., Okamura, S., Ostriker, J. P., Owen, R., Pauls, A. G., Peoples, J., Peterson, R. L., Petravick, D., Pier, J. R., Pope, A., Pordes, R., Prosapio, A., Rechenmacher, R., Quinn, T. R., Richards, G. T., Richmond, M. W., Rivetta, C. H., Rockosi, C. M., Ruthmansdorfer, K., Sandford, D., Schlegel, D. J., Schneider, D. P., Sekiguchi, M., Sergey, G., Shimasaku, K., Siegmund, W. A., Smee, S., Smith, J. A., Snedden, S., Stone, R., Stoughton, C., Strauss, M. A., Stubbs, C., SubbaRao, M., Szalay, A. S., Szapudi, I., Szokoly, G. P., Thakar, A. R., Tremonti, C., Tucker, D. L., Uomoto, A., Vanden Berk, D., Vogeley, M. S.,

Waddell, P., Wang, S.-i., Watanabe, M., Weinberg, D. H., Yanny, B., Yasuda, N., & SDSS Collaboration. 2000, *AJ*, 120, 1579

Zabludoff, A. I., Zaritsky, D., Lin, H., Tucker, D., Hashimoto, Y., Shectman, S. A., Oemler, A., & Kirshner, R. P. 1996, *ApJ*, 466, 104

Zwaan, M. A., Kuntschner, H., Pracy, M. B., & Couch, W. J. 2013, *MNRAS*, 432, 492

The Evolution of Post-Starburst Galaxies from $z \sim 1$ to the Present

Abstract

Post-starburst galaxies are in the transitional stage between blue, star-forming galaxies and red, quiescent galaxies, and therefore hold important clues for our understanding of galaxy evolution. In this paper, we systematically searched for and identified a large sample of post-starburst galaxies from the spectroscopic dataset of the Sloan Digital Sky Survey (SDSS) Data Release 9. In total, we found more than 6000 objects with redshifts between $z \sim 0.05$ and $z \sim 1.3$, making this the largest sample of post-starburst galaxies in the literature. We calculated the luminosity function of the post-starburst galaxies using two uniformly selected subsamples: the SDSS Main Galaxy Sample and the Baryon Oscillation Spectroscopic Survey CMASS sample. The luminosity functions are roughly log-normal. The peak magnitudes shift as a function of redshift from $M \sim -23.5$ at $z \sim 0.8$ to $M \sim -20.5$ at $z \sim 0.1$. This is consistent with the downsizing trend, whereby higher mass galaxies form earlier than low-mass galaxies. We compared the mass of the post-starburst stellar population found in our sample to the decline of the global star-formation rate and found that only a small amount ($\sim 0.2\%$) of all star-formation quenching results in post-starburst galaxies in the luminosity range our sample is sensitive to. Therefore, luminous post-starburst galaxies are not the place where most of the decline in star-formation rate of the universe is happening.

1 Introduction

Post-starburst galaxies were first identified by Dressler & Gunn (1983) as a distinct class of galaxies, whose main spectroscopic characteristics are strong Balmer absorption lines with a lack of emission lines due to star formation. The physical explanation of these properties is that these galaxies had a large burst of star formation about 10^{8-9} years before the observation that suddenly was quenched, with very little ongoing star formation. This stellar population is old enough that the short-lived O- and B-stars have all died (thus no nebular emission lines), and young enough that the optical spectrum is dominated by A-stars (thus the strong Balmer absorption). Given the stellar population properties, one possible explanation is that these objects are in a transitional stage between star-forming blue cloud galaxies and quiescent red sequence galaxies.

The global star formation rate over the entire universe is found to have dropped by about an order of magnitude since redshift $z \sim 1$ (Madau & Dickinson, 2014). This implies that the galaxy population changed drastically between redshift $z \sim 1$ and the present time. The heavily star-forming galaxies that are abundant at high redshift must be quenched and evolve to the red, passive elliptical galaxies. If this quenching is sudden, then they will pass through the post-starburst phase in between. Therefore, we expect that the post-starburst galaxy population in this redshift range would reflect this change in the global star formation rate. In order to understand this, one needs a large, statistical sample of post-starburst galaxies that are selected with a uniform and well-understood selection method across this large range of redshift.

The terminology in post-starburst galaxy studies is rather rich and confusing. Two common names are “K+A” and “E+A”, referring to the fact that the spectra of this kind of galaxy can be decomposed into spectra of “K”- and “A”-stars (and “E” stands for elliptical galaxy, whose spectra is dominated by K-giants). Some authors have also defined a number of subclasses such as E+a (Choi et al., 2009) and post-quenching (Quintero et al., 2004). It is also closely related to the “green valley” galaxies, lying intermediate between the red sequence and blue cloud, although not all green valley galaxies have the spectroscopic signature of post-starburst galaxies. In this paper we will make no distinction between these names and just call all such objects “post-starburst”.

Two main scenarios have been proposed to explain the formation of post-starburst galaxies, which predict different detailed properties of these galaxies. While it is likely that both mechanisms contribute to the formation of post-starburst galaxies to some degree, the relative importance of the two mechanisms is far from clear. Moreover, the relative importance of each mechanism can potentially be a function of redshift and galaxy mass.

The first scenario is a cluster-related mechanism such as ram-pressure stripping. In this picture, gas-rich star-forming galaxies fall into galaxy clusters and their gas is removed by the interaction with the hot intra-cluster medium, suddenly quenching their star formation (Gunn & Gott, 1972; Balogh et al., 2000). According to this scenario, the resulting post-starburst galaxies would be found predominantly in dense environments such as galaxy groups and clusters. They would still resemble disk galaxies, since nothing apart from gas loss would disturb their morphology. This idea was first proposed by Dressler & Gunn (1983) because the first post-starburst galaxies they found were in clusters, and they therefore hypothesized that these objects lay exclusively in overdense regions. It was only found later that these objects are also present in the field (Zabludoff et al., 1996; Quintero et al., 2004; Blake et al., 2004). Interaction with the intracluster medium is also proposed as a possible way to form S0 galaxies.

An alternative scenario is that post-starburst galaxies are associated with galaxy interactions, mergers or AGN feedback. In this scenario, when gas-rich galaxies go through a merger phase, the gas is disturbed and collapses to form stars, leading to a large scale starburst. The same disturbance also funnels the gas to the galactic center, resulting in both a central starburst and AGN activity. The galaxy then either runs out of gas and stops forming stars, or the rest of the gas receives enough heating from either supernova or AGN feedback that it becomes too hot to collapse further or is expelled altogether. Either way, the galaxy goes through a starburst phase that stops quickly. This picture makes a number of predictions about the properties of post-starburst galaxies. The first is that it naturally explains the observations of post-starburst galaxies in lower density regions such as poor groups and the field. Their morphologies should show prominent signs of recent interactions such as tidal tails (Zabludoff et al., 1996; Yang et al., 2004, 2008; Blake et al., 2004; Tran et al., 2004; Goto, 2005). Post-starburst galaxies are also

expected to generally coincide with AGN, since both starburst and AGN activity are likely triggered by the same mechanisms. Also, the post-starburst stellar population is predicted to be centrally concentrated in their galaxies because the gas is driven toward the center in a merger, making the post-starburst galaxies appear more compact than elliptical galaxies at similar redshift. Observations show that this indeed is the case (Pracy et al., 2012; Swinbank et al., 2011; Whitaker et al., 2012).

The picture that gas-rich mergers drive both star formation and AGN activity is supported by theoretical work as early as, for example, Sanders et al. (1988) and Mihos & Hernquist (1994). More recent simulation work that studies this scenario includes, for example, Hopkins et al. (2006, 2008); Bekki et al. (2001, 2005, 2010) and Snyder et al. (2011). Their models suggest that the spectra of the merging systems start with strong Balmer absorption with a moderate amount of emission lines, then go through a post-starburst phase when the emission lines fade out. After about 1 Gyr, the galaxy becomes dominated by an old stellar population.

There are also other models that attempt to explain this post-starburst phenomenon. Poggianti & Wu (2000) and Miller & Owen (2001) suggest that post-starburst galaxies are in fact dust-enshrouded starburst galaxies. In this picture, the ongoing star formation is hidden behind a large amount of dust and gas and therefore the emission lines are completely extinguished. Balmer absorption lines, on the other hand, originate from A stars, which are long-lived enough to migrate out of the star-forming gas cloud and become visible. This idea can be tested at far-infrared or radio continuum wavelengths, at which one can measure the star formation rate independent of dust and gas extinction. Various authors have carried out this test and the conclusion is that even though a small number of post-starburst galaxies may include dust-enshrouded starbursts, this model does not explain the majority of the post-starburst galaxy population (Miller & Owen, 2001; Goto, 2004; Chang et al., 2001; Nielsen et al., 2012).

In order to study post-starburst galaxies and understand the relative importance of different star-formation quenching mechanisms, the first important task is the selection of the sample itself. Post-starburst galaxies are typically selected spectroscopically, with the requirement that the Balmer absorption is strong. The $H\delta$ line is commonly used for this purpose because emission

from star formation tends to be quite weak in this line, unlike $H\alpha$ or $H\beta$. It also does not have other major lines in its immediate vicinity, making the equivalent width measurement easy. The nebular emission lines, commonly represented by $H\alpha$ and $[OII]3727$, are required to be weak. For objects at higher redshift, $H\alpha$ drops out of the wavelength coverage of optical instruments and therefore the selection is usually done on the $H\delta$ and $[OII]$ lines alone. There are also a number of alternative methods such as spectral template fitting (Quintero et al., 2004), Principal Component Analysis (Wild et al., 2007) and using UV-optical colors (Choi et al., 2009).

A large sample is important to statistically represent the whole population. Large spectroscopic surveys have enabled the selection of samples of post-starburst galaxies of hundreds at low redshift (Zabludoff et al., 1996; Goto, 2005, 2007; Wild et al., 2007; Quintero et al., 2004), and a few tens at higher redshift (Blake et al., 2004; Yan et al., 2009; Vergani et al., 2010), compared to a handful of objects in earlier studies. With these samples, various global properties of the samples have been studied, such as the luminosity function (Blake et al., 2004), their clustering (Krause et al., 2013) and quantification of their environments (Zabludoff et al., 1996; Galaz, 2000; Blake et al., 2004; Balogh et al., 2005; Hogg et al., 2006; Yan et al., 2009; Poggianti et al., 2009).

More detailed information can also be obtained for a small number of post-starburst galaxies through follow-up observations. Detailed morphological studies using HST have been carried out by Belloni (1997); Caldwell et al. (1999); Tran et al. (2003, 2004); Blake et al. (2004); Yang et al. (2004, 2008) and Cales et al. (2011) and shown that they a range of morphologies. Spatially resolved spectroscopic data, either through long slit or integral field units, have been obtained and used to study the dynamical properties (Caldwell et al., 1996) and the spatial distribution of the post-starburst stellar population in individual galaxies (Norton et al., 2001; Goto, 2005; Yagi & Goto, 2006; Pracy et al., 2005, 2009, 2010, 2012; Goto et al., 2008; Swinbank et al., 2011).

In this paper, we tackle this rich and complicated problem at the key limitation of previous studies - small sample size - by first identifying a large number of post-starburst galaxies from the Sloan Digital Sky Survey (SDSS) database over a very broad range of redshifts. In section 2 we introduce the SDSS data, and give some technical background. In section 3 we describe the

method used to identify the post-starburst galaxies from this large spectroscopic dataset. The properties of the resulting sample is then described in section 4. The luminosity function analysis of this sample, and its relation to the global star-formation rate, are then explained in section 5. The discussion and conclusion of the results are then presented in sections 6 and 7.

2 Data

2.1 SDSS and BOSS Surveys

The Sloan Digital Sky Survey (York et al., 2000) has taken both imaging and spectroscopic data over more than a quarter of the sky, using a dedicated 2.5m telescope situated at the Apache Point Observatory in New Mexico (Gunn et al., 2006). The imaging data are taken in the five-band filter system - *ugriz* - defined in Fukugita et al. (1996) with the mosaic CCD camera described in Gunn et al. (1998). The raw imaging data are processed, calibrated and cataloged by algorithms described in Lupton et al. (2001). A subset of detected sources are selected for spectroscopic follow-up by a number of selection criteria based on observed magnitudes and colors. These targets are then assigned to spectroscopic tiles (Blanton et al., 2003) and their spectra obtained with the spectrograph described in Smee et al. (2013). In the first two phases of the survey (SDSS-I, SDSS-II) the selection was concentrated into three categories: a magnitude-limited sample of galaxies; the Main Galaxy Sample (Strauss et al., 2002), luminous red galaxies (LRG) at higher redshift (Eisenstein et al., 2001) and quasars (Richards et al., 2002). Spectra obtained in these phases cover the wavelength range between $3800 - 9200\text{\AA}$ at resolution of $R \sim 2000$, with typical signal-to-noise ratio per resolution element > 4 for objects brighter than $g = 20.2$. The spectra are both wavelength- and spectrophotometry-calibrated. In the third phase of the survey, SDSS-III (Eisenstein et al., 2011), the BOSS program (Dawson et al., 2013) was carried out with an upgraded spectrograph (wavelength coverage $3600 - 10400\text{\AA}$, with signal-to-noise ratio > 6 at $i = 21$). This program concentrated on galaxies and quasars at higher redshift for measurement of Baryon Acoustic Oscillations. The spectra observed are classified with redshifts measured by the spectral classification algorithm explained in Bolton et al. (2012). In addition, for the first two

phases of the SDSS survey, an alternative spectral classification was performed (SubbaRao et al., 2002). In this work we based our study on all available spectra in SDSS-I/II and BOSS spectra in SDSS-III up to the Data Release 9 of the survey (SDSS DR9; Ahn et al. 2012).

2.2 SDSS Magnitude System

For each SDSS object, the inverse hyperbolic sine magnitude (asinh; Lupton et al. 1999) in the AB system in all five bands is measured from raw imaging data by a number of different methods, resulting in a variety of magnitudes that we will find ourselves using throughout this paper. Fiber magnitude measures the flux contained within the spectrograph fiber. Petrosian magnitude is designed to measure galaxy photometry optimally (Petrosian 1976; Blanton et al. 2001; Yasuda et al. 2001 and Strauss et al. 2002). The PSF magnitude measures the flux of a point source, using the PSF as a matched filter. Model and cModel magnitudes measure the flux of a galaxy by fitting surface brightness profiles to the image. The Spectro magnitude measures the brightness from the spectra, relying on the excellent spectrophotometric calibration of SDSS (Adelman-McCarthy et al., 2008). In later analysis, we distinguish and convert between these magnitude systems. More details on this can be found in the SDSS website <http://www.sdss.org/dr12/algorithms/magnitudes/>.

2.3 Small Sample of Post-Starburst Galaxies

We assembled a small sample of known post-starburst galaxies at both low and high redshift, which will be used to test and tune the selection criteria that we will introduce in subsequent sections.

This contains the 564 low-redshift ($z_{\text{median}} \sim 0.1$) post-starburst galaxies found in the 5th Data Release of the Sloan Digital Sky Survey (Adelman-McCarthy et al., 2007) by Goto (2007). This sample was selected from the main galaxy catalogue at redshift $z < 0.33$ such that the $H\alpha$ line is well within the wavelength coverage of the spectra. It was selected by the equivalent width cuts

$H\delta$ EW $> 5.0\text{\AA}$, $H\alpha$ EW $> -3.0\text{\AA}$ and $OII\lambda 3727$ EW $> -2.5\text{\AA}$, where positive value of equivalent width corresponds to absorption and negative value to emission.

We add to this about 100 intermediate- and high-redshift objects (redshift $z \sim 0.4 - 0.8$) that were mostly found serendipitously from visual inspection of SDSS and BOSS spectra.

3 Selection of post-starburst galaxies

3.1 Spectral Templates

The selection method we use is based on template fitting, following Quintero et al. (2004). In this section we describe the templates we use. As suggested by the name “E+A” or “K+A”, these objects’ spectra can be decomposed into a linear combination of the spectrum of an old stellar population (the “E” or “K” component), and the spectrum of an A-type star. We use the old stellar population template of Eisenstein et al. (2003). This is the composite spectrum of Luminous Red Galaxies in SDSS, which is dominated by the light of K-type giants. The spectrum of Vega (an A0V star) from Bohlin & Gilliland (2004) is used to represent the “A”-template. Both “K” and “A” templates are normalized such that the total fluxes over the wavelength range 3600-4400 \AA are the same, as shown in Figure 2.1. We emphasize that this template fitting approach is only a crude fit to the underlying stellar population. A proper and more detailed analysis of the stellar populations in our sample will be carried out in future work.

3.2 Selection Methods

Redshift Range Determination

The SDSS main spectral classification pipeline provides redshifts and classifications for all spectra based on the Principal Component Analysis (PCA) technique (Bolton et al., 2012). This pipeline redshift is reliable for object types that are common and have large numbers contributing to the PCA templates. This is not always the case for the post-starburst galaxies that we try to select, especially at high redshift. In the preliminary stage of this work we found that a number of

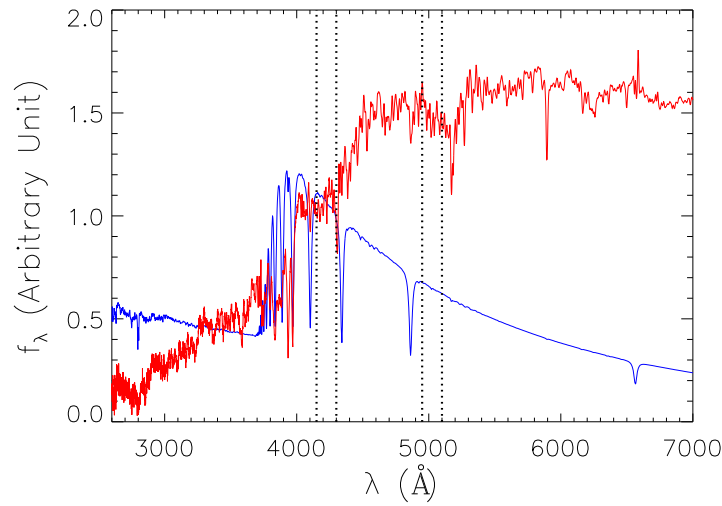


Figure 2.1 This plot shows the spectra used as fitting templates for “A” (blue) and “K” (red) components of the galaxy population. The “A”-template is the spectrum of Vega, which is representative of generic A0V stars, from Bohlin & Gilliland (2004). The “K”-template is the composite spectrum of Luminous Red Galaxies (LRGs) in SDSS (Eisenstein et al., 2003). The fits are carried over the wavelength range 3600-4400Å and the templates are normalized such that the integrated fluxes over this range are the same. The vertical lines show the wavelength ranges 4150-4300Å and 4950-5100Å (hereafter called [4200] and [5000] respectively) corresponding to our fiducial bands used in later sections.

known post-starburst galaxies, especially at high redshift, have wrong redshifts and are misclassified. Since we desire that the final sample be as complete as possible, we do not assume that the redshift value given by the pipeline is reliable, and will determine the redshift from the spectrum as if the redshift is not known a priori. For this reason we allow redshift to be a free parameter when we perform the template fitting. The redshift is constrained such that the rest-frame wavelength range of the template, 3600-4400Å, is contained within the observed spectra, corresponding roughly $z = 0.05 - 1.1$ for the SDSS wavelength coverage (3800-9200Å) and $z = 0 - 1.35$ for the BOSS wavelength coverage (3600-10200Å).

However, in SDSS-I/II an alternative, independent spectral classification pipeline is available (SubbaRao et al., 2002). This pipeline disagrees in redshift with the main pipeline significantly for about 2% of the objects. Even though both of these pipelines can be individually incorrect, when the two agree the redshift is highly likely to be correct. So when this happens (more specifically, when the two redshifts differ by less than 0.005) we do not perform the template fitting over the full redshift range, but only around a narrow range $\Delta z = 0.008$ around the average of the two to find the local optimum. For BOSS, since this alternative pipeline is not available, the redshifts for BOSS galaxies are never assumed to be known a priori.

Redshift Determination

Once the redshift range to be fit over is determined, the template fitting is performed at every value of redshift in the range with uniform spacing $dz = 0.001$. For each redshift value two models are fitted to the wavelength corresponding to 3600-4400 Å rest-frame wavelength, shifted to this value of redshift. The first model is to fit a linear combination of the “K”-template, “A”-template and a second-order polynomial in wavelength as continuum. This is written mathematically as

$$y_{\text{Model1}} = C_K K(\lambda) + C_A A(\lambda) + C_0 + C_1 \lambda + C_2 \lambda^2 \quad (2.1)$$

where $K(\lambda)$ and $A(\lambda)$ correspond to the “K” and “A” templates. The continuum is included to take into account other possible slowly-varying effects such as AGN continuum, dust extinction,

spectrophotometric errors and template errors. The second model is to fit only the second-order polynomial in wavelength, without the “K” and “A” templates.

For each fit, the value of the C parameters are determined by the standard minimum χ^2 fitting method, with each pixel weighted by the inverse square of the per-pixel error output by the spectroscopic pipeline. This method can yield negative, unphysical values of C_K or C_A . There are other classes of fitting method that can constrain parameters to be positive-definite. However, considering the ease of implementation and the fast computational speed (especially since we need to run this process on the whole SDSS and BOSS spectroscopic database, consisting of more than 2 million spectra), we use this simple χ^2 fit and tolerate this issue. This is not a problem since visual inspection (see below) is done at the end to ensure the quality of all fits anyway. Generally, it is also found that the polynomial component is usually small compared to the “K” and “A” components, thus the spectra are typically well represented by a linear combination of the two spectral templates.

For each redshift, we use the difference in χ^2 values of the two models, $\Delta\chi^2 = \chi_{\text{Model2}}^2 - \chi_{\text{Model1}}^2$, as indicator of a good template fit. $\Delta\chi^2$ indicates how much better the fit is for the model with templates included, compared to the pure polynomial model. A large value of χ^2 could only happen if at least one of the “K” or “A” template is a good representation of the spectrum at that redshift. We take the redshift with the maximum value of $\Delta\chi^2$ as the true redshift of the object.

For true post-starburst galaxies we found that the value of $\Delta\chi^2$ is at least around 40-50 (much larger than $\Delta\chi^2 \sim 2$ expected by increasing the number of parameters by 2), and up to few thousands for objects with strong post-starburst features with good signal-to-noise ratio. Values of $\Delta\chi^2$ lower than this are usually associated with low signal-to-noise spectra and it is usually unclear whether the spectral features are actually detected, therefore they are removed in the visual inspection process.

Identification of Post-starburst objects

To quantify the contribution of the “A”-spectrum component to the fit in order to identify post-starburst galaxies, we introduce a parameter, A/Total , defined as $A/(K + A + P)$ where K , A and P are the integrated flux in the wavelength range 4150-4300Å (hereafter called [4200]) of the “K”, “A” and the polynomial components of the model fit described above. This wavelength range corresponds to the continuum between the two Balmer absorption lines $H\gamma$ and $H\delta$ (Figure 2.1) which are prominent features in the A-star spectrum. We require that this A/Total ratio be greater than 0.25 for an object to be considered a candidate post-starburst galaxy. This particular cut at 0.25 is determined such that the selection algorithm recovers objects in the sample of known post-starburst galaxies (section 2.3) with reasonably strong spectral features.

Equivalent Width Cut; Visual Inspection

We also put requirements, adopted from Goto et al. (2003), on the equivalent widths of two key spectral lines. We require that the rest-frame equivalent widths satisfy $H\delta\text{EW} > 4.0\text{\AA}$ and $[\text{OII}]\lambda 3727\text{EW} > -2.5\text{\AA}$, where a positive value in equivalent width corresponds to absorption. The requirement on strong Balmer absorption guarantees a substantial contribution from the A-star component, while the lack of [OII] emission indicates an insignificant amount of ongoing star formation. The requirement on the $H\delta$ equivalent width is somewhat redundant to the requirement on A/Total ratio, since they both measure the contribution of the A-star component. We still include both to ensure that the high A/Total ratio is not only due to the good fit to the continuum by the A-star template. These cuts are less conservative than the cuts used in Goto (2007) ($H\delta\text{EW} > 5.0\text{\AA}$). This choice is made so that the sample is as inclusive as possible before all candidates are visually inspected.

The equivalent widths are calculated by summing the flux density over the line. A linear function is fit to the red and blue sidebands of the line to define the continuum region, then the excess over this continuum in the line region is used to calculate the equivalent width. The values of rest-frame wavelengths used to define the red and blue sidebands and the bandpass of relevant

Line	Bandpass	Blue Sideband	Red Sideband	Reference
[OII] λ 3727	3716.30-3738.30Å	3696.30-3716.30Å	3738.30-3758.30Å	Yan et al. (2006)
H δ	4083.50-4122.25Å	4041.60-4079.75Å	4128.50-4161.00Å	Kauffmann et al. (2003)
H α	6554.60-6574.60Å	6483.00-6513.00Å	6623.00-6653.00Å	Yan et al. (2006)

Table 2.1 The definition of the wavelength ranges we used to calculate the equivalent widths for different lines. A line is fitted through both the blue and red sidebands to represent continuum level, which is used for the equivalent width calculation in the central bandpass. The references for the use of these exact values are given in the last column.

lines (including H α , which will be used in following sections) are shown in Table 2.1. We did not apply any cut on the signal-to-noise ratio of the equivalent width measurements. We will quantify the effects of limited signal-to-noise ratio when we derive the luminosity function in later section.

It should be noted that this selection method is designed to select only those post-starburst galaxies in which the starburst had occurred at least a few hundred Myr previously. Significantly younger post-starburst galaxies will have some [OII] λ 3727 emission or weaker H δ absorption, and thus can be excluded from the sample. We will quantify the effects of this incompleteness below.

Finally, after the fitting process and various cuts, we visually inspect the spectra of all candidate post-starburst galaxies. There is a fairly high false positive rate (objects that are flagged by the selection process as candidates, but turn out to be other classes of objects). Most of these are catastrophically wrong fits in which the templates happen to match to certain spectral features producing a (small) maximum value of $\Delta\chi^2$ at some assumed redshift while at the same time giving $A/\text{Total} > 0.25$. These are removed by visual inspection at this stage. The other class of contamination is A stars and white dwarfs whose spectra fit the “A”-template extremely well at $z = 0$ by construction. This problem only exists for BOSS spectra because the wavelength coverage extends blue enough for the 3600-4400 Å range to be within the data coverage at zero redshift. We solve this issue by requiring the best-fit redshift to be bigger than $z = 0.02$, which vastly reduces the number of candidates to be visually inspected. The numbers of objects considered at each stage in the selection process are shown in Table 2.2. This selection method does a decent job of screening the entire spectroscopic database and selecting a relatively small number of potential candidates. Yet it still has a high false positive rate, about 300% for SDSS and 100% for BOSS, requiring human inspection of the spectra.

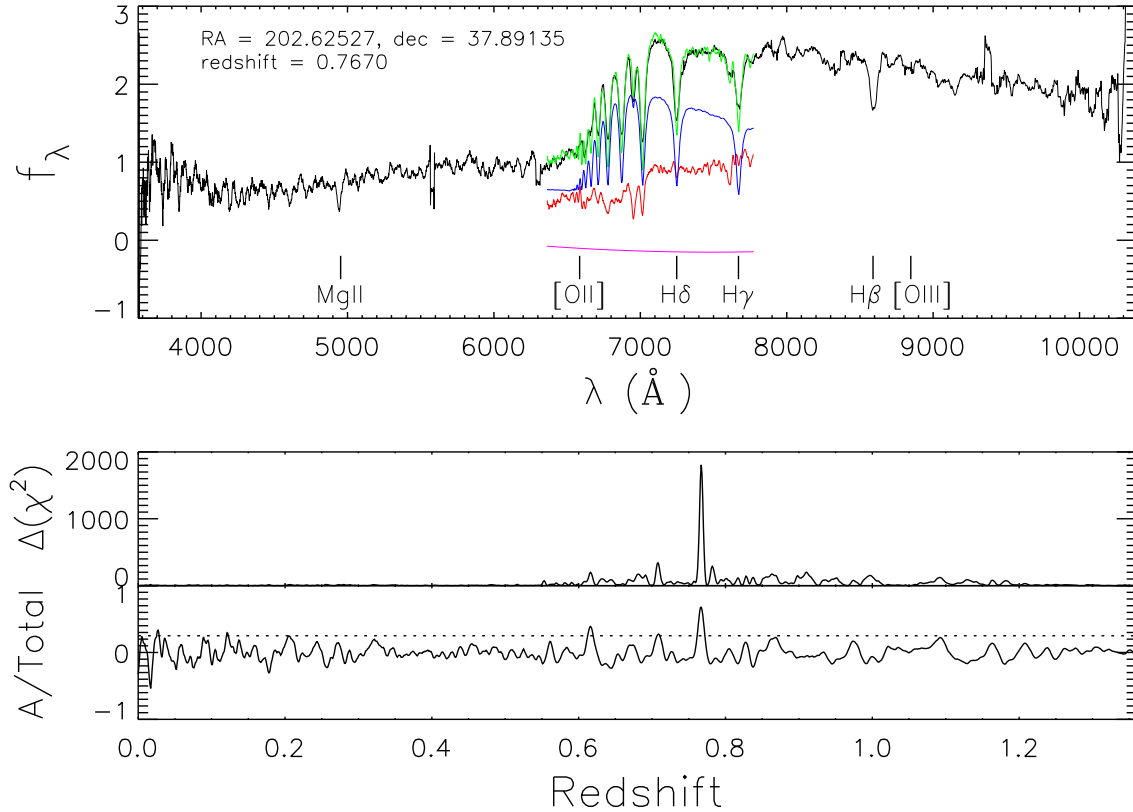


Figure 2.2 The template fitting procedure is demonstrated in this plot. The object shown is a post-starburst galaxy from BOSS at RA = 202.62527° and DEC = 37.89135° and redshift $z = 0.7670$, observed on plate 3984, fiber 233 and MJD 55333. For this object, the pipeline redshift (Bolton et al., 2012) is accurate. The top panel shows the spectrum of this object, smoothed for increased visibility. Overplotted are the best-fit model (green) with its “K”, “A” and polynomial components (red, blue and magenta respectively) at the correct redshift. Positions of several major lines are shown. For this object, there is no emission in [OII] λ 3727 as required by our selection criteria, while the H α line is outside the spectral coverage. The bottom panels show the parameters $\Delta(\chi^2)$ and A/Total of the fit done at all values of assumed redshift within the allowed range. The candidate redshift is where the inclusion of templates in the fit maximally improves the fit, resulting in the peak in $\Delta(\chi^2)$. At this redshift the A/Total ratio is required to be higher than the threshold value of 0.25, represented by the horizontal dotted line, in order to enter the sample. After passing this criterion the fit is visually inspected before being included into the final sample.

Step	SDSS	BOSS
All Spectra	$\sim 1.7 \times 10^6$	$\sim 7.6 \times 10^5$
Program Candidates	8216	23728
Program Candidates ($z > 0.02$)	8216	8485
Visually Inspected	2330	3964

Table 2.2 The number of spectra considered at each stage of the selection process. The first row is the total number of spectra considered, essentially every spectrum available in the SDSS DR9. The second row is the number of spectra flagged by the selection method to be possible post-starburst galaxy candidates after the fitting process and the application of the cuts on the A/Total ratio and the equivalent widths of the $H\delta$ and $[OII]\lambda 3727$ lines. The third row is the same as the second row but with the requirement that $z > 0.02$ to remove the contamination from A-stars and white dwarfs. This redshift restriction does not affect SDSS sample since the wavelength coverage does not allow us to probe to such low redshift. The last row is the number of post-starburst galaxies in the final sample after the visual inspection.

This selection method recovers most of the known post-starburst galaxies described in section 2.3. The ones that are not recovered either have signal-to-noise ratio too low or are simply contaminants to that sample. Therefore we believe that this selection method is robust and is able to identify most post-starburst galaxies in the sample, with a low false negative rate. It is not surprising that this selection method is robust when used against this known sample, since it was designed around this very sample. However, since the method is generic and the amount of fine-tuning is minimal, we expect that this selection method is robust in general.

4 Sample Properties

In this section we present our final sample, which is distributed uniformly over the survey footprint as expected. An ASCII file containing the full list of post-starburst galaxies presented in this paper, along with important properties, is included. Table 2.3 shows example entries of that full list.

The redshift distributions of the post-starburst galaxies selected from both SDSS and BOSS are shown in Figure 2.3. The median redshifts are around 0.2 for SDSS and 0.6 for BOSS respectively, with very little overlap between the two samples. Example of the spectra of these objects are shown in Figure 2.4. These examples are selected to illustrate a range of properties

spanned by the objects in our sample. A diverse range of spectral features are seen among the objects in this sample. First is the strong Balmer lines, especially $H\delta$, in absorption which is one of the requirements for the selection. A number of objects show a blue continuum blueward of 4000\AA , which is a sign of either a young stellar population or AGN activity. A large number of objects show weak MgII absorption, some even with detectable blueshift, indicative of outflows, which may be driven by either AGN or compact starburst (Tremonti et al., 2007; Diamond-Stanic et al., 2012; Sell et al., 2014). More rare are objects with broad MgII in emission, clearly indicative of AGN activity. These are “post-starburst quasars” (for example, Brotherton et al. (1999, 2004)). The $H\alpha$ line for lower-redshift objects also shows a diverse range of behaviors, ranging from absorption to broad line emission. This $H\alpha$ behavior and how it is related to the contamination in the selection will be discussed in section 4.4. The quantities A/Total and $H\delta$ absorption Equivalent Width are roughly correlated. This is expected since both are indicators of the strength of the A-star component. Figure 2.5 shows the distribution of the median signal-to-noise ratio per pixel in the $4150\text{-}4300\text{\AA}$ range ([4200] band) of the sample as a function of redshift and rest-frame absolute magnitude in the same wavelength range (denoted by [4200]; for more details on the calculation of this magnitude, see section 5.2) respectively. Even though we have not made cuts in signal-to-noise ratio explicitly, most post-starburst galaxies in our sample have signal-to-noise ratios at least a few in this wavelength range. We found that the median signal-to-noise ratio per pixel of about 2 is the lower limit to robustly identify post-starburst galaxies. Therefore, the mis-identification due to low signal-to-noise ratio is not a major source of concern for this sample. We quantify the effects of signal-to-noise ratio on selection further below.

4.1 Coadded Spectra

The spectra from the sample were coadded to have a high signal-to-noise ratio representative spectrum of the post-starburst galaxy sample. To do this, the spectra are summed with inverse variance weighting, after bringing all spectra to zero redshift and scaling each to a mean flux density between $4150\text{-}4300\text{\AA}$. The final coadded spectrum, along with the fit of this spectrum into components (Equation 2.1), are shown in Figure 2.6. This combined spectrum calculated

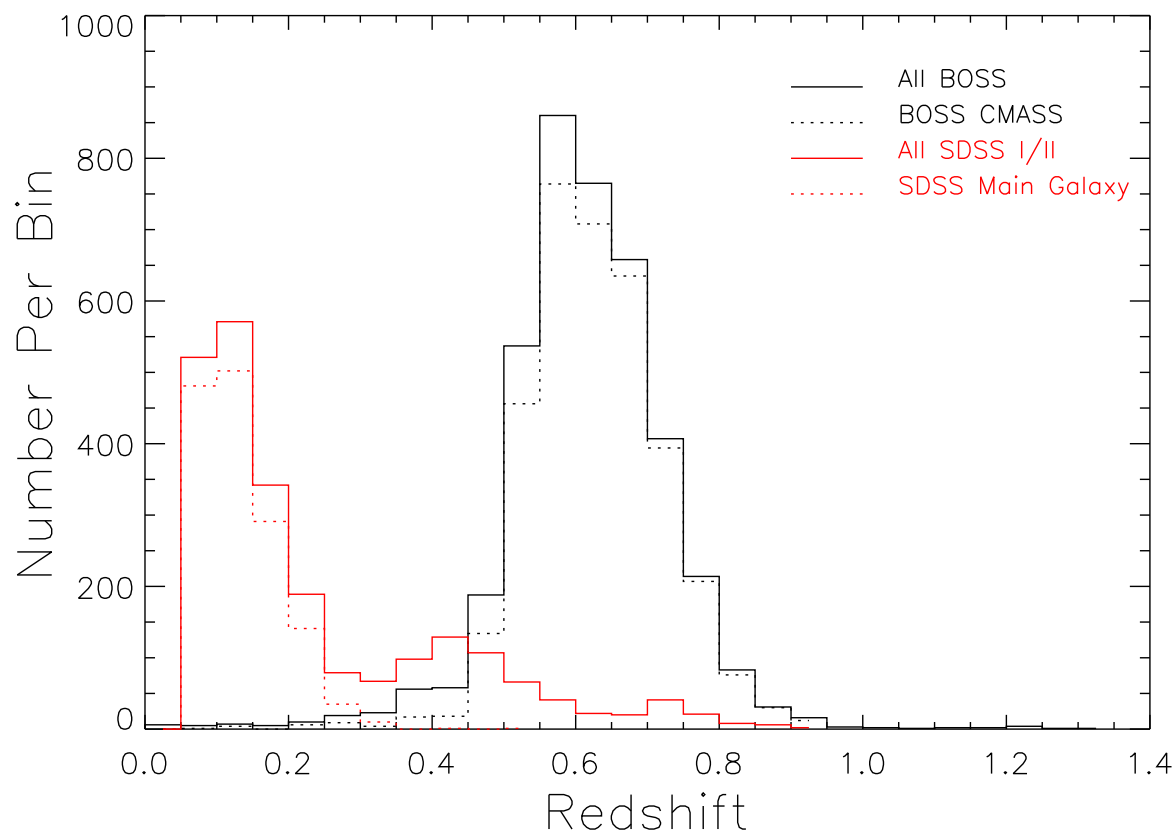


Figure 2.3 Redshift distributions of post-starburst galaxy samples from both SDSS I/II and BOSS. The solid lines of different colors (red: SDSS I/II, black: BOSS) show the distributions of the entire respective samples, while the dotted lines show the subsamples used to calculate the luminosity function (the Main Galaxy Sample for SDSS, and the CMASS galaxy sample for BOSS). Note the tail of objects with redshifts up to $z \sim 1.3$.

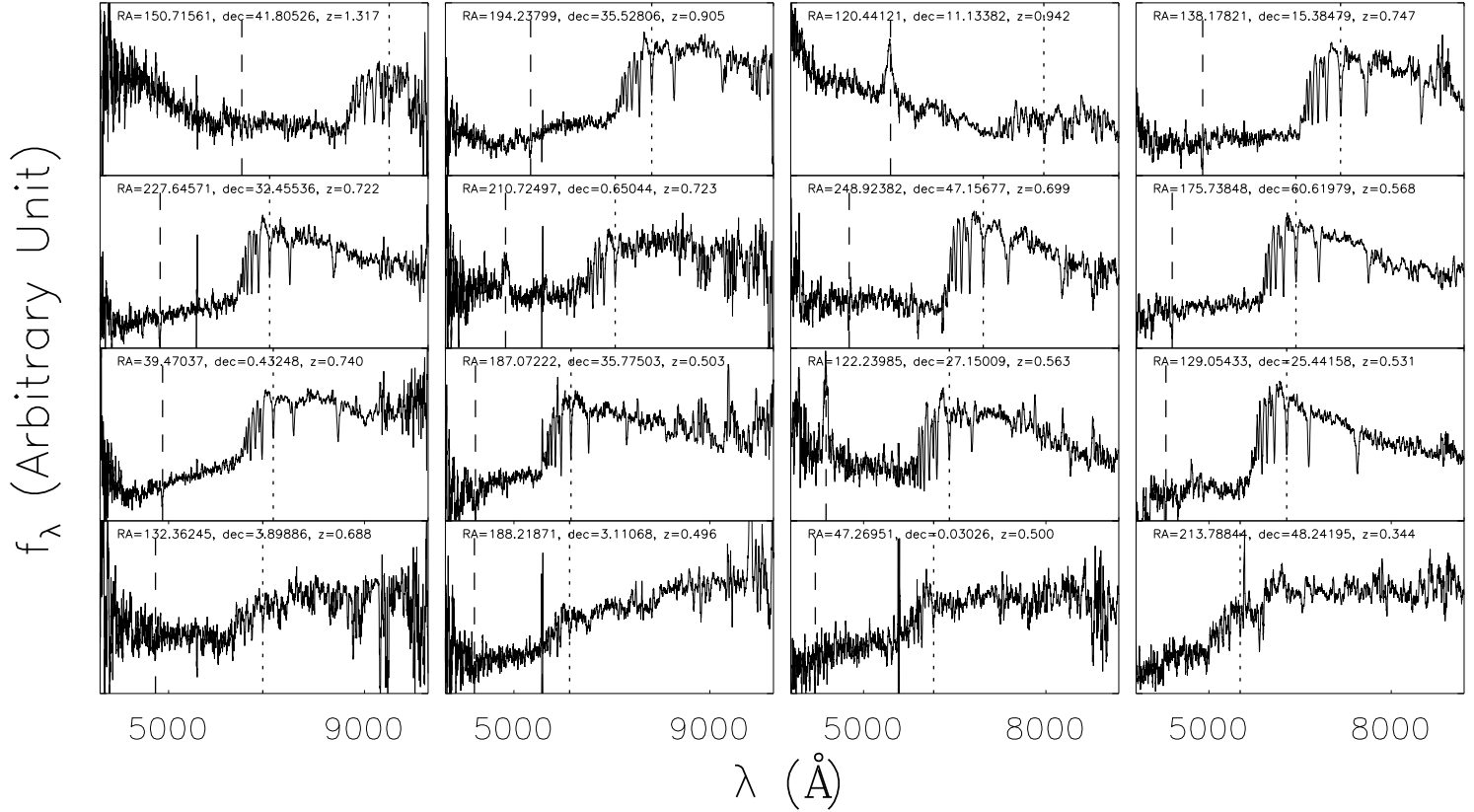


Figure 2.4 Spectra of a number of objects selected from our final sample. The left half shows objects from the BOSS sample while the right half shows ones from the SDSS I/II sample. The top left corner panel of each side shows the highest-redshift object in each sample. The bottom four panels show objects with noisy spectra to demonstrate the lowest signal-to-noise ratio that could be firmly identified as post-starburst galaxies. The rest of the panels are selected to roughly represent the range of redshift and A/Total ratio spanned by the sample and to also show objects with interesting spectral features, such as blue continuum or MgII λ 2803 line in both absorption and emission. All spectra are smoothed by 10 pixels to show features clearly. Dashed and dotted vertical lines show the position of the MgII λ 2803 and H δ lines respectively. Many spectra show a residual of the strong sky line at 5577 \AA .

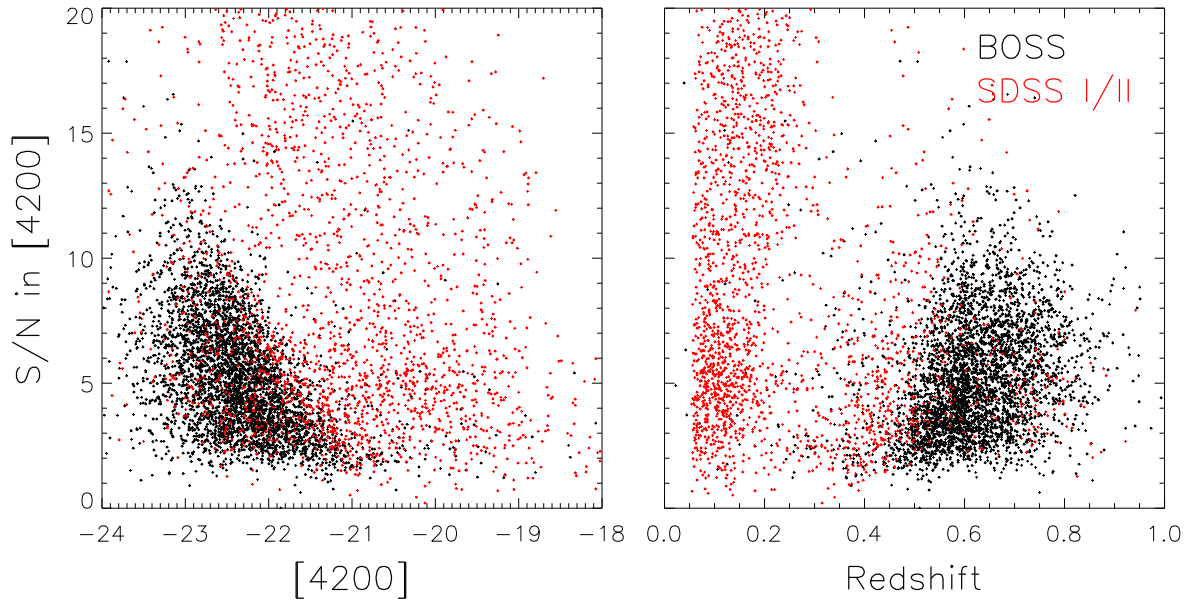


Figure 2.5 Median signal-to-noise per pixel in rest-frame wavelength range between 4150-4300Å (the “[4200] band”) of post-starburst galaxies in our sample, shown as a function of the rest-frame absolute magnitude in the same band (see Section 5.2 for more details) and redshift. The red and black points represent objects from SDSS-I/II and SDSS-III BOSS samples respectively. It should be note that the objects with $S/N < 2$, which is a lower limit for identifying post-starburst galaxies robustly.

Survey	RA(°)	DEC(°)	Plate	Fiber	MJD	z	H δ EW	[OII] λ 3727EW	A/Total	Target Selection	$z = z_{\text{pipe}}$
SDSS	120.44121	11.133820	2418	499	53794	0.942	4.80	-1.75	0.32	36700160	False
SDSS	247.71479	47.069620	627	377	52144	0.825	8.06	5.80	0.76	33554433	True
SDSS	35.161773	0.53262315	2637	205	54504	0.646	8.65	-0.29	0.67	32	True
BOSS	165.43852	37.536575	4626	730	55647	1.292	7.43	-0.26	0.54	10995116687360	True
BOSS	233.62838	0.72746109	4010	118	55350	0.941	8.75	-2.00	0.34	3298535538688	True
BOSS	124.34978	34.166264	3758	865	55506	0.823	8.41	0.45	0.69	134	True

Table 2.3 Example of the full list of post-starburst galaxies presented in this paper to demonstrate the format. The first column indicates whether the object belongs to the SDSS I/II or BOSS subsample. Columns 2-6 are for identification: Right Ascension, Declination and the Plate/Fiber/MJD identification of SDSS spectroscopy. Column 7 is the redshift determined from our selection method. Columns 8-10 are properties used in the selection method, namely the equivalent widths of H δ and [OII] λ 3727 lines, and the A/Total ratio from template fit. Column 11 is the bitmask showing the spectroscopic target selection algorithm. The bitmask can be decoded using information available on the SDSS website http://www.sdss3.org/dr10/algorithms/bitmask_legacy_target1.php for SDSS I/II objects, and http://www.sdss3.org/dr10/algorithms/bitmask_boss_target1.php for BOSS objects. The last column indicates whether the pipeline redshift (Bolton et al., 2012) agrees with the fit redshift. The objects in this table are unique objects, separated by SDSS I/II and BOSS surveys, and ordered by redshift. The full table is available in ASCII format.

from the whole sample of several thousand galaxies has very high signal-to-noise ratio and many spectral features are identified with high confidence. A small amount of $[\text{OII}]\lambda 3727$ and $\text{H}\alpha$ in emission can be seen under closer inspection. This is due to emission in individual objects that are small enough to pass the equivalent width cuts.

The coaddition is also done for various different subgroups of galaxies in order to investigate whether the spectra change systematically with properties of the galaxies. The coadded spectra of objects in two redshift bins are in excellent agreement, showing that most of the small-scale features are real. On the other hand, the continuum colors of two redshift bins differ somewhat. As most objects in the low-redshift bin are from SDSS I/II while the high redshift bin is dominated by BOSS objects, this reflects the different selection of the two samples. This selection effect is properly corrected for in the luminosity function analysis in section 5.

Figure 2.7 shows the coadded spectra binned by absolute magnitude in the fiducial band at 4200\AA . Again, the fine features in the spectra match extremely well between the different bins. The brightest group of objects are significantly bluer longward of 4500\AA . There is also a slight difference in continuum level blueward of 3500\AA , where the brightest group of galaxies have slightly higher continuum level. These differences are likely an astrophysical effect, since the more intrinsically luminous objects are likely dominated by an A-star population (in other words, they have higher A/Total ratio), and this population is relatively less luminous at red wavelengths and more luminous at bluer wavelengths.

Figure 2.8 shows the coadded spectra binned by the continuum color below 3500\AA , defined as the ratio of the flux density at 2500\AA to that at 3100\AA , averaged over bandpasses with 200\AA width. A relatively small number of objects with very blue continua (~ 100 out of ~ 3500 which have high enough quality spectra and at high enough redshift that this exercise can be carried out) have broad line emission in $\text{MgII}\lambda 2803$ and $\text{NeV}\lambda 3426$, while the rest of the sample tends to have MgII in absorption. This broad line emission is the distinct signature of post-starburst quasars. Objects with blue continua also tend to show stronger $[\text{OII}]\lambda 3727$ line in emission than the rest of the sample. The difference is small by construction since any object with more significant $[\text{OII}]$ emission would not be selected into the sample. This increased $[\text{OII}]$ emission can

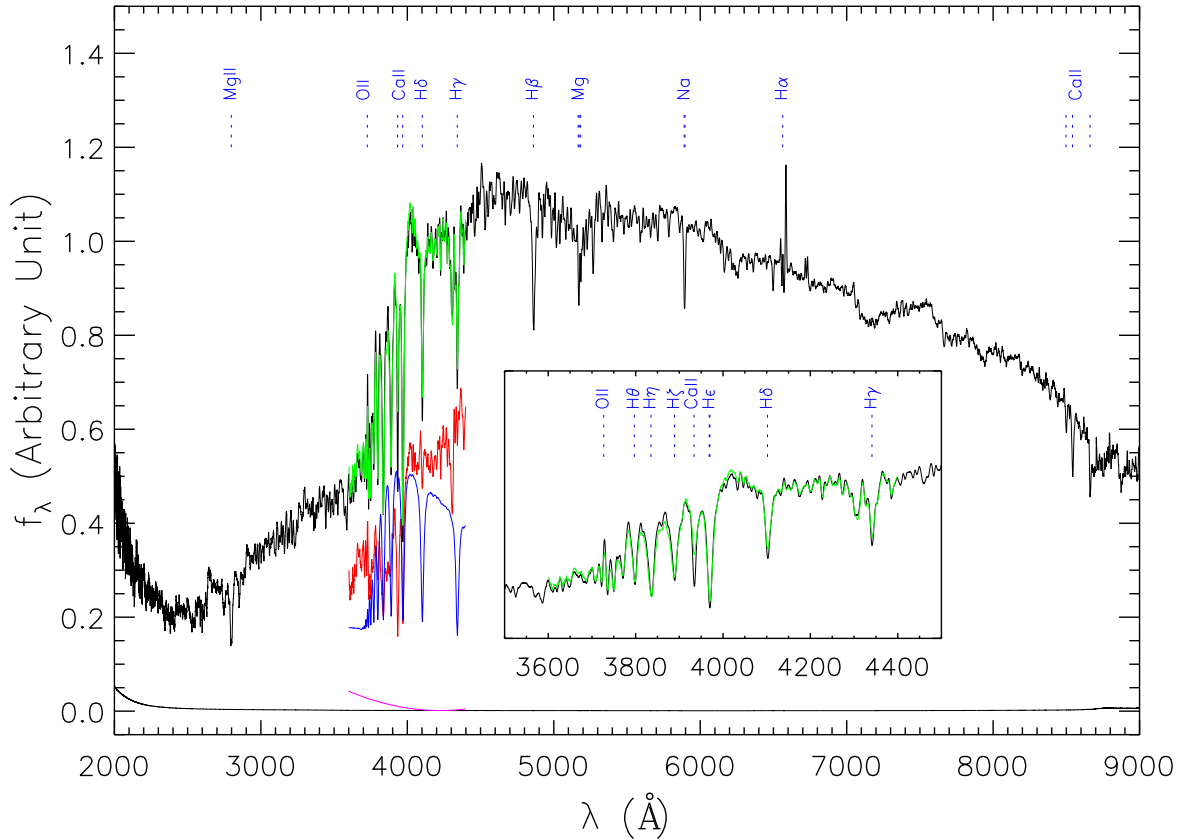


Figure 2.6 The coadded spectrum of the post-starburst galaxy sample from both SDSS and BOSS, with line features identified. The black solid line at the bottom of the plot shows the per-pixel error of the spectrum. The errors are very close to zero over most of the spectral range. The inset shows the spectrum in the 3600-4400 Å region, which is used for template fitting, in more detail. The green curve shows the model fit to this coadded spectrum, with the “K”, “A” and Polynomial components of the model shown in red, blue and magenta respectively. Note that the polynomial component is small in this coadded spectrum, as it is for most individual objects. It should be noted that at the short and long wavelength ends ($\lambda < 3000\text{Å}$ and $\lambda > 8000\text{Å}$), the coadded spectrum is derived from only a small number of objects and thus may not be very reliable.

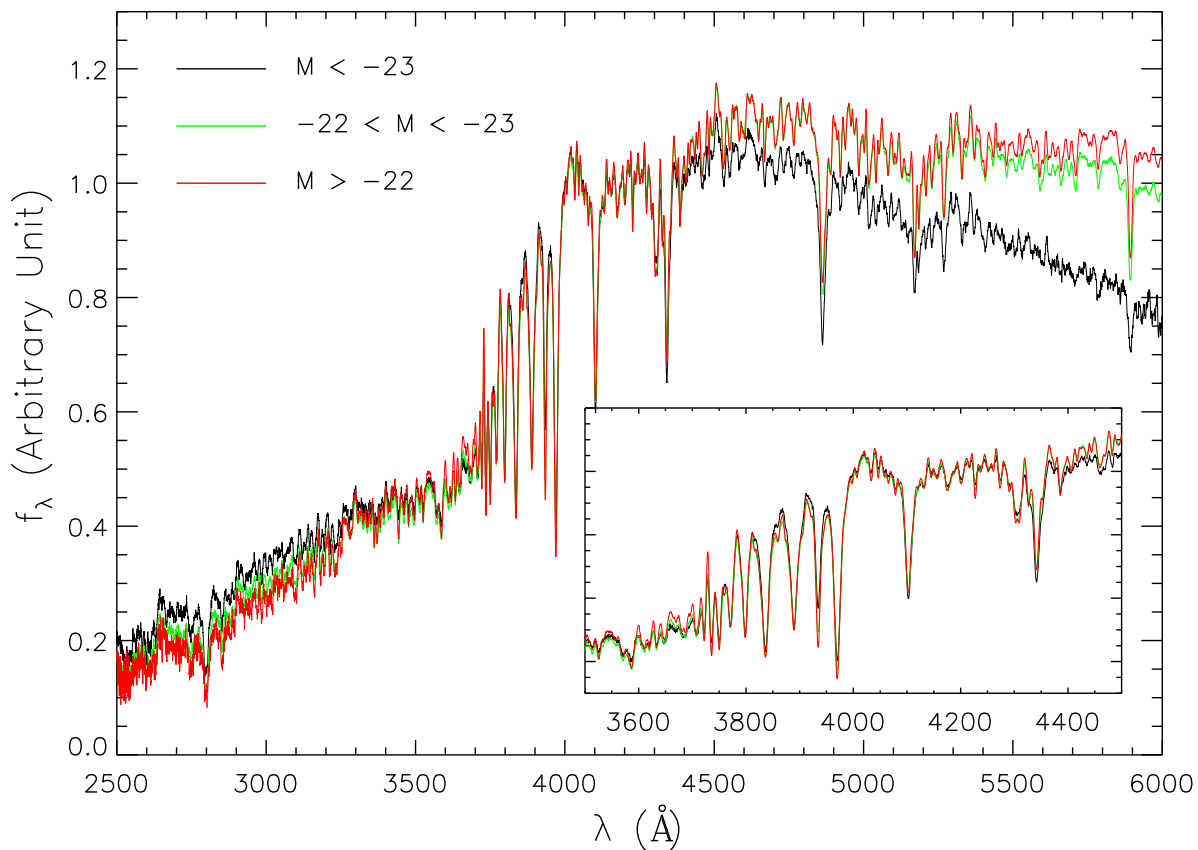


Figure 2.7 The coadded spectrum of the post-starburst galaxy sample binned by absolute magnitude in our fiducial [4200] band. The black, green and red lines are the most, intermediate and least luminous groups respectively. The small spectral features match in detail in these independent coadds, demonstrating that they are real. The difference in overall SED shapes likely reflects intrinsic properties of the populations.

be due to either a small amount of ongoing star formation, or more likely, AGN activity as already hinted by broad MgII emission. This sample can be compared to a bigger sample of SDSS post-starburst quasars presented by Brotherton et al. (2004). Most of those objects have strong enough [OII] emission that they would be excluded from our sample by our requirement on [OII] equivalent width.

4.2 Spectroscopic Target Selection

SDSS and BOSS choose targets for spectroscopic observation based on colors and morphology from the imaging data. Each spectroscopic target is selected by (possibly multiple) selection criteria. Therefore, in order to understand the properties of this sample, it is crucial to understand how each object is selected in the spectroscopic sample in the first place.

Tables 2.5 and 2.6 show the breakdown of target selection algorithms by which our post-starburst galaxies are selected, from both the SDSS I/II and BOSS sample. In the SDSS I/II sample, the `GALAXY` flag is the dominant target selection algorithm. This corresponds to the Main Galaxy Sample, which is the $r_{\text{petro}} < 17.77$ magnitude-limited galaxy sample described in Strauss et al. (2002).

The only other dominant selection flag among the SDSS I/II sample is `QSO_HIZ`, which is designed for the high-redshift quasars. A significant number of objects are selected through this flag because they appear unresolved, as required by the high-redshift quasar selection criteria, and the broadband color of the Balmer break at redshift less than unity resembles the Lyman break at redshift $z \sim 3 - 4$ (Fan et al., 1998).

For the BOSS sample, the dominant selection flags are all related to the CMASS program, which is the “Constant Stellar Mass” sample of luminous galaxies with redshift $0.4 < z < 0.7$ designed to measure Baryon Acoustic Oscillations (Anderson et al., 2012; Dawson et al., 2013). The most important of these flags is the `GAL_CMASS` flag. The flags `GAL_CMASS_COMM` and `GAL_CMASS_ALL` were used in the early part of the survey to tune the CMASS selection criteria, and are therefore more inclusive but less complete. When we calculate the luminosity function for the CMASS galaxies (Section 5), we limit our sample to the objects selected by the `GAL_CMASS`

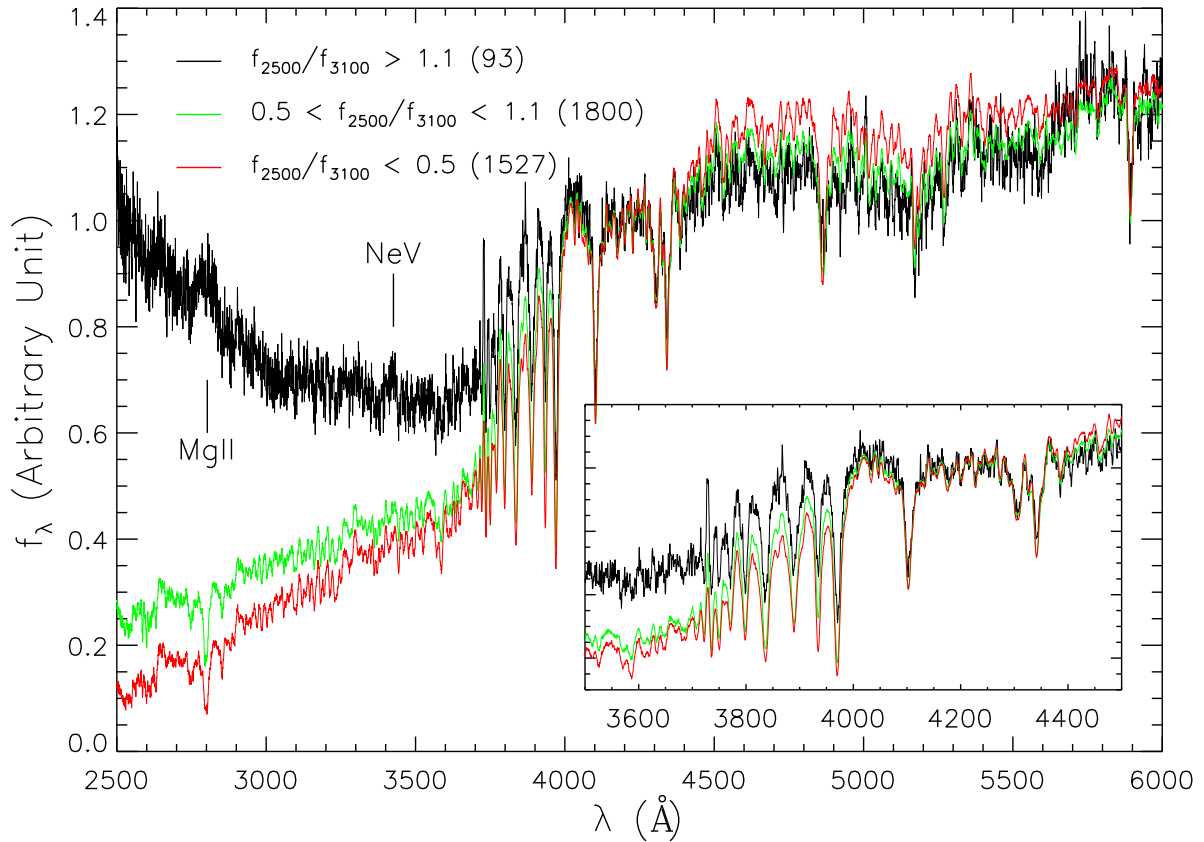


Figure 2.8 The coadded spectra of the post-starburst galaxy sample binned by the continuum color below 3500\AA , defined as the ratio of flux density at 2500\AA to that at 3100\AA , averaged over bandpasses with 200\AA width. The numbers of objects in each bin are shown in parentheses. The most dramatic feature, in addition to the slight difference in continuum color at the red side of 4000\AA break, is that the composite spectrum of objects with extremely blue continuum shows broad line $\text{MgII}\lambda 2803$ emission, while the rest of the sample shows it in absorption. Additionally, $\text{NeV}\lambda 3426$ in emission can be seen in this population. That is, these are post-starburst quasars, showing both AGN features (blue continuum, broad line emission) and post-starburst spectral features.

flag only. It should also be noted that very few objects in our sample are part of the other major BOSS galaxy sample, the LOWZ sample.

4.3 Comparison to the Pipeline Redshifts

We mentioned in section 3.2 that some of the high-redshift post-starburst galaxies have incorrect pipeline redshifts. We now discuss this issue in more detail.

Table 2.4 summarizes the comparison between pipeline redshifts and our measured redshifts for our post-starburst galaxy sample. The sample from SDSS I/II is broken down by availability of the second pipeline redshift. For this sample, the main spectroscopic pipeline (`id1spec2d`) redshift (Bolton et al., 2012) and the `spectro1d` redshift (SubbaRao et al., 2002) are incorrect 4-6% of the time. The BOSS post-starburst sample has better redshift determination; it is incorrect for only about 2% of our objects. The main reason the pipeline redshifts are incorrect is the lack of post-starburst spectral templates in the spectroscopic pipeline. This was improved in the BOSS sample, resulting in better redshift determination. Other reasons for incorrect redshift determinations are artifacts in the data that significantly change the shape of the continuum, such as bad CCD columns or light leakage from bright object in adjacent fibers, or simply too low signal-to-noise ratio. In most (but not every) of these cases, the `ZWARNING` flag is set by the pipeline to indicate low confidence in the redshift.

Two objects with discrepant redshifts are particularly interesting: they are actually pairs of objects along the same line of sight at different redshifts. In these cases, our post-starburst galaxy selection method identifies one object of the pair, while the SDSS spectroscopic pipeline correctly identifies another. These systems are shown in Figure 2.9 with various line features identified. The first system is a post-starburst galaxy at redshift $z = 0.861$ with a star-forming galaxy at redshift $z = 0.3532$. The second system is a post-starburst galaxy at redshift $z = 0.738$ and a quasar at redshift $z = 1.8039$. These objects may be interesting for follow-up observations to study strong gravitational lensing or absorption spectroscopy of outflows, for example.

Sample	Number of Objects
BOSS entire sample	3964
$z_{\text{fit}} = z_1$	3900 = 98.38%
SDSS entire sample	2330
$z_{\text{fit}} = z_1$	2194 = 94.16%
SDSS z_2 exists	2223
$z_{\text{fit}} = z_1$	2106 = 94.74%
$z_{\text{fit}} = z_2$	2153 = 96.85%
$z_{\text{fit}} = z_1$ but $z_{\text{fit}} \neq z_2$	47 = 2.11%
$z_{\text{fit}} = z_2$ but $z_{\text{fit}} \neq z_1$	94 = 4.23%
$z_{\text{fit}} = z_1 = z_2$	2059 = 92.62%
$z_{\text{fit}} \neq z_1 \neq z_2$	23 = 1.03%
SDSS z_2 does not exist	107
$z_{\text{fit}} = z_1$	88 = 82.24%

Table 2.4 The breakdown of our post-starburst galaxy sample in terms of whether the redshifts determined by the spectroscopic pipelines agree with those from our fitting procedure. In this table, z_1 indicates the `id1spec2d` redshift from the main spectroscopic pipeline (Bolton et al., 2012) which is available for both samples, while z_2 is the `spectro1d` redshift (SubbaRao et al., 2002), which is available for most of the SDSS I/II sample, but not for BOSS.

Selection Criteria	Number
Total	2330
Main Galaxy Sample	1462
All Galaxy	1879
Luminous Red Galaxy	140
Quasar	406
ROSAT	32
Stellar	30
Serendipitous	66

Table 2.5 The breakdown of our post-starburst galaxies sample from the SDSS I/II sample in terms of the spectroscopic target selection algorithms by which they are selected. The second row is the magnitude-limited main galaxy sample that we use in our luminosity function analysis. The other rows show the number of objects selected by various broad groups of selection algorithms. Note that a galaxy can be selected by more than one algorithm.

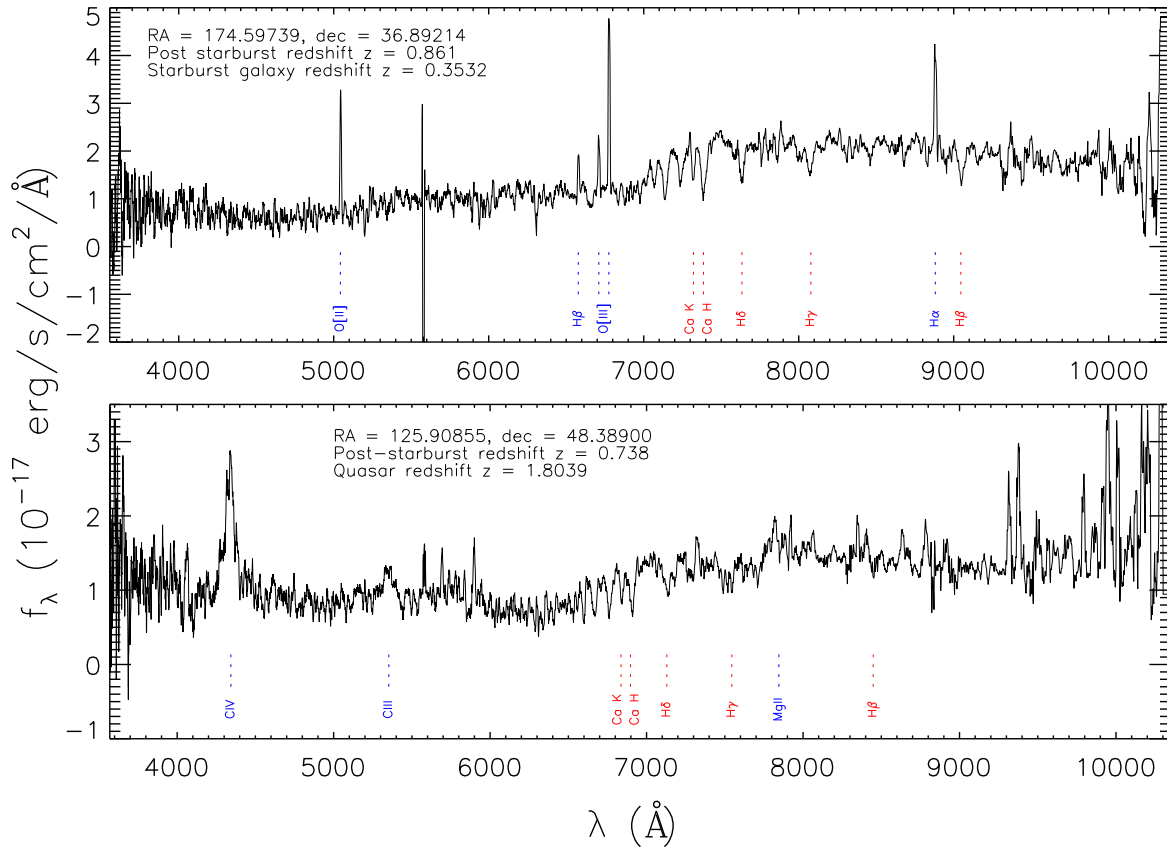


Figure 2.9 Two interesting objects that were discovered serendipitously because the pipeline redshifts and the fit redshifts disagree. They are actually pairs of objects along the same line of sight at different redshifts. The top panel shows a post-starburst galaxy at redshift $z = 0.861$ with a starforming galaxy at redshift $z = 0.3532$. The bottom panel is a post-starburst galaxy at redshift $z = 0.738$ with a quasar at redshift $z = 1.8039$. The features belonging to the post-starburst galaxies in each plot are indicated in red, while the ones belonging to the superposed objects are indicated in blue. These spectra are smoothed with a 10 pixel boxcar average to show the features clearly.

Selection Criteria	Number
Total	3964
CMASS sample	3475
Galaxy	3810
Quasar	72
Spectral Template	5

Table 2.6 The breakdown of our post-starburst galaxies sample from the BOSS sample in terms of the spectroscopic target selection algorithms by which they are selected. The second row is the CMASS sample with well-defined selection that we use in our luminosity function analysis. The other rows show the number of objects selected by various broad groups of selection algorithms. Note that a galaxy can be selected by more than one algorithm.

4.4 $H\alpha$ Equivalent Width

In our selection of this sample, we have neglected the $H\alpha$ line and only considered two lines ($H\delta$ in absorption and lack of $[OII]\lambda 3727$ in emission) since most of objects we select for are at high enough redshifts that the $H\alpha$ line is redshifted out of the wavelength coverage of the spectra. In order to compare this to other works and understand any biases the lack of selection in $H\alpha$ might introduce, we need to quantify how strong $H\alpha$ is in these objects. This exercise is important for two reasons. First is because $H\alpha$ line is commonly used as an indicator of star formation rate in most previous studies of E+A galaxies at low redshift. The second reason is that AGN is also known to produce $H\alpha$ emission, therefore can introduce selection biases. We address this concern with two different approaches.

The first one is to use our sample (mainly from SDSS-I/II) at low enough redshift that $H\alpha$ lies in the SDSS spectra. Figure 2.10 shows the distribution of $H\alpha$ equivalent width as a function of the absolute magnitude in the rest-frame [5000] band (this band is used later for luminosity function calculation; more detail in section 5.2) for the 1766 SDSS-I/II post-starburst galaxies at $z < 0.33$. Among these objects only 968 (54%) have $H\alpha EW > -3.0\text{\AA}$, the selection criterion adopted by Goto (2007). This means that nearly half of the sample at low redshift would be dropped as star forming if $H\alpha$ were taken into consideration, a rate consistent with what Goto (2007) found. However, if one limits the consideration to only the intrinsically luminous galaxies, the contamination is minimal. This can be seen from the subsample with absolute [5000]

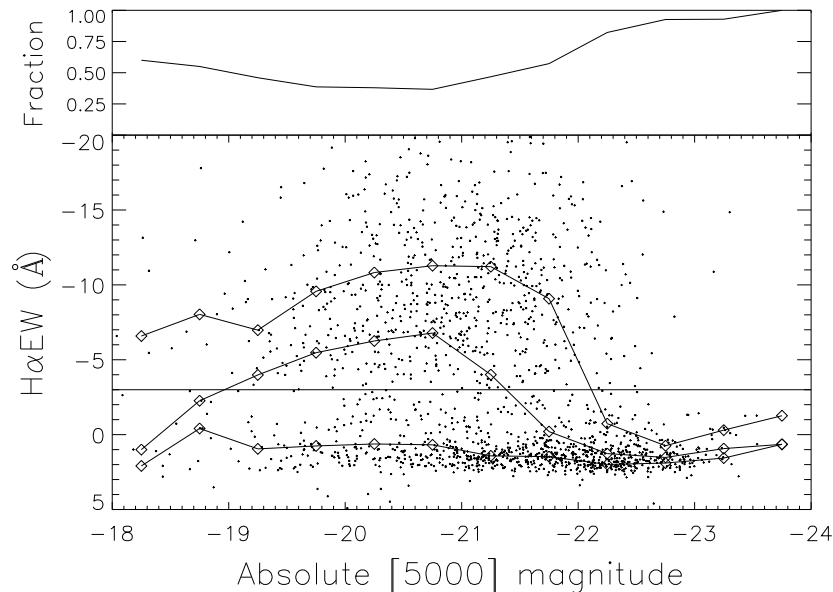


Figure 2.10 Rest frame $H\alpha$ Equivalent Width against the absolute magnitude in the [5000] band for post-starburst galaxies from SDSS I/II sample with redshift $z < 0.33$, selected irrespective of their $H\alpha$ properties. In the sign convention used here, positive EW is absorption. The horizontal line indicates the selection criteria $H\alpha EW > -3.0\text{\AA}$ used by Goto (2007). The three lines with square symbols are the 25, 50 and 75 percentiles of the objects in each half-magnitude bin respectively. The top panel shows the fraction of objects that pass the Goto (2007) selection criteria in each bin.

magnitude brighter than -22.5 . Out of 154 objects in this subsample, only 11 objects (7%) have $H\alpha EW > -3.0\text{\AA}$. Since most of our targets at high redshifts selected from BOSS are more luminous than $M \sim -22.5$ in the same band, and under the assumption that the post-starburst galaxies of the same intrinsic brightness have the same properties across cosmic time, we can extrapolate from this bright, low-redshift sample to conclude that our high-redshift sample from BOSS is minimally contaminated by our lack of $H\alpha$ information.

At the high-redshift end, we conducted follow-up Near-IR spectroscopic observations on a small number of objects to observe $H\alpha$ directly. We observed 10 objects at $z \sim 0.8$ with the TripleSpec Near Infrared spectrograph (Wilson et al., 2004) on the ARC 3.5m telescope at the Apache Point Observatory. The follow-up observations took place between November 2011 and November 2013, with details shown in Table 2.7. The targets were selected such that the $H\alpha$ line is expected to be in a region clear of telluric absorption, and to be as bright as possible for

Date observed	RA	DEC	Redshift	Exposure time
16 Nov 2011	01:36:11.85	+00:30:04.39	0.7886	48 mins
16 Nov 2011	02:49:56.15	-00:59:05.65	0.8270	56 mins
02 Jun 2012	16:46:24.77	+28:23:12.56	0.8560	64 mins
12 Jun 2012	12:32:54.27	+00:22:43.12	0.8499	40 mins
05 Sep 2013	21:15:33.74	+00:22:47.93	0.8338	84 mins
05 Sep 2013	01:13:33.06	+02:50:26.32	0.8980	92 mins
05 Sep 2013	02:29:24.93	-03:36:33.60	0.8520	56 mins
19 Nov 2013	21:20:56.53	+00:01:13.24	0.8381	76 mins
19 Nov 2013	23:51:41.07	+03:05:42.60	0.8570	60 mins
19 Nov 2013	02:08:51.52	+05:52:28.04	0.8269	104 mins

Table 2.7 Details of follow-up observations of high-redshift post-starburst galaxies using the Triple-Spec instrument at the Apache Point Observatory (APO) 3.5m telescope.

maximum signal-to-noise ratio. The exposure times were between 40 minutes and 104 minutes per object. The spectra were reduced using the publicly available software Triplespectool, which is a modified version of Spextool developed by Cushing et al. (2004). The software uses the telluric correction algorithm developed by Vacca et al. (2003).

The objects are clearly detected in the continuum, but are too faint to have good enough signal-to-noise ratio to detect the $H\alpha$ line either in absorption or emission. The composite spectrum of these objects at $H\alpha$ wavelength is shown in Figure 2.11 and the equivalent width of $H\alpha$ calculated from this composite using a simple estimate is $H\alpha EW \approx -4 \pm 6 \text{ \AA}$, consistent with zero. This lack of any clear detection is consistent with our low-redshift finding that luminous post-starburst galaxies selected only from $H\delta$ and $[OII]\lambda 3727$ are minimally contaminated by objects with large $H\alpha$ emission. The $[NII]\lambda 6584$ emission is detected in this composite spectrum with reasonable confidence. At face value, high $[NII]$ to $H\alpha$ ratio suggests that the spectrum is dominated by AGN. However, it is also possible that the $H\alpha$ absorption from post-starburst spectrum is offset by $H\alpha$ emission from an AGN component resulting in a non-detection in this line.

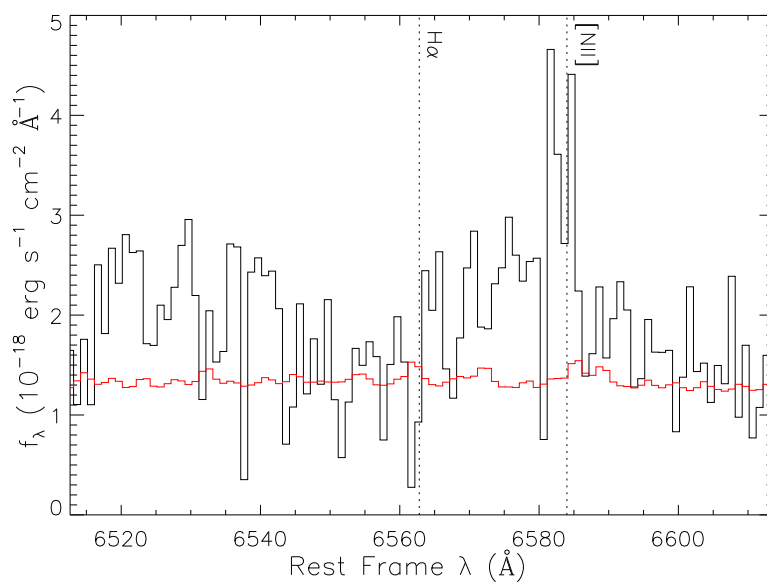


Figure 2.11 The composite spectrum around the wavelength of $H\alpha$ of 10 post-starburst galaxies that were observed by the TripleSpec instrument at the APO 3.5m telescope. The noise level is shown by the red line. The expected positions of $H\alpha$ and $[NII]\lambda 6584$ are shown by the dotted vertical lines. The continuum of these objects is clearly detected, but the signal-to-noise ratio is too low for $H\alpha$ to be seen either in emission or absorption. The $[NII]$ emission is detected with reasonable confidence.

4.5 Potential Biases in Selection

In this section, we discuss potential selection biases in our post-starburst galaxy sample. It is common to use the strength of [OII] λ 3727 and H α emission to measure star formation rate, in order to make cuts in these quantities and select objects with little or no ongoing star formation. However, AGN also produce emission in both lines. Therefore, when AGN is present, it is inevitable that biases are introduced when selecting sample using these lines.

In this work, we select post-starburst galaxies based on the H δ and [OII] lines; we discussed the bias due to not considering not considering H α line above in Section 4.4.

Objects that have intrinsically post-starburst stellar populations, but have significant [OII] emission due to AGN/LINERs (Yan et al., 2006) will be removed from the sample by the [OII] equivalent width cut. The degree of this bias is harder to quantify, since it can be difficult to distinguish galaxies that have post-starburst population with AGN and those with ongoing star formation, at least at the resolution and signal-to-noise ratio of SDSS spectra.

We note that the sample of post-starburst galaxies presented in this work is defined in a practical way, based on the equivalent widths of two lines. Therefore, it does not correspond exactly to the galaxy population whose stellar populations are intrinsically post-starburst, regardless of the presence of an AGN. In the luminosity function calculation in the next section, we attempt to carefully correct for these biases and check for self-consistency when possible.

Another source of bias is the incompleteness in the SDSS spectroscopic sample itself. About 5% of objects targeted for spectroscopy never had spectra taken (due to fiber collisions) or had spectra of particularly low signal-to-noise ratio. This incompleteness is a weak function of redshift and magnitude, since faint objects at high redshift tend to have lower signal-to-noise ratio. All luminosity functions calculated are divided by 0.95 to correct for this incompleteness.

5 Luminosity Function

5.1 Synthetic Spectrophotometry

In order to calculate the luminosity function, one needs the selection function, i.e., the probability of selecting a given galaxy as a function of redshift, given its luminosity and spectral shape. Given that we already have well-calibrated spectra for every object in our sample, we can synthesize the photometry of an object at any redshift by shifting the spectrum and scaling the brightness to that redshift, reconstructing the magnitudes and tracing through the selection criteria. This process automatically incorporates the k-correction and the dimming of objects with redshift (the inverse square law). We also quantified and corrected for the incompleteness due to changes in signal-to-noise ratio as a function of assumed redshift. The details of the process are as follows.

We calculate the synthesized magnitude in the g , r and i bands that a given galaxy would have, on a grid of redshift ranging from z_{\min} and z_{\max} (determined as the redshift range where the 3600-4400Å region would be inside the spectral coverage, as used in the post-starburst selection algorithm discussed earlier), with a grid spacing of $\Delta z = 0.001$. For each value on this redshift grid, the spectrum of the object is shifted, then integrated over each required band to find the average flux density over the band.

For the vast majority of assumed redshifts, the g , r and i filters fall within the observed spectral coverage. If not, we extrapolate the spectrum using the best-fit model from the spectroscopic pipeline (Bolton et al., 2012). In rare cases when even the model does not have the required spectral coverage, the magnitude is calculated from linear extrapolation from nearby redshift values.

This average flux density is then scaled to take into account the inverse square law by the multiplicative factor $\left(\frac{1+z_{\text{obs}}}{1+z_{\text{ass}}}\right) \left(\frac{D_L(z_{\text{obs}})}{D_L(z_{\text{ass}})}\right)^2$, where z_{obs} is the observed redshift of the object, z_{ass} is the assumed redshift at this particular gridpoint and $D_L(z)$ is the cosmological luminosity distance evaluated at these redshifts. The relationship between $D_L(z)$ and z is from the standard Λ CDM cosmology with $\Omega_M = 0.3$, $\Omega_\Lambda = 0.7$ and $H_0 = 70 \text{ km s}^{-1} \text{ Mpc}^{-1}$. This scaled average flux density is then turned into AB magnitude, with the Schlegel et al. (1998) galactic extinction of

the object in the same band corrected for. We call this class of magnitude derived from the spectrum the ‘‘Spectro’’ magnitude, as we described in section 2.2.

Next, these Spectro magnitudes in the g , r and i bands are converted into various other kinds of magnitudes that are used in the spectroscopic selection algorithms (section 4.2), namely the Model, Cmodel, Petrosian and Fiber magnitudes (section 2.2). This conversion is done for each kind of magnitude by applying the difference between the Spectro magnitude and that kind of magnitude at the observed redshift. This single-valued conversion is justified because at the redshifts relevant for the CMASS sample, the angular diameter distance is a slowly changing function of redshift. The appearances of the images observed, except for brightness, are relatively constant, therefore the difference between families of magnitudes that arise from different ways to process this image should not change very much with redshift. Once this process is done, we have derived magnitudes in the g , r and i bands that the object would appear photometrically as a function of redshift. At the lower redshift range relevant to SDSS I/II sample, the justification that the angular-diameter distance is a slowly changing function of redshift is no longer true, and the use of the single-valued correction might be less justified. However, we still expect that it is largely valid given the small redshift range ($\Delta z \sim 0.2$) involved.

5.2 Magnitude and Color in Fiducial Bands

In order to compare intrinsic luminosities of objects over a range of redshift, the magnitudes in the observed bands are not sufficient, since they sample different parts of the spectrum at different redshifts, and thus need to be k-corrected. For this purpose, we calculate the absolute AB magnitude in two fiducial top-hat bands fixed in rest-frame wavelength from the spectra for all our objects from the SDSS I/II and BOSS samples. The first is the fiducial band we have introduced before; it lies between 4150\AA and 4300\AA , sampling the continuum between the $H\gamma$ and $H\delta$ lines. The other band is between 4950\AA and 5100\AA . As introduced earlier, we will refer to these bands as the [4200] and [5000] bands respectively. These two wavelength ranges roughly represent the wavelength coverage for the r and i bands at redshift $z \sim 0.5$, and lie in continuum regions without strong absorption lines. The magnitude in the [4200] band is available for every

object in our sample, because our selection process guarantees that this rest-frame wavelength is covered in the spectrum. The same is not true for the [5000] band, since it is shifted outside the spectral coverage for redshift greater than around unity. However, galaxies in subsamples with homogeneous selection that we will use to calculate the luminosity function (the SDSS Main Galaxy Sample and the BOSS CMASS Sample) do not extend to such high redshift, so this is not an issue.

For each band, the averaged flux density \bar{f}_λ in the band is calculated from the spectrum, then scaled to 10 parsec by the factor $(1+z) \left(\frac{D_L(z)}{10\text{pc}}\right)^2$ for the calculation of absolute magnitude. The AB magnitude is then derived. This Spectro magnitude is then converted to Cmodel magnitude using the observed difference between Cmodel and Spectro magnitude from the SDSS bands, and interpolated to the wavelength where the fiducial band under consideration lies at the observed redshift. Galactic extinction is corrected in the same manner, using the extinction in SDSS bands interpolated to the appropriate wavelength where the fiducial band lies.

Figure 2.12 shows the scatter plot between this absolute magnitude in the [5000] band and redshift of the objects, together with the respective approximate selection limit, in both the SDSS I/II and BOSS samples. The selection limits are calculated from the coadded spectrum of the sample, showing the absolute magnitude corresponding to when the spectrum is scaled to match the selection limits of the respective surveys. Even before calculating the luminosity function properly, this plot gives a number of qualitative insights into the luminosity function of these two subsamples of post-starburst galaxies.

First of all, there is a dramatic difference between the luminosity ranges over which the post-starburst galaxies lie at low and high redshift, as seen by comparing the SDSS Main Galaxy sample and the BOSS CMASS sample. The low-redshift sample ranges from -19 to -23 magnitude, while the high-redshift sample ranges from -22 to -24 magnitude and even brighter. It is noteworthy that there are very few low-redshift post-starburst galaxies brighter than -23 magnitude, even though if luminous galaxies existed at low redshift they would certainly have been observed and selected into the sample. From this, we expect that the number density of

luminous post-starburst galaxies at high redshift is significantly higher than that at low redshift; this is a downsizing trend.

This trend can also be seen within the low and high redshift sample separately. For example, at redshift $z \sim 0.1$ there are fewer galaxies at -23 magnitude than at redshift $z \sim 0.2$, and also at redshift $z \sim 0.55$ there are fewer galaxies at -23.5 magnitude than at $z \sim 0.75$. Therefore we expect just from this plot that the luminosity functions of post-starburst galaxies as a function of redshift should show a downsizing trend. In other words, luminous post-starburst galaxies are more abundant at higher redshift.

It is also noteworthy that the post-starburst galaxies selected from the BOSS CMASS sample have systematically higher redshift than the overall CMASS galaxies; the median redshift of CMASS post-starburst galaxies is $z \sim 0.63$, while that of the whole CMASS sample is $z \sim 0.57$. This is likely due to systematic difference in the SEDs of post-starburst galaxies and the generic elliptical galaxies which are the main target of CMASS color selection.

5.3 SDSS Main Galaxy Sample

The SDSS Main Galaxy Sample is simply a magnitude-limited at $r_{\text{petro}} < 17.77$. For each of our post-starburst galaxies from the SDSS Main Galaxy Sample, we use the Petrosian magnitude as a function of assumed redshift calculated from the spectrum to determine the redshift range over which this galaxy would be selected into the SDSS spectroscopic sample. Because our spectra extend to 3800 \AA , we can only select post-starburst galaxies at $z > 0.02$. Once the redshift range over which the galaxy would be selected is known, the volume V_{max} for this galaxy is calculated by integrating the cosmological volume within this range, with the solid angle of the SDSS DR7 spectroscopic survey of 8032 degree^2 taken into account. The luminosity function of post-starburst galaxies from the SDSS Main Galaxy Sample is then calculated using the standard $1/V_{\text{max}}$ method. Finally, this luminosity function is divided by a factor of two at magnitudes fainter than $M \sim -22$ to statistically take into account the contamination from objects with strong $\text{H}\alpha$ emission (see section 4.4 and Figure 2.10). It is worth noting that this correction may overcorrect for the contamination at faint magnitudes, since some objects might have intrinsically

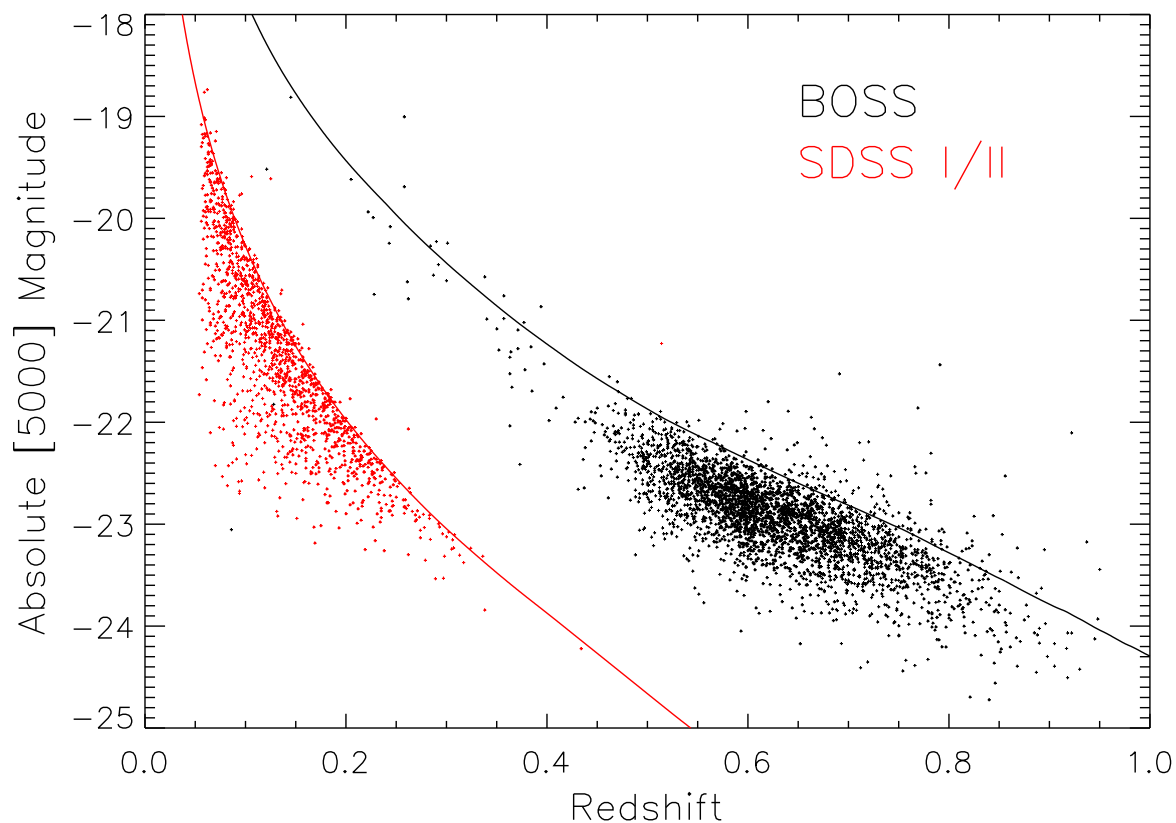


Figure 2.12 Absolute magnitude in the fiducial band [5000] against redshift for our post-starburst galaxies from both the SDSS Main Galaxy sample (red) and the BOSS CMASS sample (black). The solid lines show the corresponding selection limits of each sample for the mean SED ($r_{\text{petro}} < 17.77$ for SDSS and $i_{\text{cmodel}} < 19.9$ for BOSS). These lines are calculated from the coadded spectrum of the sample, such that they show the absolute magnitude in the [5000] band when the spectrum is scaled to match the selection limits of the respective surveys at each value of redshift. Note that these selection lines are not hard cuts, and the fact that some objects lie above the lines is due to the variation in the SEDs from the average.

post-starburst stellar populations, but with AGN causing its removal from the sample. The sample is split into two redshift bins with roughly the same number of objects at $z = 0.12$ (with the volume V_{\max} limited to the corresponding redshift bin). The resulting luminosity function for galaxies in this sample for both redshift bins (along with that of the CMASS sample, see next section) are shown in Figure 2.18.

5.4 BOSS CMASS Sample

For the BOSS CMASS sample, the spectroscopic target selection criteria are designed to select an approximately volume-limited sample of galaxies in the range $0.4 < z < 0.7$ to measure Baryon Acoustic Oscillations in their clustering (Anderson et al., 2012). CMASS stands for “Constant Mass”, and the following criteria are designed to be crude cuts in both photometric redshift and stellar mass, isolating objects with mass $> 10^{11} M_{\odot}$. These selection criteria are

$$17.5 < i_{\text{cmod}} < 19.9 \quad (2.2)$$

$$r_{\text{mod}} - i_{\text{mod}} < 2.0 \quad (2.3)$$

$$d_{\perp} = r_{\text{mod}} - i_{\text{mod}} - (g_{\text{mod}} - r_{\text{mod}})/8.0 > 0.55 \quad (2.4)$$

$$i_{\text{fib2}} < 21.5 \quad (2.5)$$

$$i_{\text{cmod}} < 19.86 + 1.6(d_{\perp} - 0.8), \quad (2.6)$$

with two additional star-galaxy separation cuts

$$i_{\text{psf}} - i_{\text{mod}} > 0.2 + 0.2(20.0 - i_{\text{mod}}) \quad (2.7)$$

$$z_{\text{psf}} - z_{\text{mod}} > 9.125 - 0.46z_{\text{mod}}. \quad (2.8)$$

The star-galaxy separation cut is used to select extended sources by comparing the PSF magnitudes to the model magnitudes. Due to the slowly varying nature of the angular diameter distance with redshift for the relevant redshift range of this sample, we expect that any object

that satisfies the star-galaxy separation at its observed redshift and enters the CMASS sample in the first place would also satisfy these conditions over the entire redshift range. Therefore we do not consider these cuts from our calculation of the selection function.

However, some post-starburst galaxies may be unresolved, and thus not targeted at all by CMASS. Indeed, $\sim 2\%$ of our objects are targeted as unresolved quasar candidates, but this fraction is small enough not to alter the luminosity function results significantly. We therefore calculate the luminosity function only from objects selected as CMASS galaxies.

The distribution of objects in our sample in the various color-magnitude spaces probed by these criteria are shown in Figure 2.13. It can be seen that the three most restrictive conditions for our samples are $i_{\text{cm}od} < 19.9$, $d_{\perp} > 0.55$ and $i_{\text{cm}od} < 19.86 + 1.6(d_{\perp} - 0.8)$.

Another potential selection bias that should be noted is the fact that our selection method is designed to target relatively older post-starburst galaxies, leading to incompleteness in the blue end of the sample (as discussed earlier in Section 3.2). For the BOSS CMASS subsample, which is designed to target red, luminous galaxies through this color selection, this effect might add extra incompleteness to the blue, faint end of the sample.

We use the prediction of brightness as a function of assumed redshift based on the observed SED (see Section 5.1) to find the redshift range over which all criteria are satisfied, as demonstrated in Figure 2.14. This range corresponds to the redshifts that the object would still be selected into the spectroscopic sample and subsequently our post-starburst galaxy sample. We also calculate the effects of finite signal-to-noise ratio on our selection function for each galaxy. This completeness fraction, $C(z)$, is defined as a fraction of times that a specific spectrum will still be selected as a post-starburst galaxy by our $A/\text{Total} > 0.25$ criterion after adding random noise at the appropriate level. In this calculation, we use the best-fit template between rest-frame 3600-4400Å range, scaled for cosmological dimming, as the “noiseless model”, while the noise is taken from the sky background at the wavelength range corresponding to rest-frame 3600-4400Å at that redshift. For majority of objects, the completeness fraction $C(z)$ remains at unity over the relevant redshift ranges. This noise model is appropriate because at these magnitudes, the sky noise completely dominates over the photon noise from the object itself. The volume V_{max} is then

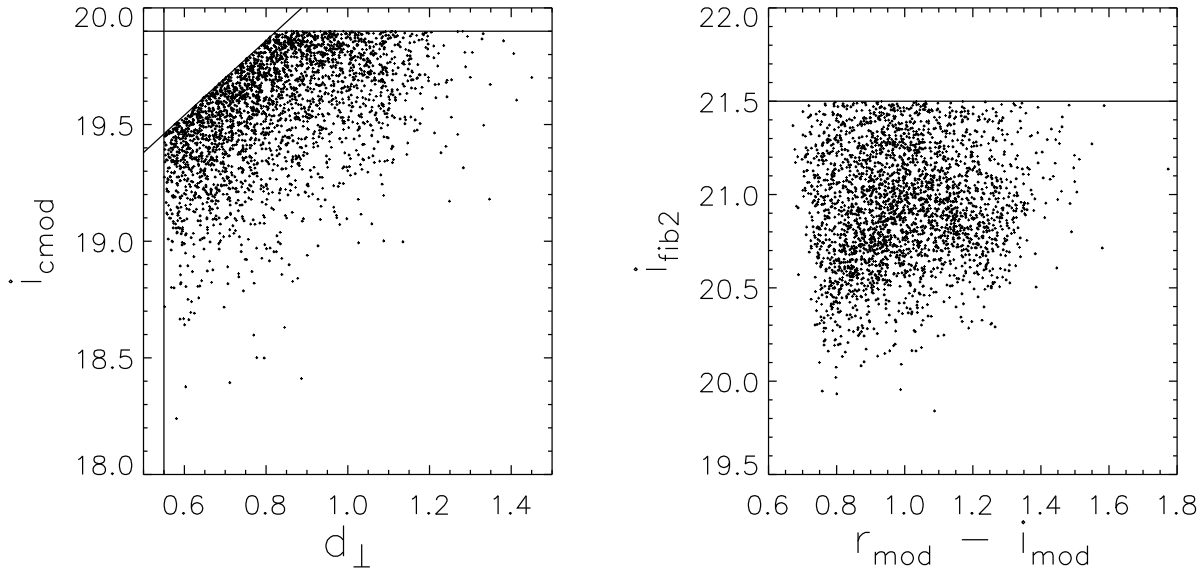


Figure 2.13 Our post-starburst galaxies from the BOSS CMASS sample shown against the CMASS selection criteria. The left panel shows the distribution of the Cmodel i -band magnitude against the color d_{\perp} . The lines shown are the relevant selection criteria $i_{\text{cmod}} < 19.86 + 1.6(d_{\perp} - 0.8)$, $i_{\text{cmod}} < 19.9$ and $d_{\perp} > 0.55$, with $i_{\text{cmod}} > 17.5$ off the scale. The right panel shows the Fiber2 i -band magnitude against the $r-i$ color. The selection line shown is $i_{\text{fib2}} < 21.5$, with $r_{\text{mod}} - i_{\text{mod}} < 2$ off the scale. All colors and magnitudes plotted here are corrected for the Schlegel et al. (1998) galactic extinction.

calculated as

$$V_{\text{max}} = \frac{\Omega}{4\pi} \int_{z_{\text{min}}}^{z_{\text{max}}} C(z) dV,$$

where Ω corresponds to the solid angle of the BOSS survey up to SDSS DR9, 3275 deg². In cases that we calculate the luminosity function in a redshift bin, this volume V_{max} is further restricted to be only the volume that overlaps with that redshift bin.

Even after the volume V_{max} is known, simply summing the inverse of this volume in bins of magnitudes is not sufficient to get an unbiased luminosity function. This is due to a consequence of the CMASS color selection that not all SEDs are selected at all luminosities. We now describe the process we adopt to correct for this effect.

Figure 2.13 shows the selection of the CMASS galaxies in observed quantities, but in order to obtain a physically meaningful measure of the luminosity function, we need to work in terms of

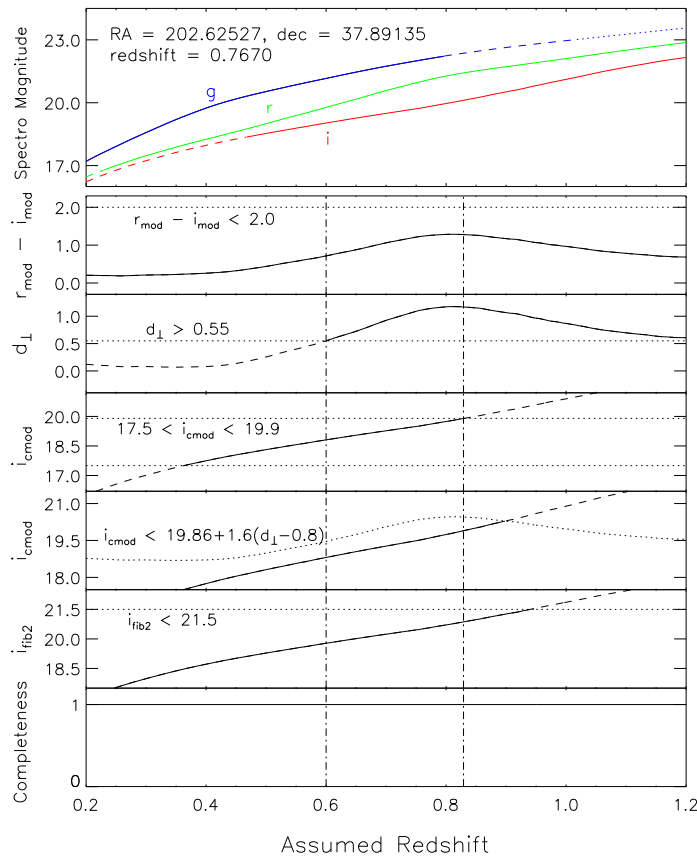


Figure 2.14 Example to demonstrate our method to calculate V_{max} for a specific BOSS CMASS galaxy. The spectrum of this object is shown in Figure 2.2. The top panel shows the Spectro magnitude in each of the g , r and i bands that the object would appear to have at any assumed redshift. The solid lines correspond to the redshift ranges over which the magnitude can be calculated directly from the spectrum. Dashed lines correspond to the redshift ranges where the magnitudes are calculated from the best-fit template because the wavelength coverage of the spectrum does not cover the band. The dotted lines correspond to the redshift range where neither the spectrum or the template fit covers the band, and the magnitude is simply extrapolated. The lower five panels show relevant selection criteria used by CMASS evaluated in this redshift range. Various kinds of magnitudes are converted from the Spectro magnitude, with extinction taken into account. The relevant quantities in each panel are shown by the solid line in the redshift range where the criteria is met, and dashed line otherwise. The bottom panel shows the completeness fraction as a function of redshift. This parameter is the fraction of times that this spectrum, with random noise at appropriate level added, will be selected by template fitting as post-starburst galaxy. This is derived with Monte Carlo calculation, with details described further in the text. We note that for this object and most objects in our sample, the completeness remains at unity throughout the relevant redshift range, indicative of sufficient signal-to-noise ratio to be unambiguously selected. The horizontal dotted lines show the selection thresholds. The vertical dash-dotted lines indicate the redshift range where all five selection criteria are met simultaneously, corresponding to the redshift range within which this object will still be selected into the CMASS sample.

Survey	Redshift Range	Total Number	After Fiducial Selection Cuts	Median Redshift
SDSS Main Galaxy	All Redshift	1462	1462	0.124
SDSS Main Galaxy	$z < 0.12$	696	696	0.091
SDSS Main Galaxy	$z > 0.12$	766	766	0.160
BOSS CMASS Galaxy	All Redshift	3475	2867	0.624
BOSS CMASS Galaxy	$z < 0.55$	649	437	0.521
BOSS CMASS Galaxy	$0.55 < z < 0.65$	1462	1331	0.599
BOSS CMASS Galaxy	$0.65 < z < 0.75$	1039	900	0.689
BOSS CMASS Galaxy	$z > 0.75$	325	199	0.786

Table 2.8 Details of redshift bins in the luminosity function calculation of the BOSS CMASS sample. The first and second columns are the survey and redshift range respectively. The third column is the total number of objects selected into each respective sample in these redshift ranges. The fourth column is the number of objects actually used in the luminosity function calculation. For the SDSS I/II sample, these two columns are the same. For the BOSS CMASS sample, there is an additional requirement for objects to pass the fiducial selection cuts defined in term of intrinsic properties described in the text. The last column shows the median redshift of all objects in the third column.

the intrinsic, rest-frame properties of the galaxies. We measure these intrinsic quantities by using the two fiducial bands at 4200\AA and 5000\AA that we introduced earlier. Note again that these two bands lie at the approximate wavelengths of the r and i bands at redshift $z = 0.5$, and the quantity d_{\perp} is dominated by r and i . Therefore we expect that the selection criteria in terms of $i_{\text{cm}od}$ and d_{\perp} should translate roughly to cuts in the $[5000]$ and $[4200] - [5000]$ plane. Figure 2.15 shows this plane; galaxies are indeed roughly bounded by the cuts shown. We see that the color distribution of galaxies in this space becomes increasingly restricted fainter than $M = -23.0$, which would introduce biases in the luminosity function if not corrected for. In this parameter space, we define the selection lines to be $-24.1 < [5000] < -22.2$, $0.2 < [4200] - [5000] < 1.2$ and $[5000] < -23.3 + 1.8([4200] - [5000])$. These selection lines are drawn arbitrarily to have a similar form to the CMASS selection in observed quantities, with values such that they roughly represent the distribution in Figure 2.15. In order to have a uniformly selected sample, we do not include any galaxy that falls outside this range in our luminosity function analysis. Figure 2.16 shows the distribution in this parameter space but separated into different redshift bins. For the BOSS CMASS sample, populations at different redshifts fall into different region of this parameter space, but remain bound by the fiducial selection cuts.

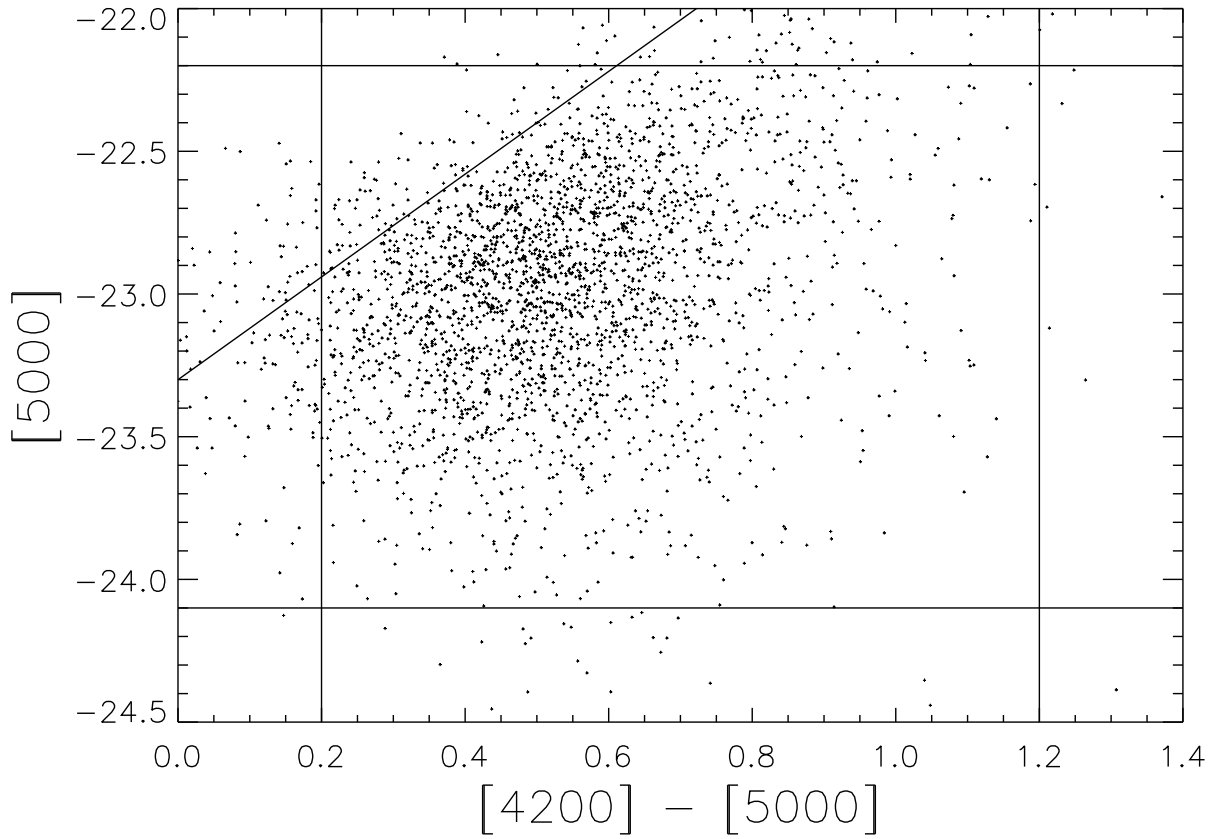


Figure 2.15 Our post-starburst galaxies from the BOSS CMASS sample at all redshifts, shown in rest-frame absolute magnitudes and colors calculated from the spectra. The solid lines shown are the selection cuts in this parameter space corresponding roughly to the CMASS selection in term of i and d_{\perp} at redshift $z \sim 0.5$. At magnitude fainter than $M \sim -23$, the color-dependent magnitude cut introduces an additional selection bias in the luminosity function calculation.

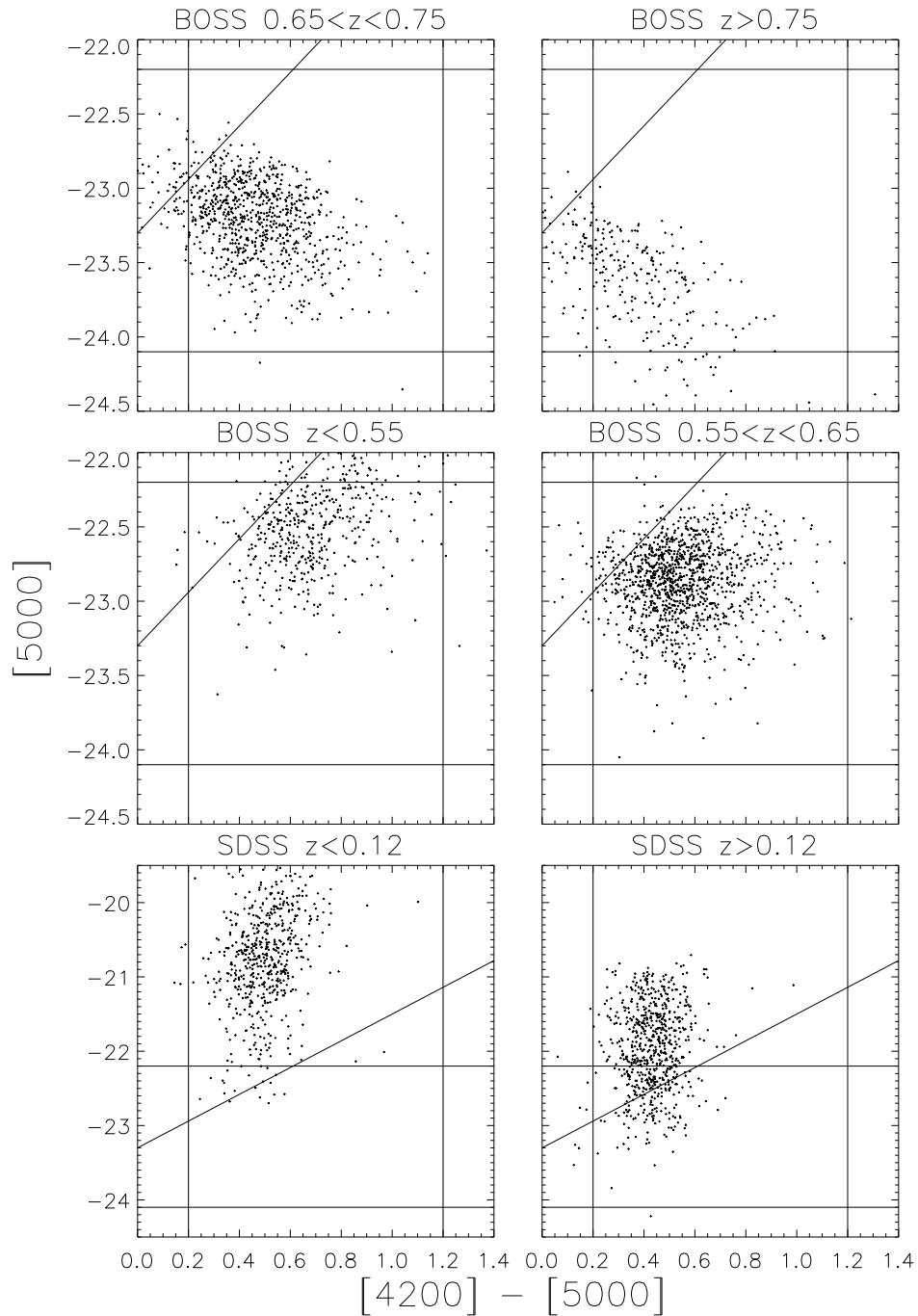


Figure 2.16 Distribution of our post-starburst galaxies in rest-frame magnitudes and colors similar to Figure 2.15, but separated into redshift bins. The top four panels show the BOSS CMASS sample, along with the selection cuts in these quantities. Only objects that pass these selection cuts are used to calculate the luminosity functions. The lower two panels show the equivalent plot for the SDSS I/II Main Galaxy sample. The selection cuts used in BOSS sample is shown only for comparison, but are not used since this sample is not subject to the CMASS selection.

This correction works under the assumption that the distribution of number density of galaxies is a separable function of magnitude and color. Thus knowing the distribution of galaxies in the red portion of the sample, where the sample is complete, allows one to extrapolate and determine the number density in the blue part where the sample is biased against faint objects. The same argument also applies the other way around, allowing one to use the luminous portion of the sample, which is complete in color, to determine the number density at the fainter part where blue objects are biased against. The validity of this assumption is shown in Figure 2.17, where the number densities (sum of $1/V_{\max}$) for the sample are shown for a number of bins in both magnitude and color. The distributions in different bins, once normalized, are the same at the bright and red portions of the sample where the selection is complete. This property of the distribution allows us to infer the number density of objects in the region of parameter space where the selection is incomplete from the region where the selection is complete. The number of objects are at least a few tens in bins near the cutoff line, therefore small number statistics should not have a major effect in the conclusion that the number density is a separable function in color and magnitude.

The correction for this incompleteness is as follows. We define a relevant color-magnitude parameter space given by $C = [5000] - [4200]$ and $M = [5000]$. For each gridpoint in this parameter space, we define the distribution $D(M, C)$ such that $D(M, C)\Delta M\Delta C$ is the comoving number density of post-starburst galaxies with color between C and $C + \Delta C$ and magnitude between M and $M + \Delta M$, which is calculated by summing the inverse V_{\max} of all galaxies belonging to that gridpoint.

The number density in grid points that are excluded by the selection can then be predicted using the assumption that the distribution is a separable function in magnitude and color. The number density in an excluded grid point, written as $D_{\text{incomplete}}(M, C)$, can be computed from the total number density in three different regions of the parameter space: the part of the parameter space at the same color but bright enough to be complete $[\int_{-\infty}^{M_{\text{crit}}} D(M', C)dM']$, the part at the same magnitude but with color red enough to be complete $[\int_{C_{\text{crit}}}^{\infty} D(M, C')dC']$, and the part that is both red and bright enough $[\int_{-\infty}^{M_{\text{crit}}} \int_{C_{\text{crit}}}^{\infty} D(M', C')dC'dM']$. The ratio of the first

and third quantities represent the ratio of number density at the specific value of color at that grid point to the total number density at color redder than the cutoff, measured at magnitude bright enough to be complete. This ratio should be the same as the ratio between $D_{\text{incomplete}}(M, C)$ and the second quantity, since the ratio of number densities in two color ranges should be independent of magnitude based on the assumption that the distribution is separable in color and magnitude. This yields the final expression of $D_{\text{incomplete}}$:

$$D_{\text{incomplete}}(M, C) = \frac{\int_{C_{\text{crit}}}^{\infty} D(M, C') dC' \int_{-\infty}^{M_{\text{crit}}} D(M', C) dM'}{\int_{-\infty}^{M_{\text{crit}}} \int_{C_{\text{crit}}}^{\infty} D(M', C') dC' dM'}. \quad (2.9)$$

Here M_{crit} is the magnitude where the diagonal selection line in Figure 2.15 crosses the blue color limit $C = 0.2$, yielding $M_{\text{crit}} \sim -23$. The value of C_{crit} is the color cutoff above which the selection is complete. This value depends on the value of magnitude being considered, given by $C_{\text{crit}} = \max(0.2, (M + 23.3)/1.8)$. For gridpoints that are on the selection cut and are partially excluded, we calculate the number density distribution by combining the information from objects in the complete part with the predicted distribution for the incomplete part, both weighted by the respective area of their parts in the cell.

Once the distribution function over the grid has been determined, the luminosity function can be calculated simply by integrating over the colors

$$\Phi(M) = \int_{-\infty}^{\infty} D(M, C') dC' \quad (2.10)$$

where $D(M, C)$ is now the distribution in both color and magnitude corrected for incompleteness from the selection.

The luminosity function is calculated for our post-starburst galaxies from BOSS CMASS in four different redshift bins. The number of objects in each redshift bin is shown in Table 2.8. The error bar in the luminosity function is calculated using Poisson statistics (and does not take into account systematic errors in the correction for color incompleteness).

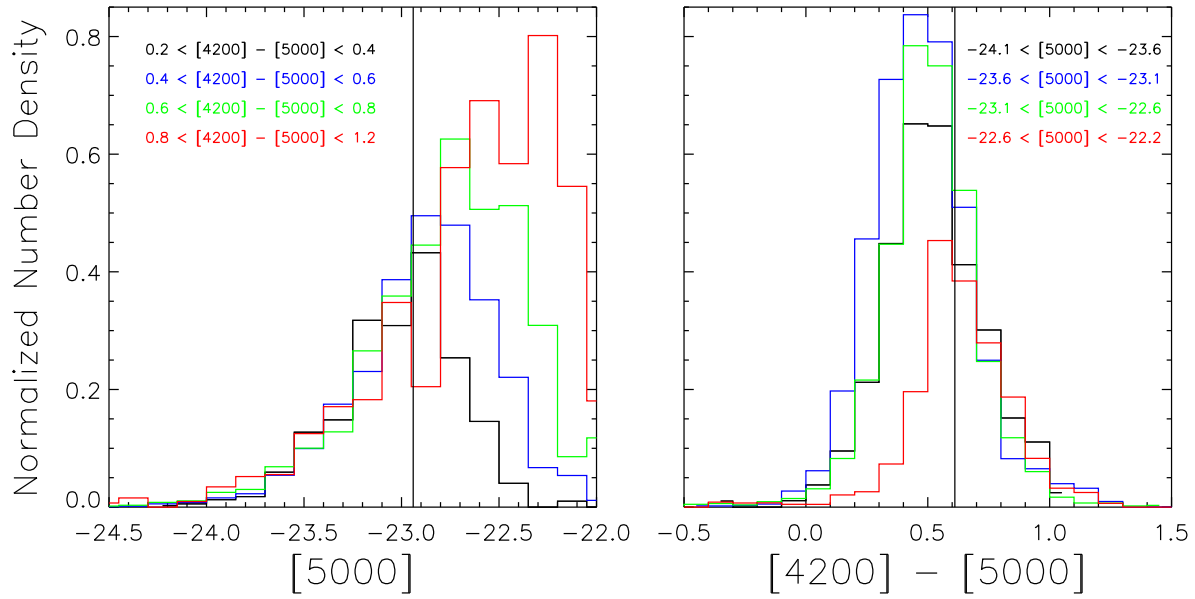


Figure 2.17 The relative distributions of the number density of galaxies ($\Sigma(1/V_{\max})$) as a function of color and magnitude. Left panel: the relative distribution as a function of magnitude for different colors, normalized such that the total numbers of galaxies brighter than M_{crit} (vertical line) is the same for each color bin. Right panel: distribution as a function of colors for different magnitudes, normalized such that total numbers of galaxies redder than C_{crit} are the same for each magnitude bin. With this normalization, the curves are approximately coincident where the distributions are complete, showing that the distributions of galaxies in color and magnitude are indeed approximately separable and independent.

Figure 2.18 shows the resulting luminosity functions of BOSS CMASS post-starburst galaxies for all four redshift bins, as well as those calculated from the SDSS I/II sample in two redshift bins.

These luminosity functions are quite different in different redshift bins; we see strong evidence for redshift evolution. The downsizing trend can be seen in two ways from this plot. The first is that the magnitude where the luminosity function peaks becomes progressively more luminous for higher redshift. This indicates that the typical post-starburst galaxies at higher redshift are more luminous than at lower redshift. However, selection biases can be important here, because the peak magnitudes in each redshift bin are very close to the cutoff magnitudes. We discuss a posteriori tests of the luminosity function below in section 5.5.

The second way to see the downsizing trend, which is less affected by the selection biases, is to compare number densities of post-starburst galaxies at fixed magnitude for different redshift bins. For example, at $M = -23.5$ the number densities for different redshift bins gradually decrease from $z \sim 0.7$ to $z \sim 0.5$, while the two low-redshift bins of SDSS have almost no galaxies at that magnitude, even though they would have been observed and selected if they exist. The exception to this trend is the highest-redshift bin ($z > 0.75$) which has the smallest number of galaxies but suffers from the largest selection biases.

This way of viewing the downsizing trend is shown in Figure 2.19. The number densities at fixed luminosity are shown as a function of redshift. The information used in this plot is the same as that in Figure 2.18, using magnitude bins of size $\Delta M = 0.5$. For each luminosity, the number density of post-starburst galaxies increases strongly with redshift, by more than an order of magnitude from $z = 0.1$ to $z = 0.6$ in the case of the sample at $M = -23$, while at fixed redshift, the fainter objects are more numerous. The exception to these trends are again the highest-redshift bin and lowest luminosity bin, both of which are likely to be affected the most by selection effects.

We compared the luminosity function in our lowest redshift bin to that of Quintero et al. (2004), which is calculated for low-redshift SDSS post-starburst galaxies in the $^{0.1}i$ -band. After correcting for the fact that different bands are used, these luminosity functions agree reasonably

well to about a factor of 2. We also compared the luminosity function in the highest redshift bin to that of Wild et al. (2014), which is calculated at $z \sim 1$ at rest-frame $1\mu\text{m}$ in the UDS field, then extrapolated to the K -band. This luminosity function is higher than ours by about a factor of 5, but given the significant difference in the selection methods and wavelength ranges used, this difference is not a major source of concern.

The luminosity functions of BOSS CMASS galaxies are then fitted to Gaussian functions in magnitude (log-normal in luminosity) with inverse-variance weights. The fitting function is

$$\Phi(M) = A \exp \left[-\frac{(M - M_0)^2}{\sigma^2} \right] \quad (2.11)$$

The two free parameters in this fit are the normalization A and the peak magnitude M_0 , while the width of the Gaussian σ is fixed to be 0.4 magnitude at all redshifts; empirically, the width is very close to constant. With σ fixed, the normalization A is proportional to the total number density in each redshift bin. The fit parameters as functions of median redshift of the bins, along with a linear fit of these parameters as a function of redshift, are shown in Figure 2.20. This plot shows the trend that we already described; the overall normalization decreases while the peak magnitude becomes brighter at higher redshift.

5.5 Self-Consistency Test of Luminosity Function from the BOSS CMASS Sample

The validity of the luminosity function is tested in this section with the method described in, for example, Sandage et al. (1979) and Koranyi & Strauss (1997). Given the measured luminosity function and the observed redshift and SED of each galaxy, one can predict what the luminosity distribution of the galaxies in the sample would be, with color and magnitude selection taken into account. The predicted luminosity distribution can then be compared to the observed one. If the sample is uniform and the measurement is done consistently, the predicted and observed luminosity distributions should agree well.

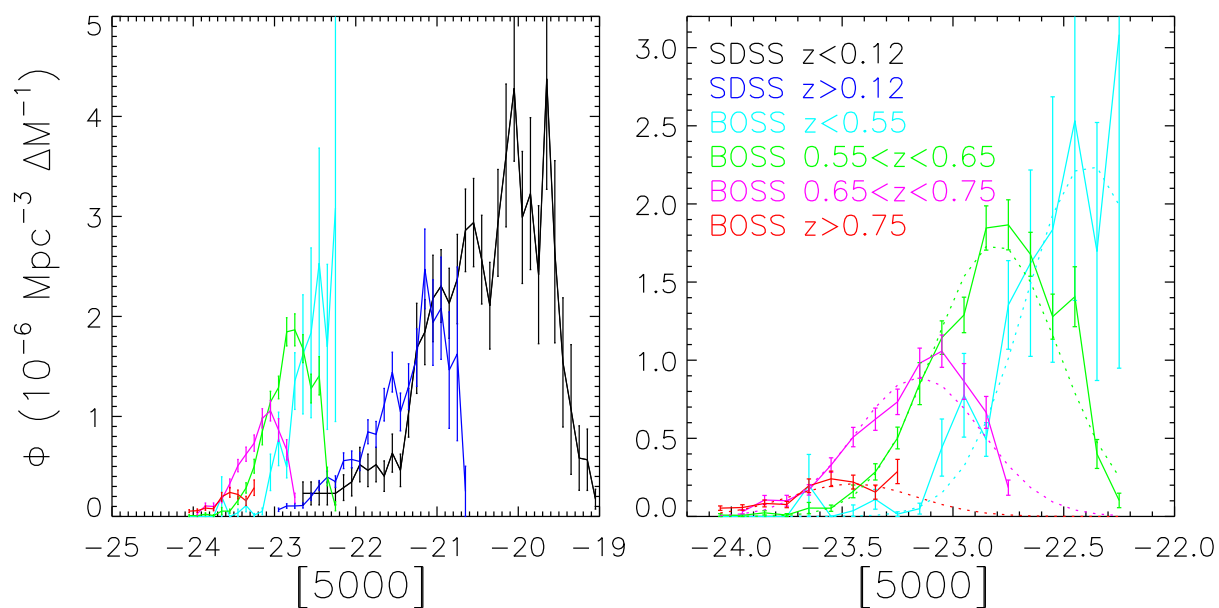


Figure 2.18 Left panel: Luminosity functions of the post-starburst galaxy sample from both SDSS I/II and BOSS samples for each of our redshift bins. Right panel: The same luminosity functions but only for the BOSS sample, with the same color-coding as the left panel. The Gaussian fits to the luminosity function for BOSS sample are shown as dashed lines. Error bars shown are Poisson.

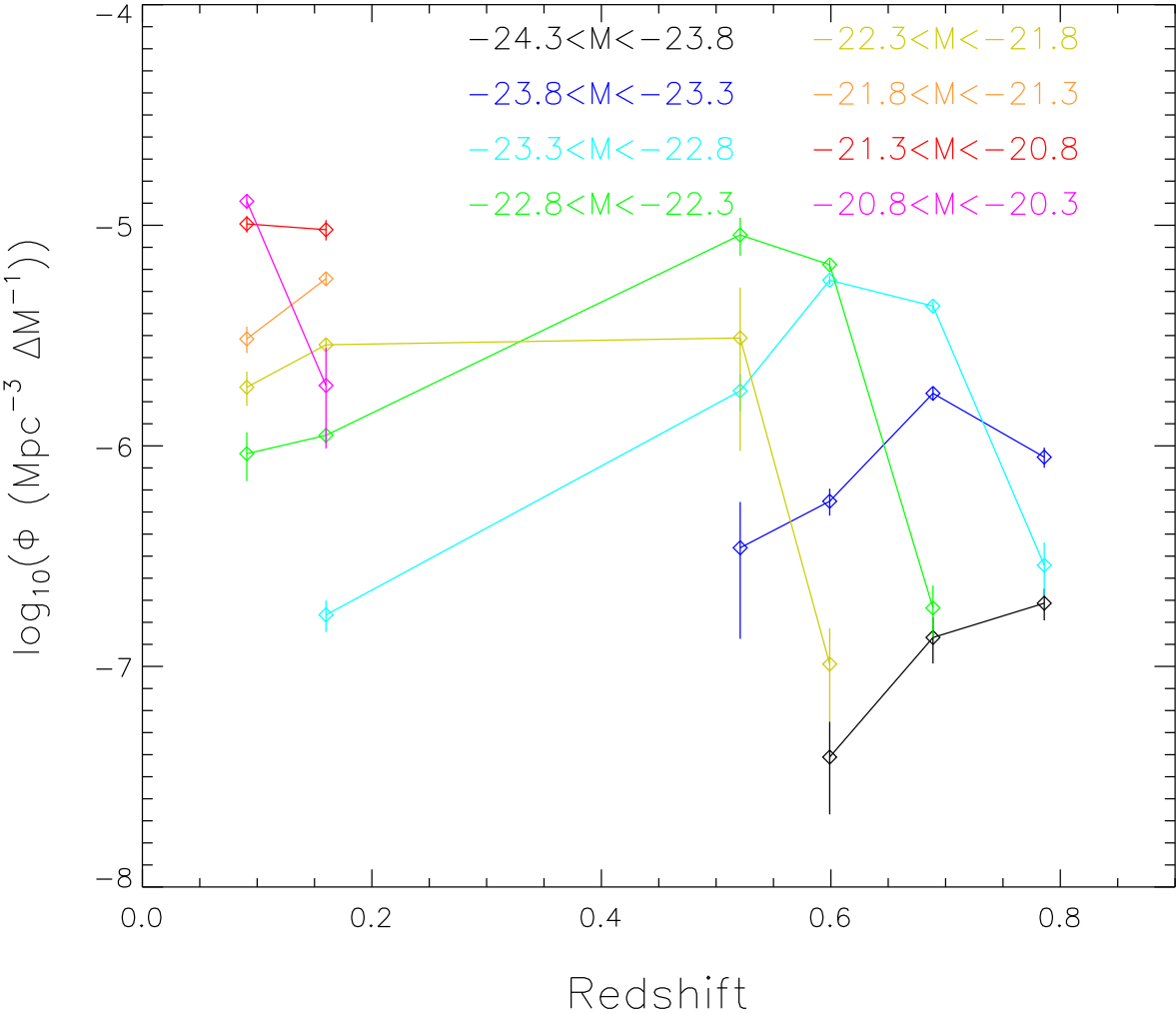


Figure 2.19 Number density as a function of redshift at fixed luminosity. Each line corresponds to the range of luminosity indicated in the legend, all with width $\Delta M = 0.5$. The error bars are Poisson. This plot contains the same information as in Figure 2.18 but re-binned in luminosity and plotted as a function of redshift.

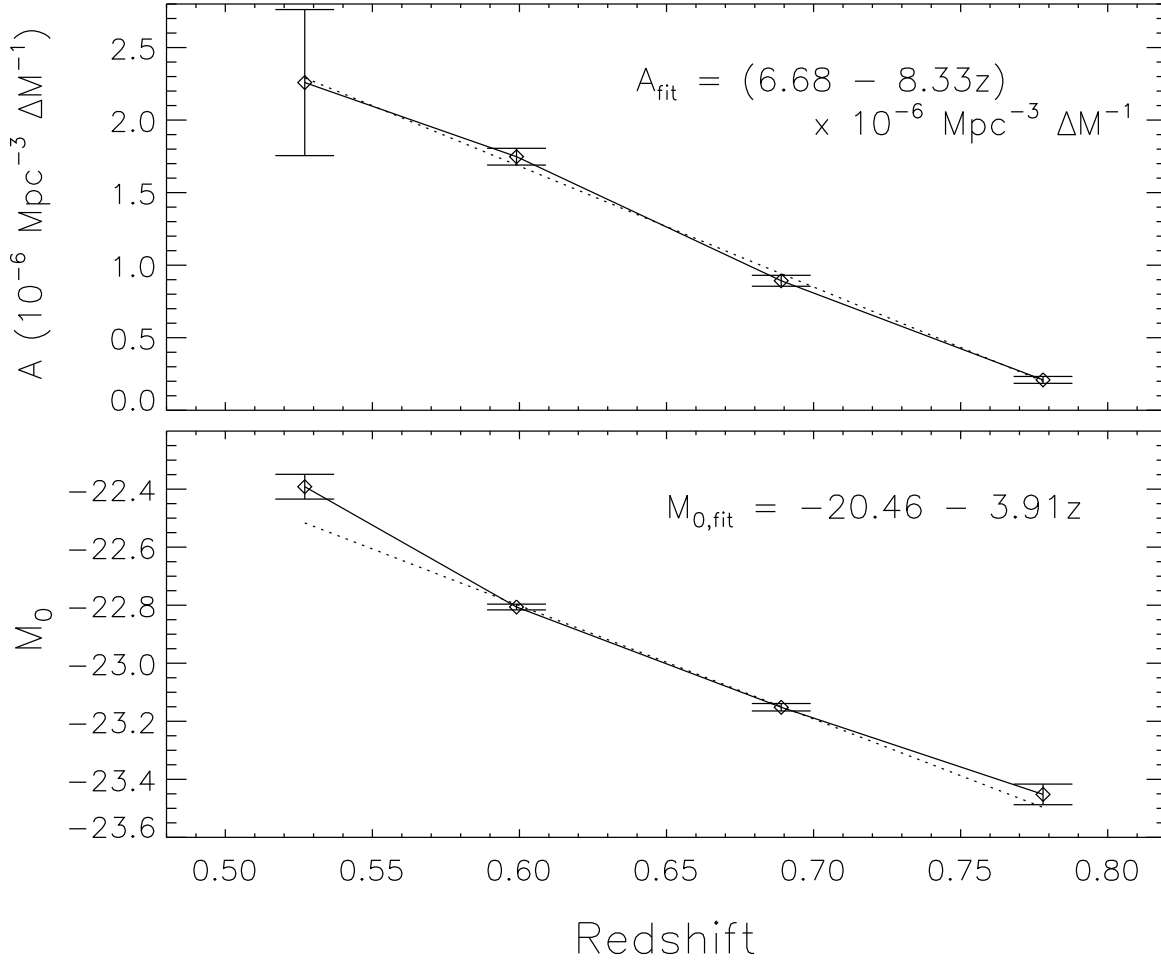


Figure 2.20 Best fit parameters of the luminosity functions of post-starburst galaxies from our BOSS CMASS sample for the different redshift bins shown in Figure 2.18. The fitting function is $\Phi(M) = A \exp\left(-\frac{(M-M_0)^2}{\sigma^2}\right)$, where the normalization A and the peak magnitude M_0 are free parameters and the width is fixed as constant at $\sigma = 0.4$. The dotted lines show the linear fit to these parameters. The redshift on the abscissa is the median redshift of objects in the bin. The empirical linear fits for these parameters are given in each panel.

This method is equivalent to asking the question “For a given luminosity function and our selection function, what is the probability distribution of luminosities for a galaxy of a given redshift and SED shape?”

For each galaxy in the sample, the contribution of this galaxy to the luminosity distribution bin is given by

$$P_{\text{one galaxy}}(M)\Delta M = \frac{\Phi(M)S(M)\Delta M}{\Sigma\Phi(M)S(M)\Delta M}, \quad (2.12)$$

where $\Phi(M)$ is the luminosity function. The selection function $S(M)$ is the fraction of the sample that could be observed at magnitude M given the color cuts. This is determined from the subsample at $M < M_{\text{crit}}$ where the sample is complete, which has the same color distribution as the rest of the sample, as shown in Figure 2.17. At fainter magnitudes, only a fraction $S(M)$ of this distribution is left due to the selection cut $M = -23.3 + 1.8C$. $S(M)$ can be written as

$$S(M) = \frac{\int_{C_{\text{cut}}(M)}^{\infty} \int_{-\infty}^{M_{\text{crit}}} D(M', C') dM' dC'}{\int_{-\infty}^{\infty} \int_{-\infty}^{M_{\text{crit}}} D(M', C') dM' dC'} \quad (2.13)$$

where $C_{\text{cut}}(M) = (M + 23.3)/1.8$.

The predicted luminosity distribution is then derived by summing equation 2.12 over the entire sample (or over redshift shells). The final profile of the predicted distribution integrates to exactly the same number of objects in the sample, since the normalization for each object is forced to be unity (as shown in equation 2.12).

This method in its simplest form assumes an unchanging population, which is in contrast with the strong redshift evolution we found in sections 5.3 and 5.4, and the fast drop in the global star formation rate of the universe since redshift unity. To address this issue, we need to take into account the redshift evolution of the luminosity function. For each galaxy, we evaluate the luminosity function $\Phi(M)$ at its observed redshift using the fit parameters to the redshift evolution of the luminosity function shown in Figure 2.20. This modified method is performed for the BOSS CMASS sample, both for the whole sample and in redshift bins. The predicted and observed luminosity distributions are shown in Figure 2.21. They agree very well, giving us an a

posteriori confirmation of the robustness of our luminosity function calculation. In its simplest form, in which both the luminosity function and luminosity distribution are calculated in a narrow redshift bin, this method is indeed a circular argument. This is because the observed distribution is corrected for selection effects in order to derive the luminosity function, which in turn has the selection effects added to get back at the observed distribution. However, in this case we take into account the fast redshift evolution of the luminosity function which effectively couples different redshift bins to each other, thus breaking the circularity and providing a non-trivial self-consistency test.

5.6 Comparison to Global Star Formation Rate

We now investigate whether the numbers of post-starburst galaxies in our sample could explain the decrease in the global star-formation rate since redshift $z \sim 1$. In other words, we test whether all the observed decrease in the star-formation rate is purely due to quenching of massive galaxies that are in our sample. In particular, we calculate the mass density in A-stars (ρ_A , in unit of M_\odot/Mpc^3) as a function of redshift using both approaches.

The first approach is to calculate the A-star mass density from the post-starburst galaxy luminosity functions, calculated from our sample in sections 5.3 and 5.4. This is done by performing the integral

$$\rho_A = \left(\frac{M}{L}\right)_A \left(\frac{A}{\text{Total}}\right) \int L \Phi(M) dM \quad (2.14)$$

This entire calculation is performed in our fiducial top-hat band in the wavelength range 4950-5100Å, which we have used in our calculation of the luminosity function. The integral represents the total stellar luminosity density in this wavelength band, with luminosity L consistently calculated from magnitude M in this band. This is then converted to A-star luminosity density with the global fraction $A/\text{Total} \sim 0.26$, which is calculated from fitting the templates to the coadded spectrum of the entire sample. Note that this A/Total value here is calculated in the [5000] band, and is not the same as the one used in the selection algorithm,

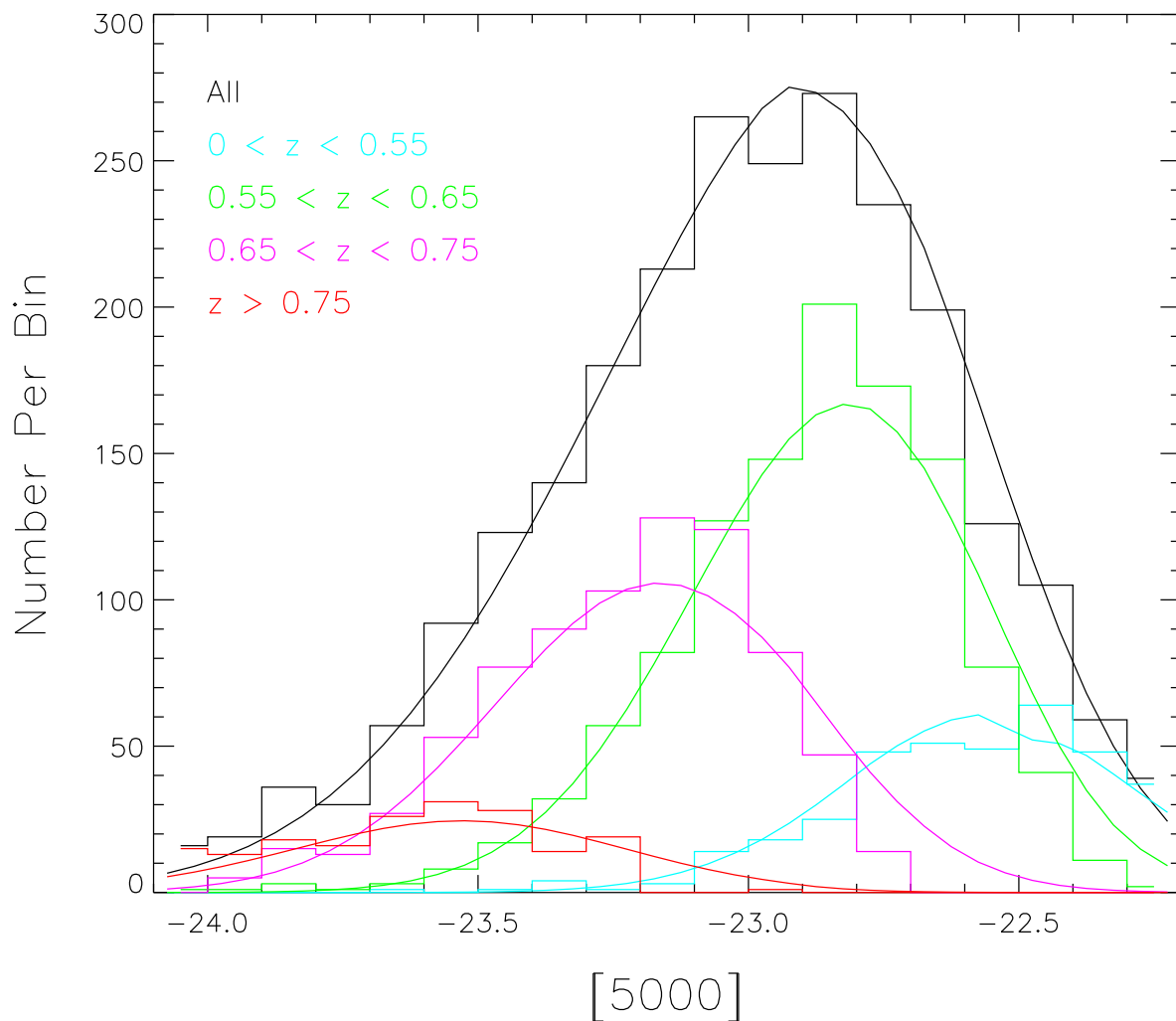


Figure 2.21 Comparison between the predicted and observed luminosity distribution in the [5000] band of the BOSS CMASS sample. The histograms show the observed luminosity distribution (simply numbers of galaxies in each magnitude bin). The solid lines are the predicted distribution calculated by the method described in the text. This calculation is performed for both the whole sample (black) and in redshift bins (colored). The agreement between the two is an a posteriori confirmation of the validity of our luminosity function determination.

which is in the [4200] band, which explains the low value. Finally it is converted to A-star mass density with the mass-to-light ratio of A-stars, which is calculated from the spectrophotometrically-calibrated spectrum of Vega by Bohlin & Gilliland (2004), assuming the distance to Vega of 7.68 pc.

The second approach is to calculate the A-star mass density expected from the declining global star-formation rate ρ_{SFR} . This is done by integrating the excess star-formation rate backward in time in the time interval that would result in the stellar population being identified as post-starburst by our definition at the epoch under consideration.

$$\rho_{\text{A}}(t) = \left(\frac{M_{\text{A}}}{M_{*}} \right) \int_{t-\tau_1}^{t-\tau_2} (\rho_{\text{SFR}}(t') - \rho_{\text{SFR}}(t - \tau_1)) dt' \quad (2.15)$$

The global star-formation density ρ_{SFR} (in unit of $M_{\odot}\text{yr}^{-1}\text{Mpc}^{-3}$) as a function of redshift is calculated using the fit formula in equation 15 from Madau & Dickinson (2014). The fraction $M_{\text{A}}/M_{*} \sim 0.07$ is the ratio of A-star mass to total mass formed. This is calculated from the Salpeter initial mass function (which is the same IMF assumed in the formula) assuming the lower and upper limits of A-star mass to be $1.6 - 2.9M_{\odot}$ respectively, while limiting the stellar masses to be between $0.08 - 100M_{\odot}$. The parameters τ_1 and τ_2 are the lower and upper age of the stellar population that would be identified as post-starburst by our selection algorithm. The lower limit τ_1 corresponds to the lifetime of a B3 star, which is the lowest mass star able to produce an HII region around it, leading to significant [OII] emission. The upper limit τ_2 is derived by comparing the single stellar population model by Maraston (2005) to our selection, requiring the A/Total ratio to be larger than 0.25. This age range is between 50 Myr and 0.8 Gyr, which is similar to the interval between the ages of B-stars and A-stars, as one would intuitively expect.

One inherent assumption in this estimate is that all galaxies that are still forming stars at the end of the time window were also forming stars at the beginning, and therefore are not in the post-starburst population. However, it can be the case that additional galaxies have quenched during that time period, joining the post-starburst population, while more star-formation happens in other galaxies to compensate for the overall star-formation rate. Thus this estimate is

a conservative lower limit, since it only shows the minimum amount of quenching demanded by the declining global star-formation rate.

We performed this exercise of estimating the A-star mass density by these two different methods in all redshift bins we used to calculate the luminosity function. This is shown in the upper panel of Figure 2.22. We define the parameter η , shown in the lower panel of the same figure, as the ratio between the mass density of A stars required by the global star-formation rate to that calculated from luminosity functions. This parameter, which has typical values of around 500, suggests that the massive post-starburst galaxies in our sample account for only a small component of the decline of star formation in the universe. The vast majority of this decline must be either in lower luminosity post-starburst galaxies, or in systems in which the star formation declines only gradually.

Indeed, this calculation contains a number of simplifying assumptions. For example, the A/Total ratio, while assumed to be global, can potentially be a function of luminosity. The IMF is simply assumed to be Salpeter. The mass-to-light ratio of A-stars are taken from Vega which is an A0 star and therefore is not representative of the whole A-star population. Each of these assumptions might easily give a factor of two error to the calculation. However, given that the discrepancy between the mass density of A-stars calculated from these two different methods is a few orders of magnitude, our qualitative conclusion is robust.

6 Discussion

6.1 Sample

From the publicly available data from the Sloan Digital Sky Survey, we have identified a large number of post-starburst galaxies based on their optical spectra. This sample is the largest sample of post-starburst galaxies thus far, and consists of 2359 galaxies from SDSS I/II and 3964 galaxies from SDSS III (BOSS) respectively. The highest-redshift objects are at redshift $z \sim 1$ and $z \sim 1.3$ for the two surveys respectively. In fact, for the BOSS sample, the size of the sample can be increased significantly: the sample used in this work is selected from the Ninth Data

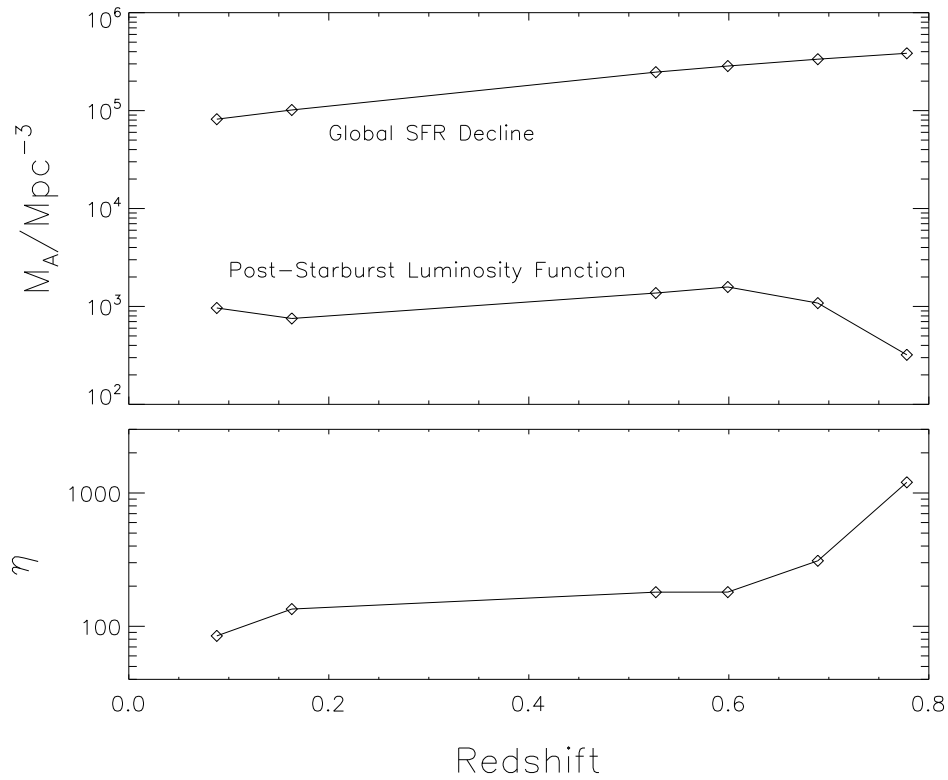


Figure 2.22 Top panel: The mass density in A-stars as a function of redshift (in units of M_\odot/Mpc^3) calculated in two ways. The bottom line is calculated from the luminosity functions of post-starburst galaxies in our sample. The top line is that expected from the declining global star-formation rate, as quantified by Madau & Dickinson (2014). Bottom panel: The ratio of the densities shown in the top panel. The typical value of around 500 indicates that the star formation quenching in massive post-starburst galaxies is a small component of the total decline of star formation in the universe.

Release (DR9; Ahn et al. (2012)), while the BOSS survey now contains twice as many spectra. This sample provides a valuable observational foundation for galaxy evolution studies.

The stellar populations of post-starburst galaxies are modeled with two main components: young, A-stars and an old underlying component. They are selected to not have any indication of ongoing star formation as measured by $[\text{OII}]\lambda 3727$ nebular line emission. So these objects had a large amount of star formation between 20 million and 0.8 billion years previously that is almost entirely quenched by the epoch when they are observed.

Their spectra also show a diverse range of features. Weak MgII absorption is seen in a large number of objects. This feature is related to the intragalactic gas, and its velocity relative to the systemic redshift indicates inflow or outflow. A small number of objects show either blue continuum or broad MgII in emission, both of which are related to AGN activity which is thought to be one possible feedback mechanism to cause the quenching.

6.2 Evolution of the Luminosity Function

The luminosity functions calculated from the SDSS I/II and BOSS samples in a number of redshift bins evolve rapidly over the redshift baseline from $z \sim 0.8$ to 0.1. The sense of this evolution is consistent with downsizing, where the typical stellar mass of objects that are currently quenching their star formation decreases with cosmic time (e.g., Bundy et al. (2006)).

This dramatic evolution is expected in light of the finding that the global star formation rate of the universe drops by an order of magnitude since redshift $z \sim 1$ (Madau & Dickinson, 2014). The decrease in global star formation rate would require a number of star-forming galaxies to be quenched. These galaxies would subsequently enter the post-starburst phase, in the redshift range we probe with this survey. Under the assumption that all galaxies pass through a post-starburst phase after quenching, and that our sample selection is sufficiently complete, we would expect that the evolution in the luminosity function of post-starburst galaxies should broadly reflect the evolution in global star formation rate.

To check this idea, we calculated the mass density in A stars indicated by the measured luminosity functions, and compared this to what is expected from the declining global

star-formation rate. We found that the mass density of A stars in our post-starburst galaxies is smaller than that expected by a factor of ~ 500 , suggesting that most star-forming galaxies at high redshift do *not* go through a luminous post-starburst phase, and post-starburst galaxies are indeed a rare occurrence.

In light of this result, there are a few ways in which the star formation rate could decrease without entering the post-starburst phase. The first is that most of the star-formation quenching might happen in low-mass galaxies or satellites that are not luminous enough to be selected as part of the survey. The $1/V_{\max}$ formulation we performed in redshift bins does not correct for this because the luminosity functions are evolving with redshift, and thus faint galaxies that are seen locally can not be used to imply the corresponding population at higher redshift. Indeed, even if there exists a large population of unseen low-luminosity galaxies at high redshift, it would not contribute much to the total luminosity and inferred mass. For example, if the faint end of the luminosity function at $0.65 < z < 0.75$ mirrored of the $z < 0.12$ bin, it would have increased the total luminosity in that bin by less than a factor of 2.

The second way this could happen is for the star formation to be quenched gradually in the majority of star-forming galaxies, and perhaps staying at a modest rate thereafter (e.g. Cortese & Hughes 2009; Salim et al. 2012; Fang et al. 2012, 2013; Schawinski et al. 2014). Such galaxies will never show a strong A-star component in their spectra, and will not be identified as a post-starburst galaxy. We believe that this scenario is the main channel by which the star-formation rate in the universe has decreased, given that reasonably massive galaxies, like our Milky Way, that retain modest levels of star formation are common.

Another complication in this aspect is that a fraction of post-starburst galaxies might not represent a key evolutionary stage of the galaxy, but only a random, stochastic phase of a small-scale starburst which is not significant compared to the total stellar mass of the galaxy. Depending on the exact details of the selection criteria, these objects might pass through the selection and enter the sample. This issue can be answered, again, by understanding the mapping between the fundamental properties of the stellar population to the observable spectral features, which can be done with stellar population synthesis models.

6.3 Mechanisms Responsible for Quenching

Another key aspect is the physical mechanism for quenching the star formation on a short timescale. There are two main scenarios by which this can happen. The first involves cluster-related mechanisms such as ram-pressure stripping, in which a star-forming galaxy falls into a galaxy cluster, and interacts with the intracluster medium. The second is the merger-related scenario, where a merger between two gas-rich galaxies induces a large starburst which is subsequently quenched either due to feedback or gas exhaustion. These scenarios can be distinguished in a number of different ways, some with data available in this sample, some requiring more complementary information.

One possible way to approach this would be to use stellar population model fits to the individual galaxy spectra to reconstruct a crude star-formation history of each galaxy. If the recent star formation history is consistent with a large starburst that is quenched quickly, then it would be more consistent with the merger scenario where the large scale starburst is induced all at once, possibly at the center of the galaxy. In contrast, if the star-formation history is closer to being constant, before being quenched relatively suddenly, then it would be closer to the cluster interaction scenario. In this case, the term post-starburst is certainly misleading, because there is no burst, but it can have strong enough A-star feature to be classified under this group if the star formation is quenched suddenly enough (Quintero et al., 2004). In practice, distinguishing these two scenarios in stellar populations is a challenging task and might only be possible for extreme cases even for a high signal-to-noise ratio spectra.

Another clue contained within the spectra is the presence of AGN, which certainly also can play an important role in the evolution of the galaxy, and might be closely related to how the star formation is quenched. Simulations (Hopkins et al., 2006, 2008; Sijacki et al., 2007) invoke the quenching from AGN feedback, providing the energy needed to stop overproduction of stars. However, there is evidence (Wild et al., 2010; Shin et al., 2011; Yesuf et al., 2014) that AGN activity tends to peak after the starburst, and therefore might not be the cause of star formation quenching. Quantifying the number of post-starburst galaxies with spectroscopic AGN signatures might yield an understanding of the influence central AGNs have on this population. In our

sample there are ~ 100 objects that show sign of AGN activity such as blue continuum or, more importantly, broad line emission. However, this number might suffer from severe selection bias, since AGN activity can give rise to [OII] $\lambda 3727$ emission, leading to exclusion of objects from our sample. In addition to the optical signature of the AGN, if complementary data in other wavelength ranges (such as X-ray or radio) is available then one might also have different ways to detect and quantify AGN properties and understand this relation (eg. Shin et al. (2011)).

Moreover, this sample can be augmented by a number of external datasets. Firstly, deep imaging data can be very useful to quantify the environment of the post-starburst galaxies, i.e., whether they lie in galaxy clusters or the field. The requirement is that these imaging data have to be deep enough to see a typical L_* galaxy at redshifts up to unity. The SDSS photometric data are not deep enough to do this, but various current and upcoming weak-lensing surveys such as the Canadian-France-Hawaii Telescope Legacy Survey (CFHTLS; Heymans et al. (2012)), the Dark Energy Survey (DES; The Dark Energy Survey Collaboration (2005)), Hyper-Suprime Cam (HSC; Miyazaki et al. (2012)) and the Large Synoptic Survey Telescope (LSST; Ivezić et al. (2008)) would be sufficient for this task.

High resolution HST imaging data would also be useful in studying the morphology of these objects at high redshift to probe the effect of close interactions and mergers, possibly by comparing to a control sample of normal galaxies with similar mass and redshift. If a significant fraction of post-starburst galaxies, especially ones in the field, show signs of disturbed morphology or close, merging neighbors, it would lend support to the merger scenario. It would also be interesting if one finds field post-starburst galaxies with smooth morphology, since that would need some other explanation. There are a number of works studying morphologies at low redshift (e.g., Yang et al. (2008) for post-starburst galaxies, Cales et al. (2011) for post-starburst quasars). However, since the post-starburst galaxy population at high redshift is significantly different from that at low redshift, as seen in the evolution of the luminosity function, independent studies at high redshift must be done to fully understand the properties and mechanisms at work in the high-redshift population.

Indeed, the single most important piece of information that would allow us to explore different ways that galaxies evolve is the stellar mass. This is because the observed color and luminosity change in complex ways due to stellar evolution, while the stellar mass reflects fundamental changes in galaxy properties like mergers, infall or star formation. However, stellar population modeling to determine stellar mass is subject to serious systematic errors, including uncertainties in the IMF, poorly understood late stages of stellar evolution, and degeneracies between fit parameters.

6.4 Improvement to Selection Method

In this work, we have developed a robust method to select post-starburst galaxies from optical spectra. This method relies minimally on prior knowledge of the redshift of the object, making it suitable to apply to large amounts of spectroscopic data even in the presence of large redshift errors in the standard pipeline. This algorithm selects a relatively small number of candidates from the large dataset for visual inspection to confirm the correctness of the identification. While the false negative rate is very small based on a small test sample of known post-starburst galaxies, the false positive rate to be removed by visual inspection is between 100% and 300%. At this point, the amount of visual inspection required is still manageable, but more optimized algorithm with lower false positive rate will be critical when the next generation of surveys generate significantly larger samples. Examples of such surveys are the fourth phase of the Sloan Digital Sky Survey (SDSS IV), The Dark Energy Spectroscopic Instrument (DESI; Levi et al. (2013)) and the Prime Focus Spectrograph (PFS; Takada et al. (2014)). For SDSS and BOSS data in particular, it was found in retrospect that the redshift determination by the spectroscopic pipeline is very robust, with less than 5% incorrect redshifts even for this rare class of objects. Therefore, selecting the post-starburst galaxies from SDSS and BOSS assuming the pipeline redshifts to be reliable would have simplified the process and reduced the number of false positives significantly.

In light of this, there are some improvements to incorporate the future work selecting post-starburst galaxies from large spectroscopic surveys. One such dataset in the near future

would be the entire BOSS survey (SDSS DR12). This phase of SDSS contains twice as many spectra than what we used in this paper, and is now public (Alam et al., 2015).

The first improvement might be to do the selection based on the stellar population properties, rather than empirical cuts on parameters such as A/Total or equivalent widths. Ideally, this approach is more preferable since it leads to selection based on physically meaningful properties of the galaxy population such as stellar population age and metallicity. For example, one might define post-starburst galaxies to be populations that are older than 300Myr but younger than 1Gyr. Yesuf et al. (2014) fit stellar population models using multi-wavelength data while taking AGN and dust obscuration into account.

Selection of these objects from the next generation of multi-band photometric surveys is another possibility. Doing so requires distinguishing between the 3600\AA Balmer break and the 4000\AA break at slightly different redshifts. One can potentially resolve this ambiguity using multi-wavelength information, for example in NUV and NIR, since the old population would have almost no flux in NUV but large flux in NIR, and conversely for the young population. Wild et al. (2014) studied galaxy SEDs in optical and NIR, and found that post-starburst galaxies have unique, identifiable colors. However, the presence of dust and AGN would make this task challenging.

7 Conclusion

The post-starburst phase is a rare phase in galaxy evolution, in which a small number of star-forming galaxies are on their way to becoming passive elliptical galaxies. Therefore, understanding this class of galaxies could yield clues about how galaxies evolve and the mechanisms that drive evolution, at least for massive galaxies. Currently, there are many open questions in this topic, ranging from phenomenological aspects such as the luminosity function and its evolution with redshift, to the physical mechanisms that cause star formation to stop and subsequently turn a starforming galaxy into a post-starburst galaxy. One key limitation faced by many previous works was the lack of a large, statistical sample with uniform selection over a broad range of redshift.

In this paper, we have systematically selected a sample of post-starburst galaxies from the SDSS DR9 spectroscopic dataset. The method we developed is based on template fitting, with cuts on equivalent widths applied to various relevant spectral lines. The selection algorithm is tested and verified against a smaller sample of post-starburst galaxies known prior to the study. All objects in the final sample are visually inspected to remove false positives.

We apply this selection scheme to the entire SDSS DR7 spectroscopic database, and also to the BOSS spectroscopic dataset presented in DR9. This yields 2330 galaxies from the SDSS DR7 dataset, and 3964 galaxies from the BOSS dataset. This is the largest sample of post-starburst galaxies currently available in the literature. The full list of these objects is available with this paper. The redshifts of these galaxies range from local galaxies up to $z \sim 1.3$, with a median redshift of ~ 0.16 and ~ 0.61 for the SDSS DR7 and BOSS subsamples respectively, with little overlap between them. Various interesting spectral features are seen, such as MgII absorption in a large number of galaxies, and broad MgII emission and blue continuum in about 100 objects. They are the so-called post-starburst quasars.

A large fraction of SDSS DR7 sample is selected by the Main Galaxy Sample, while the dominant spectroscopic selection algorithm for BOSS sample is CMASS. These two subsamples have uniform magnitude and color selection criteria, allowing us to calculate luminosity functions in a number of redshift bins.

We quantify and correct for various selection biases in the luminosity function calculation. The first bias is the different cosmological volume over which each object can be selected from the spectroscopic sample of the survey. This is corrected by the standard $1/V_{\max}$ method, where V_{\max} is calculated from the individual spectrum and the details of the selection criteria for each subsample. The second effect is due to the color selection algorithm used in the CMASS sample, which is biased against faint blue objects, even though we expect post-starburst galaxies to also exist in that region of color space. This is corrected by extrapolation from the complete part of the color distribution, assuming that the underlying distribution is separable in color and magnitude, an assumption shown to be consistent with the data. Moreover, after all the corrections are performed, we compare the observed distribution of objects in luminosity to the

expected one given the luminosity function. The observed and expected distributions are consistent, suggesting that our method to calculate the luminosity function is robust.

We see strong redshift evolution of the resulting luminosity function of our post-starburst galaxy sample. The sense of this evolution is that the number density at fixed luminosity of post-starburst galaxies is considerably higher at high redshift. In other words, we see the “downsizing” trend in the luminosity function evolution that has been seen in other galaxy populations. At fixed redshift, the less luminous objects are more abundant than luminous objects. This trend, qualitatively, is in line with the expectation from the fact that the global star formation rate of the universe has dropped by about an order of magnitude since redshift $z \sim 1$.

We performed a quantitative comparison between the mass density of the post-starburst A stars population from our sample (by integrating over the luminosity function), to that expected from the declining global star-formation rate. We found that only a small fraction, approximately 0.2%, of the minimum star-formation quenching required by the declining global star-formation rate, can be explained by the amount found in post-starburst galaxies. This makes post-starburst galaxies a rare phenomenon. It suggests that most star-formation quenching has to happen in ways that escape our post-starburst galaxy selection method. This can be either by quenching gradually enough to never show strong post-starburst spectral signatures, or by quenching in low-mass galaxies or satellites that are too faint to be selected into the SDSS survey at high redshift.

Acknowledgement

We thank Kevin Bundy, Renyue Cen, Jenny Greene, James Gunn, Robert Lupton, and Christy Tremonti for useful discussions, insights and comments during the entire duration of this project. We also thank the anonymous referee for exceptionally thorough feedback, which has improved the paper significantly.

Funding for SDSS-III has been provided by the Alfred P. Sloan Foundation, the Participating Institutions, the National Science Foundation, and the U.S. Department of Energy Office of Science. The SDSS-III web site is <http://www.sdss3.org/>.

SDSS-III is managed by the Astrophysical Research Consortium for the Participating Institutions of the SDSS-III Collaboration including the University of Arizona, the Brazilian Participation Group, Brookhaven National Laboratory, Carnegie Mellon University, University of Florida, the French Participation Group, the German Participation Group, Harvard University, the Instituto de Astrofísica de Canarias, the Michigan State/Notre Dame/JINA Participation Group, Johns Hopkins University, Lawrence Berkeley National Laboratory, Max Planck Institute for Astrophysics, Max Planck Institute for Extraterrestrial Physics, New Mexico State University, New York University, Ohio State University, Pennsylvania State University, University of Portsmouth, Princeton University, the Spanish Participation Group, University of Tokyo, University of Utah, Vanderbilt University, University of Virginia, University of Washington, and Yale University.

This work is partially based on observations obtained with the Apache Point Observatory 3.5-meter telescope, which is owned and operated by the Astrophysical Research Consortium.

Bibliography

Adelman-McCarthy, J. K., Agüeros, M. A., Allam, S. S., Allende Prieto, C., Anderson, K. S. J., Anderson, S. F., Annis, J., Bahcall, N. A., Bailer-Jones, C. A. L., Baldry, I. K., Barentine, J. C., Bassett, B. A., Becker, A. C., Beers, T. C., Bell, E. F., Berlind, A. A., Bernardi, M., Blanton, M. R., Bochanski, J. J., Boroski, W. N., Brinchmann, J., Brinkmann, J., Brunner, R. J., Budavári, T., Carliles, S., Carr, M. A., Castander, F. J., Cinabro, D., Cool, R. J., Covey, K. R., Csabai, I., Cunha, C. E., Davenport, J. R. A., Dilday, B., Doi, M., Eisenstein, D. J., Evans, M. L., Fan, X., Finkbeiner, D. P., Friedman, S. D., Frieman, J. A., Fukugita, M., Gänsicke, B. T., Gates, E., Gillespie, B., Glazebrook, K., Gray, J., Grebel, E. K., Gunn, J. E., Gurbani, V. K., Hall, P. B., Harding, P., Harvanek, M., Hawley, S. L., Hayes, J., Heckman, T. M., Hendry, J. S., Hindsley, R. B., Hirata, C. M., Hogan, C. J., Hogg, D. W., Hyde, J. B., Ichikawa, S.-i., Ivezić, Ž., Jester, S., Johnson, J. A., Jorgensen, A. M., Jurić, M., Kent, S. M., Kessler, R., Kleinman, S. J., Knapp, G. R., Kron, R. G., Krzesinski, J., Kuropatkin, N., Lamb, D. Q., Lampeitl, H., Lebedeva, S., Lee, Y. S., Leger, R. F., Lépine, S., Lima, M., Lin, H., Long,

- D. C., Loomis, C. P., Loveday, J., Lupton, R. H., Malanushenko, O., Malanushenko, V., Mandelbaum, R., Margon, B., Marriner, J. P., Martínez-Delgado, D., Matsubara, T., McGehee, P. M., McKay, T. A., Meiksin, A., Morrison, H. L., Munn, J. A., Nakajima, R., Neilsen, Jr., E. H., Newberg, H. J., Nichol, R. C., Nicinski, T., Nieto-Santisteban, M., Nitta, A., Okamura, S., Owen, R., Oyaizu, H., Padmanabhan, N., Pan, K., Park, C., Peoples, Jr., J., Pier, J. R., Pope, A. C., Purger, N., Raddick, M. J., Re Fiorentin, P., Richards, G. T., Richmond, M. W., Riess, A. G., Rix, H.-W., Rockosi, C. M., Sako, M., Schlegel, D. J., Schneider, D. P., Schreiber, M. R., Schwobe, A. D., Seljak, U., Sesar, B., Sheldon, E., Shimasaku, K., Sivarani, T., Smith, J. A., Snedden, S. A., Steinmetz, M., Strauss, M. A., SubbaRao, M., Suto, Y., Szalay, A. S., Szapudi, I., Szkody, P., Tegmark, M., Thakar, A. R., Tremonti, C. A., Tucker, D. L., Uomoto, A., Vanden Berk, D. E., Vandenberg, J., Vidrih, S., Vogeley, M. S., Voges, W., Vogt, N. P., Wadadekar, Y., Weinberg, D. H., West, A. A., White, S. D. M., Wilhite, B. C., Yanny, B., Yocum, D. R., York, D. G., Zehavi, I., & Zucker, D. B. 2008, *ApJS*, 175, 297
- Adelman-McCarthy, J. K., Agüeros, M. A., Allam, S. S., Anderson, K. S. J., Anderson, S. F., Annis, J., Bahcall, N. A., Bailer-Jones, C. A. L., Baldry, I. K., Barentine, J. C., Beers, T. C., Belokurov, V., Berlind, A., Bernardi, M., Blanton, M. R., Bochanski, J. J., Boroski, W. N., Bramich, D. M., Brewington, H. J., Brinchmann, J., Brinkmann, J., Brunner, R. J., Budavári, T., Carey, L. N., Carliles, S., Carr, M. A., Castander, F. J., Connolly, A. J., Cool, R. J., Cunha, C. E., Csabai, I., Dalcanton, J. J., Doi, M., Eisenstein, D. J., Evans, M. L., Evans, N. W., Fan, X., Finkbeiner, D. P., Friedman, S. D., Frieman, J. A., Fukugita, M., Gillespie, B., Gilmore, G., Glazebrook, K., Gray, J., Grebel, E. K., Gunn, J. E., de Haas, E., Hall, P. B., Harvanek, M., Hawley, S. L., Hayes, J., Heckman, T. M., Hendry, J. S., Hennessy, G. S., Hindsley, R. B., Hirata, C. M., Hogan, C. J., Hogg, D. W., Holtzman, J. A., Ichikawa, S.-i., Ichikawa, T., Ivezić, Ž., Jester, S., Johnston, D. E., Jorgensen, A. M., Jurić, M., Kauffmann, G., Kent, S. M., Kleinman, S. J., Knapp, G. R., Kniazev, A. Y., Kron, R. G., Krzesinski, J., Kuropatkin, N., Lamb, D. Q., Lampeitl, H., Lee, B. C., Leger, R. F., Lima, M., Lin, H., Long, D. C., Loveday, J., Lupton, R. H., Mandelbaum, R., Margon, B., Martínez-Delgado, D., Matsubara, T., McGehee, P. M., McKay, T. A., Meiksin, A., Munn, J. A., Nakajima, R., Nash,

- T., Neilsen, Jr., E. H., Newberg, H. J., Nichol, R. C., Nieto-Santisteban, M., Nitta, A., Oyaizu, H., Okamura, S., Ostriker, J. P., Padmanabhan, N., Park, C., Peoples, Jr., J., Pier, J. R., Pope, A. C., Pourbaix, D., Quinn, T. R., Raddick, M. J., Re Fiorentin, P., Richards, G. T., Richmond, M. W., Rix, H.-W., Rockosi, C. M., Schlegel, D. J., Schneider, D. P., Scranton, R., Seljak, U., Sheldon, E., Shimasaku, K., Silvestri, N. M., Smith, J. A., Smolčić, V., Snedden, S. A., Stebbins, A., Stoughton, C., Strauss, M. A., SubbaRao, M., Suto, Y., Szalay, A. S., Szapudi, I., Szkody, P., Tegmark, M., Thakar, A. R., Tremonti, C. A., Tucker, D. L., Uomoto, A., Vanden Berk, D. E., Vandenberg, J., Vidrih, S., Vogeley, M. S., Voges, W., Vogt, N. P., Weinberg, D. H., West, A. A., White, S. D. M., Wilhite, B., Yanny, B., Yocum, D. R., York, D. G., Zehavi, I., Zibetti, S., & Zucker, D. B. 2007, *ApJS*, 172, 634
- Ahn, C. P., Alexandroff, R., Allende Prieto, C., Anderson, S. F., Anderton, T., Andrews, B. H., Aubourg, É., Bailey, S., Balbinot, E., Barnes, R., & et al. 2012, *ApJS*, 203, 21
- Alam, S., Albareti, F. D., Allende Prieto, C., Anders, F., Anderson, S. F., Anderton, T., Andrews, B. H., Armengaud, E., Aubourg, É., Bailey, S., & et al. 2015, *ApJS*, 219, 12
- Anderson, L., Aubourg, E., Bailey, S., Bizyaev, D., Blanton, M., Bolton, A. S., Brinkmann, J., Brownstein, J. R., Burden, A., Cuesta, A. J., da Costa, L. A. N., Dawson, K. S., de Putter, R., Eisenstein, D. J., Gunn, J. E., Guo, H., Hamilton, J.-C., Harding, P., Ho, S., Honscheid, K., Kazin, E., Kirkby, D., Kneib, J.-P., Labatie, A., Loomis, C., Lupton, R. H., Malanushenko, E., Malanushenko, V., Mandelbaum, R., Manera, M., Maraston, C., McBride, C. K., Mehta, K. T., Mena, O., Montesano, F., Muna, D., Nichol, R. C., Nuza, S. E., Olmstead, M. D., Oravetz, D., Padmanabhan, N., Palanque-Delabrouille, N., Pan, K., Parejko, J., Pâris, I., Percival, W. J., Petitjean, P., Prada, F., Reid, B., Roe, N. A., Ross, A. J., Ross, N. P., Samushia, L., Sánchez, A. G., Schlegel, D. J., Schneider, D. P., Scóccola, C. G., Seo, H.-J., Sheldon, E. S., Simmons, A., Skibba, R. A., Strauss, M. A., Swanson, M. E. C., Thomas, D., Tinker, J. L., Tojeiro, R., Magaña, M. V., Verde, L., Wagner, C., Wake, D. A., Weaver, B. A., Weinberg, D. H., White, M., Xu, X., Yèche, C., Zehavi, I., & Zhao, G.-B. 2012, *MNRAS*, 427, 3435
- Balogh, M. L., Miller, C., Nichol, R., Zabludoff, A., & Goto, T. 2005, *MNRAS*, 360, 587

- Balogh, M. L., Navarro, J. F., & Morris, S. L. 2000, *ApJ*, 540, 113
- Bekki, K., Couch, W. J., Shioya, Y., & Vazdekis, A. 2005, *MNRAS*, 359, 949
- Bekki, K., Owers, M. S., & Couch, W. J. 2010, *ApJ*, 718, L27
- Bekki, K., Shioya, Y., & Couch, W. J. 2001, *ApJ*, 547, L17
- Belloni, P. 1997, in *Galaxy Scaling Relations: Origins, Evolution and Applications*, ed. L. N. da Costa & A. Renzini, 319
- Blake, C., Pracy, M. B., Couch, W. J., Bekki, K., Lewis, I., Glazebrook, K., Baldry, I. K., Baugh, C. M., Bland-Hawthorn, J., Bridges, T., Cannon, R., Cole, S., Colless, M., Collins, C., Dalton, G., De Propris, R., Driver, S. P., Efstathiou, G., Ellis, R. S., Frenk, C. S., Jackson, C., Lahav, O., Lumsden, S., Maddox, S., Madgwick, D., Norberg, P., Peacock, J. A., Peterson, B. A., Sutherland, W., & Taylor, K. 2004, *MNRAS*, 355, 713
- Blanton, M. R., Dalcanton, J., Eisenstein, D., Loveday, J., Strauss, M. A., SubbaRao, M., Weinberg, D. H., Anderson, Jr., J. E., Annis, J., Bahcall, N. A., Bernardi, M., Brinkmann, J., Brunner, R. J., Burles, S., Carey, L., Castander, F. J., Connolly, A. J., Csabai, I., Doi, M., Finkbeiner, D., Friedman, S., Frieman, J. A., Fukugita, M., Gunn, J. E., Hennessy, G. S., Hindsley, R. B., Hogg, D. W., Ichikawa, T., Ivezić, Ž., Kent, S., Knapp, G. R., Lamb, D. Q., Leger, R. F., Long, D. C., Lupton, R. H., McKay, T. A., Meiksin, A., Merelli, A., Munn, J. A., Narayanan, V., Newcomb, M., Nichol, R. C., Okamura, S., Owen, R., Pier, J. R., Pope, A., Postman, M., Quinn, T., Rockosi, C. M., Schlegel, D. J., Schneider, D. P., Shimasaku, K., Siegmund, W. A., Smee, S., Snir, Y., Stoughton, C., Stubbs, C., Szalay, A. S., Szokoly, G. P., Thakar, A. R., Tremonti, C., Tucker, D. L., Uomoto, A., Vanden Berk, D., Vogeley, M. S., Waddell, P., Yanny, B., Yasuda, N., & York, D. G. 2001, *AJ*, 121, 2358
- Blanton, M. R., Lin, H., Lupton, R. H., Maley, F. M., Young, N., Zehavi, I., & Loveday, J. 2003, *AJ*, 125, 2276
- Bohlin, R. C. & Gilliland, R. L. 2004, *AJ*, 127, 3508

- Bolton, A. S., Schlegel, D. J., Aubourg, É., Bailey, S., Bhardwaj, V., Brownstein, J. R., Burles, S., Chen, Y.-M., Dawson, K., Eisenstein, D. J., Gunn, J. E., Knapp, G. R., Loomis, C. P., Lupton, R. H., Maraston, C., Muna, D., Myers, A. D., Olmstead, M. D., Padmanabhan, N., Pâris, I., Percival, W. J., Petitjean, P., Rockosi, C. M., Ross, N. P., Schneider, D. P., Shu, Y., Strauss, M. A., Thomas, D., Tremonti, C. A., Wake, D. A., Weaver, B. A., & Wood-Vasey, W. M. 2012, *AJ*, 144, 144
- Brotherton, M., Diamond-Stanic, A., vanden Berk, D., Burton, R., & Croom, S. 2004, in *Astronomical Society of the Pacific Conference Series*, Vol. 311, *AGN Physics with the Sloan Digital Sky Survey*, ed. G. T. Richards & P. B. Hall, 285
- Brotherton, M. S., van Breugel, W., Stanford, S. A., Smith, R. J., Boyle, B. J., Miller, L., Shanks, T., Croom, S. M., & Filippenko, A. V. 1999, *ApJ*, 520, L87
- Bundy, K., Ellis, R. S., Conselice, C. J., Taylor, J. E., Cooper, M. C., Willmer, C. N. A., Weiner, B. J., Coil, A. L., Noeske, K. G., & Eisenhardt, P. R. M. 2006, *ApJ*, 651, 120
- Caldwell, N., Rose, J. A., & Dendy, K. 1999, *AJ*, 117, 140
- Caldwell, N., Rose, J. A., Franx, M., & Leonardi, A. J. 1996, *AJ*, 111, 78
- Cales, S. L., Brotherton, M. S., Shang, Z., Bennert, V. N., Canalizo, G., Stoll, R., Ganguly, R., Vanden Berk, D., Paul, C., & Diamond-Stanic, A. 2011, *ApJ*, 741, 106
- Chang, T.-C., van Gorkom, J. H., Zabludoff, A. I., Zaritsky, D., & Mihos, J. C. 2001, *AJ*, 121, 1965
- Choi, Y., Goto, T., & Yoon, S.-J. 2009, *MNRAS*, 395, 637
- Cortese, L. & Hughes, T. M. 2009, *MNRAS*, 400, 1225
- Cushing, M. C., Vacca, W. D., & Rayner, J. T. 2004, *PASP*, 116, 362
- Dawson, K. S., Schlegel, D. J., Ahn, C. P., Anderson, S. F., Aubourg, É., Bailey, S., Barkhouser, R. H., Bautista, J. E., Beifiori, A., Berlind, A. A., Bhardwaj, V., Bizyaev, D., Blake, C. H.,

- Blanton, M. R., Blomqvist, M., Bolton, A. S., Borde, A., Bovy, J., Brandt, W. N., Brewington, H., Brinkmann, J., Brown, P. J., Brownstein, J. R., Bundy, K., Busca, N. G., Carithers, W., Carnero, A. R., Carr, M. A., Chen, Y., Comparat, J., Connolly, N., Cope, F., Croft, R. A. C., Cuesta, A. J., da Costa, L. N., Davenport, J. R. A., Delubac, T., de Putter, R., Dhital, S., Ealet, A., Ebelke, G. L., Eisenstein, D. J., Escoffier, S., Fan, X., Filiz Ak, N., Finley, H., Font-Ribera, A., Génova-Santos, R., Gunn, J. E., Guo, H., Haggard, D., Hall, P. B., Hamilton, J.-C., Harris, B., Harris, D. W., Ho, S., Hogg, D. W., Holder, D., Honscheid, K., Huehnerhoff, J., Jordan, B., Jordan, W. P., Kauffmann, G., Kazin, E. A., Kirkby, D., Klaene, M. A., Kneib, J.-P., Le Goff, J.-M., Lee, K.-G., Long, D. C., Loomis, C. P., Lundgren, B., Lupton, R. H., Maia, M. A. G., Makler, M., Malanushenko, E., Malanushenko, V., Mandelbaum, R., Manera, M., Maraston, C., Margala, D., Masters, K. L., McBride, C. K., McDonald, P., McGreer, I. D., McMahon, R. G., Mena, O., Miralda-Escudé, J., Montero-Dorta, A. D., Montesano, F., Muna, D., Myers, A. D., Naugle, T., Nichol, R. C., Noterdaeme, P., Nuza, S. E., Olmstead, M. D., Oravetz, A., Oravetz, D. J., Owen, R., Padmanabhan, N., Palanque-Delabrouille, N., Pan, K., Parejko, J. K., Pâris, I., Percival, W. J., Pérez-Fournon, I., Pérez-Ràfols, I., Petitjean, P., Pfaffenberger, R., Pforr, J., Pieri, M. M., Prada, F., Price-Whelan, A. M., Raddick, M. J., Rebolo, R., Rich, J., Richards, G. T., Rockosi, C. M., Roe, N. A., Ross, A. J., Ross, N. P., Rossi, G., Rubiño-Martin, J. A., Samushia, L., Sánchez, A. G., Sayres, C., Schmidt, S. J., Schneider, D. P., Scóccola, C. G., Seo, H.-J., Sheldon, A., Sheldon, E., Shen, Y., Shu, Y., Slosar, A., Smee, S. A., Snedden, S. A., Stauffer, F., Steele, O., Strauss, M. A., Streblyanska, A., Suzuki, N., Swanson, M. E. C., Tal, T., Tanaka, M., Thomas, D., Tinker, J. L., Tojeiro, R., Tremonti, C. A., Vargas Magaña, M., Verde, L., Viel, M., Wake, D. A., Watson, M., Weaver, B. A., Weinberg, D. H., Weiner, B. J., West, A. A., White, M., Wood-Vasey, W. M., Yèche, C., Zehavi, I., Zhao, G.-B., & Zheng, Z. 2013, *AJ*, 145, 10
- Diamond-Stanic, A. M., Moustakas, J., Tremonti, C. A., Coil, A. L., Hickox, R. C., Robaina, A. R., Rudnick, G. H., & Sell, P. H. 2012, *ApJ*, 755, L26
- Dressler, A. & Gunn, J. E. 1983, *ApJ*, 270, 7

- Eisenstein, D. J., Annis, J., Gunn, J. E., Szalay, A. S., Connolly, A. J., Nichol, R. C., Bahcall, N. A., Bernardi, M., Burles, S., Castander, F. J., Fukugita, M., Hogg, D. W., Ivezić, Ž., Knapp, G. R., Lupton, R. H., Narayanan, V., Postman, M., Reichart, D. E., Richmond, M., Schneider, D. P., Schlegel, D. J., Strauss, M. A., SubbaRao, M., Tucker, D. L., Vanden Berk, D., Vogeley, M. S., Weinberg, D. H., & Yanny, B. 2001, *AJ*, 122, 2267
- Eisenstein, D. J., Hogg, D. W., Fukugita, M., Nakamura, O., Bernardi, M., Finkbeiner, D. P., Schlegel, D. J., Brinkmann, J., Connolly, A. J., Csabai, I., Gunn, J. E., Ivezić, Ž., Lamb, D. Q., Loveday, J., Munn, J. A., Nichol, R. C., Schneider, D. P., Strauss, M. A., Szalay, A., & York, D. G. 2003, *ApJ*, 585, 694
- Eisenstein, D. J., Weinberg, D. H., Agol, E., Aihara, H., Allende Prieto, C., Anderson, S. F., Arns, J. A., Aubourg, É., Bailey, S., Balbinot, E., & et al. 2011, *AJ*, 142, 72
- Fan, X., Strauss, M. A., Gunn, J. E., Hennessy, G. S., Ivezić, Z., Knapp, G. R., Lupton, R. H., Newberg, H. J., Schneider, D. P., & Sloan Digital Sky Survey Collaboration. 1998, in *Bulletin of the American Astronomical Society*, Vol. 30, American Astronomical Society Meeting Abstracts, 1244
- Fang, J. J., Faber, S. M., Koo, D. C., & Dekel, A. 2013, *ApJ*, 776, 63
- Fang, J. J., Faber, S. M., Salim, S., Graves, G. J., & Rich, R. M. 2012, *ApJ*, 761, 23
- Fukugita, M., Ichikawa, T., Gunn, J. E., Doi, M., Shimasaku, K., & Schneider, D. P. 1996, *AJ*, 111, 1748
- Galaz, G. 2000, *AJ*, 119, 2118
- Goto, T. 2004, *A&A*, 427, 125
- Goto, T. 2005, *MNRAS*, 357, 937
- Goto, T. 2007, *MNRAS*, 381, 187
- Goto, T., Nichol, R. C., Okamura, S., Sekiguchi, M., Miller, C. J., Bernardi, M., Hopkins, A., Tremonti, C., Connolly, A., Castander, F. J., Brinkmann, J., Fukugita, M., Harvanek, M.,

- Ivezic, Z., Kleinman, S. J., Krzesinski, J., Long, D., Loveday, J., Neilsen, E. H., Newman, P. R., Nitta, A., Snedden, S. A., & Subbarao, M. 2003, PASJ, 55, 771
- Goto, T., Yagi, M., & Yamauchi, C. 2008, MNRAS, 391, 700
- Gunn, J. E., Carr, M., Rockosi, C., Sekiguchi, M., Berry, K., Elms, B., de Haas, E., Ivezić, Ž., Knapp, G., Lupton, R., Pauls, G., Simcoe, R., Hirsch, R., Sanford, D., Wang, S., York, D., Harris, F., Annis, J., Bartozek, L., Boroski, W., Bakken, J., Haldeman, M., Kent, S., Holm, S., Holmgren, D., Petravick, D., Prosapio, A., Rechenmacher, R., Doi, M., Fukugita, M., Shimasaku, K., Okada, N., Hull, C., Siegmund, W., Mannery, E., Blouke, M., Heidtman, D., Schneider, D., Lucinio, R., & Brinkman, J. 1998, AJ, 116, 3040
- Gunn, J. E. & Gott, III, J. R. 1972, ApJ, 176, 1
- Gunn, J. E., Siegmund, W. A., Mannery, E. J., Owen, R. E., Hull, C. L., Leger, R. F., Carey, L. N., Knapp, G. R., York, D. G., Boroski, W. N., Kent, S. M., Lupton, R. H., Rockosi, C. M., Evans, M. L., Waddell, P., Anderson, J. E., Annis, J., Barentine, J. C., Bartoszek, L. M., Bastian, S., Bracker, S. B., Brewington, H. J., Briegel, C. I., Brinkmann, J., Brown, Y. J., Carr, M. A., Czarapata, P. C., Drennan, C. C., Dombeck, T., Federwitz, G. R., Gillespie, B. A., Gonzales, C., Hansen, S. U., Harvanek, M., Hayes, J., Jordan, W., Kinney, E., Klaene, M., Kleinman, S. J., Kron, R. G., Kresinski, J., Lee, G., Limmongkol, S., Lindenmeyer, C. W., Long, D. C., Loomis, C. L., McGehee, P. M., Mantsch, P. M., Neilsen, Jr., E. H., Neswold, R. M., Newman, P. R., Nitta, A., Peoples, Jr., J., Pier, J. R., Prieto, P. S., Prosapio, A., Rivetta, C., Schneider, D. P., Snedden, S., & Wang, S.-i. 2006, AJ, 131, 2332
- Heymans, C., Van Waerbeke, L., Miller, L., Erben, T., Hildebrandt, H., Hoekstra, H., Kitching, T. D., Mellier, Y., Simon, P., Bonnett, C., Coupon, J., Fu, L., Harnois Déraps, J., Hudson, M. J., Kilbinger, M., Kuijken, K., Rowe, B., Schrabback, T., Semboloni, E., van Uitert, E., Vafaei, S., & Velander, M. 2012, MNRAS, 427, 146
- Hogg, D. W., Masjedi, M., Berlind, A. A., Blanton, M. R., Quintero, A. D., & Brinkmann, J. 2006, ApJ, 650, 763

Hopkins, P. F., Hernquist, L., Cox, T. J., Di Matteo, T., Robertson, B., & Springel, V. 2006, ApJS, 163, 1

Hopkins, P. F., Hernquist, L., Cox, T. J., & Kereš, D. 2008, ApJS, 175, 356

Ivezic, Z., Tyson, J. A., Abel, B., Acosta, E., Allsman, R., AlSayyad, Y., Anderson, S. F., Andrew, J., Angel, R., Angeli, G., Ansari, R., Antilogus, P., Arndt, K. T., Astier, P., Aubourg, E., Axelrod, T., Bard, D. J., Barr, J. D., Barrau, A., Bartlett, J. G., Bauman, B. J., Beaumont, S., Becker, A. C., Becla, J., Beldica, C., Bellavia, S., Blanc, G., Blandford, R. D., Bloom, J. S., Bogart, J., Borne, K., Bosch, J. F., Boutigny, D., Brandt, W. N., Brown, M. E., Bullock, J. S., Burchat, P., Burke, D. L., Cagnoli, G., Calabrese, D., Chandrasekharan, S., Chesley, S., Cheu, E. C., Chiang, J., Claver, C. F., Connolly, A. J., Cook, K. H., Cooray, A., Covey, K. R., Cribbs, C., Cui, W., Cutri, R., Daubard, G., Daues, G., Delgado, F., Digel, S., Doherty, P., Dubois, R., Dubois-Felsmann, G. P., Durech, J., Eracleous, M., Ferguson, H., Frank, J., Freemon, M., Gangler, E., Gawiser, E., Geary, J. C., Gee, P., Geha, M., Gibson, R. R., Gilmore, D. K., Glanzman, T., Goodenow, I., Gressler, W. J., Gris, P., Guyonnet, A., Hascall, P. A., Haupt, J., Hernandez, F., Hogan, C., Huang, D., Huffer, M. E., Innes, W. R., Jacoby, S. H., Jain, B., Jee, J., Jernigan, J. G., Jevremovic, D., Johns, K., Jones, R. L., Juramy-Gilles, C., Juric, M., Kahn, S. M., Kalirai, J. S., Kallivayalil, N., Kalmbach, B., Kantor, J. P., Kasliwal, M. M., Kessler, R., Kirkby, D., Knox, L., Kotov, I., Krabbendam, V. L., Krughoff, S., Kubanek, P., Kuczewski, J., Kulkarni, S., Lambert, R., Le Guillou, L., Levine, D., Liang, M., Lim, K., Lintott, C., Lupton, R. H., Mahabal, A., Marshall, P., Marshall, S., May, M., McKercher, R., Migliore, M., Miller, M., Mills, D. J., Monet, D. G., Moniez, M., Neill, D. R., Nief, J., Nomerotski, A., Nordby, M., O'Connor, P., Oliver, J., Olivier, S. S., Olsen, K., Ortiz, S., Owen, R. E., Pain, R., Peterson, J. R., Petry, C. E., Pierfederici, F., Pietrowicz, S., Pike, R., Pinto, P. A., Plante, R., Plate, S., Price, P. A., Prouza, M., Radeka, V., Rajagopal, J., Rasmussen, A., Regnault, N., Ridgway, S. T., Ritz, S., Rosing, W., Roucelle, C., Rumore, M. R., Russo, S., Saha, A., Sassolas, B., Schalk, T. L., Schindler, R. H., Schneider, D. P., Schumacher, G., Sebag, J., Sembroski, G. H., Seppala, L. G., Shipsey, I., Silvestri, N., Smith, J. A., Smith, R. C., Strauss, M. A., Stubbs, C. W., Sweeney, D., Szalay, A., Takacs, P., Thaler,

- J. J., Van Berg, R., Vanden Berk, D., Vetter, K., Virieux, F., Xin, B., Walkowicz, L., Walter, C. W., Wang, D. L., Warner, M., Willman, B., Wittman, D., Wolff, S. C., Wood-Vasey, W. M., Yoachim, P., Zhan, H., & for the LSST Collaboration. 2008, ArXiv e-prints
- Kauffmann, G., Heckman, T. M., White, S. D. M., Charlot, S., Tremonti, C., Brinchmann, J., Bruzual, G., Peng, E. W., Seibert, M., Bernardi, M., Blanton, M., Brinkmann, J., Castander, F., Csábai, I., Fukugita, M., Ivezić, Z., Munn, J. A., Nichol, R. C., Padmanabhan, N., Thakar, A. R., Weinberg, D. H., & York, D. 2003, MNRAS, 341, 33
- Koranyi, D. M. & Strauss, M. A. 1997, ApJ, 477, 36
- Krause, E., Hirata, C. M., Martin, C., Neill, J. D., & Wyder, T. K. 2013, MNRAS, 428, 2548
- Levi, M., Bebek, C., Beers, T., Blum, R., Cahn, R., Eisenstein, D., Flaugher, B., Honscheid, K., Kron, R., Lahav, O., McDonald, P., Roe, N., Schlegel, D., & representing the DESI collaboration. 2013, ArXiv e-prints
- Lupton, R., Gunn, J. E., Ivezić, Z., Knapp, G. R., & Kent, S. 2001, in Astronomical Society of the Pacific Conference Series, Vol. 238, Astronomical Data Analysis Software and Systems X, ed. F. R. Harnden, Jr., F. A. Primini, & H. E. Payne, 269
- Lupton, R. H., Gunn, J. E., & Szalay, A. S. 1999, AJ, 118, 1406
- Madau, P. & Dickinson, M. 2014, ARA&A, 52, 415
- Maraston, C. 2005, MNRAS, 362, 799
- Mihos, J. C. & Hernquist, L. 1994, ApJ, 431, L9
- Miller, N. A. & Owen, F. N. 2001, ApJ, 554, L25
- Miyazaki, S., Komiyama, Y., Nakaya, H., Kamata, Y., Doi, Y., Hamana, T., Karoji, H., Furusawa, H., Kawanomoto, S., Morokuma, T., Ishizuka, Y., Nariai, K., Tanaka, Y., Uruguchi, F., Utsumi, Y., Obuchi, Y., Okura, Y., Oguri, M., Takata, T., Tomono, D., Kurakami, T., Namikawa, K., Usuda, T., Yamanoi, H., Terai, T., Uekiyo, H., Yamada, Y., Koike, M., Aihara,

- H., Fujimori, Y., Mineo, S., Miyatake, H., Yasuda, N., Nishizawa, J., Saito, T., Tanaka, M., Uchida, T., Katayama, N., Wang, S.-Y., Chen, H.-Y., Lupton, R., Loomis, C., Bickerton, S., Price, P., Gunn, J., Suzuki, H., Miyazaki, Y., Muramatsu, M., Yamamoto, K., Endo, M., Ezaki, Y., Itoh, N., Miwa, Y., Yokota, H., Matsuda, T., Ebinuma, R., & Takeshi, K. 2012, in Society of Photo-Optical Instrumentation Engineers (SPIE) Conference Series, Vol. 8446, Society of Photo-Optical Instrumentation Engineers (SPIE) Conference Series
- Nielsen, D. M., Ridgway, S. E., De Propriis, R., & Goto, T. 2012, *ApJ*, 761, L16
- Norton, S. A., Gebhardt, K., Zabludoff, A. I., & Zaritsky, D. 2001, *ApJ*, 557, 150
- Petrosian, V. 1976, *ApJ*, 209, L1
- Poggianti, B. M., Aragón-Salamanca, A., Zaritsky, D., De Lucia, G., Milvang-Jensen, B., Desai, V., Jablonka, P., Halliday, C., Rudnick, G., Varela, J., Bamford, S., Best, P., Clowe, D., Noll, S., Saglia, R., Pelló, R., Simard, L., von der Linden, A., & White, S. 2009, *ApJ*, 693, 112
- Poggianti, B. M. & Wu, H. 2000, *ApJ*, 529, 157
- Pracy, M. B., Couch, W. J., Blake, C., Bekki, K., Harrison, C., Colless, M., Kuntschner, H., & de Propriis, R. 2005, *MNRAS*, 359, 1421
- Pracy, M. B., Couch, W. J., & Kuntschner, H. 2010, *PASA*, 27, 360
- Pracy, M. B., Kuntschner, H., Couch, W. J., Blake, C., Bekki, K., & Briggs, F. 2009, *MNRAS*, 396, 1349
- Pracy, M. B., Owers, M. S., Couch, W. J., Kuntschner, H., Bekki, K., Briggs, F., Lah, P., & Zwaan, M. 2012, *MNRAS*, 420, 2232
- Quintero, A. D., Hogg, D. W., Blanton, M. R., Schlegel, D. J., Eisenstein, D. J., Gunn, J. E., Brinkmann, J., Fukugita, M., Glazebrook, K., & Goto, T. 2004, *ApJ*, 602, 190
- Richards, G. T., Fan, X., Newberg, H. J., Strauss, M. A., Vanden Berk, D. E., Schneider, D. P., Yanny, B., Boucher, A., Burles, S., Frieman, J. A., Gunn, J. E., Hall, P. B., Ivezić, Ž., Kent, S.,

- Loveday, J., Lupton, R. H., Rockosi, C. M., Schlegel, D. J., Stoughton, C., SubbaRao, M., & York, D. G. 2002, *AJ*, 123, 2945
- Salim, S., Fang, J. J., Rich, R. M., Faber, S. M., & Thilker, D. A. 2012, *ApJ*, 755, 105
- Sandage, A., Tammann, G. A., & Yahil, A. 1979, *ApJ*, 232, 352
- Sanders, D. B., Soifer, B. T., Elias, J. H., Madore, B. F., Matthews, K., Neugebauer, G., & Scoville, N. Z. 1988, *ApJ*, 325, 74
- Schawinski, K., Urry, C. M., Simmons, B. D., Fortson, L., Kaviraj, S., Keel, W. C., Lintott, C. J., Masters, K. L., Nichol, R. C., Sarzi, M., Skibba, R., Treister, E., Willett, K. W., Wong, O. I., & Yi, S. K. 2014, *MNRAS*, 440, 889
- Schlegel, D. J., Finkbeiner, D. P., & Davis, M. 1998, *ApJ*, 500, 525
- Sell, P. H., Tremonti, C. A., Hickox, R. C., Diamond-Stanic, A. M., Moustakas, J., Coil, A., Williams, A., Rudnick, G., Robaina, A., Geach, J. E., Heinz, S., & Wilcots, E. M. 2014, *MNRAS*, 441, 3417
- Shin, M.-S., Strauss, M. A., & Tojeiro, R. 2011, *MNRAS*, 410, 1583
- Sijacki, D., Springel, V., Di Matteo, T., & Hernquist, L. 2007, *MNRAS*, 380, 877
- Smee, S. A., Gunn, J. E., Uomoto, A., Roe, N., Schlegel, D., Rockosi, C. M., Carr, M. A., Leger, F., Dawson, K. S., Olmstead, M. D., Brinkmann, J., Owen, R., Barkhouser, R. H., Honscheid, K., Harding, P., Long, D., Lupton, R. H., Loomis, C., Anderson, L., Annis, J., Bernardi, M., Bhardwaj, V., Bizyaev, D., Bolton, A. S., Brewington, H., Briggs, J. W., Burles, S., Burns, J. G., Castander, F. J., Connolly, A., Davenport, J. R. A., Ebelke, G., Epps, H., Feldman, P. D., Friedman, S. D., Frieman, J., Heckman, T., Hull, C. L., Knapp, G. R., Lawrence, D. M., Loveday, J., Mannery, E. J., Malanushenko, E., Malanushenko, V., Merrelli, A. J., Muna, D., Newman, P. R., Nichol, R. C., Oravetz, D., Pan, K., Pope, A. C., Ricketts, P. G., Shelden, A., Sandford, D., Siegmund, W., Simmons, A., Smith, D. S., Snedden, S., Schneider, D. P., SubbaRao, M., Tremonti, C., Waddell, P., & York, D. G. 2013, *AJ*, 146, 32

- Snyder, G. F., Cox, T. J., Hayward, C. C., Hernquist, L., & Jonsson, P. 2011, *ApJ*, 741, 77
- Strauss, M. A., Weinberg, D. H., Lupton, R. H., Narayanan, V. K., Annis, J., Bernardi, M., Blanton, M., Burles, S., Connolly, A. J., Dalcanton, J., Doi, M., Eisenstein, D., Frieman, J. A., Fukugita, M., Gunn, J. E., Ivezić, Ž., Kent, S., Kim, R. S. J., Knapp, G. R., Kron, R. G., Munn, J. A., Newberg, H. J., Nichol, R. C., Okamura, S., Quinn, T. R., Richmond, M. W., Schlegel, D. J., Shimasaku, K., SubbaRao, M., Szalay, A. S., Vanden Berk, D., Vogeley, M. S., Yanny, B., Yasuda, N., York, D. G., & Zehavi, I. 2002, *AJ*, 124, 1810
- SubbaRao, M., Frieman, J., Bernardi, M., Loveday, J., Nichol, B., Castander, F., & Meiksin, A. 2002, in *Society of Photo-Optical Instrumentation Engineers (SPIE) Conference Series*, Vol. 4847, *Astronomical Data Analysis II*, ed. J.-L. Starck & F. D. Murtagh, 452–460
- Swinbank, M., Balogh, M., Bower, R., Zabludoff, A., Lucey, J., McGee, S., Miller, C., & Nichol, R. 2011, *ArXiv e-prints*
- Takada, M., Ellis, R. S., Chiba, M., Greene, J. E., Aihara, H., Arimoto, N., Bundy, K., Cohen, J., Doré, O., Graves, G., Gunn, J. E., Heckman, T., Hirata, C. M., Ho, P., Kneib, J.-P., Fèvre, O. L., Lin, L., More, S., Murayama, H., Nagao, T., Ouchi, M., Seiffert, M., Silverman, J. D., Sodr e, L., Spergel, D. N., Strauss, M. A., Sugai, H., Suto, Y., Takami, H., & Wyse, R. 2014, *PASJ*, 66, 1
- The Dark Energy Survey Collaboration. 2005, *ArXiv Astrophysics e-prints*
- Tran, K.-V. H., Franx, M., Illingworth, G., Kelson, D. D., & van Dokkum, P. 2003, *ApJ*, 599, 865
- Tran, K.-V. H., Franx, M., Illingworth, G. D., van Dokkum, P., Kelson, D. D., & Magee, D. 2004, *ApJ*, 609, 683
- Tremonti, C. A., Moustakas, J., & Diamond-Stanic, A. M. 2007, *ApJ*, 663, L77
- Vacca, W. D., Cushing, M. C., & Rayner, J. T. 2003, *PASP*, 115, 389
- Vergani, D., Zamorani, G., Lilly, S., Lamareille, F., Halliday, C., Scodreggio, M., Vignali, C., Ciliegi, P., Bolzonella, M., Bondi, M., Kovač, K., Knobel, C., Zucca, E., Caputi, K., Pozzetti,

- L., Bardelli, S., Mignoli, M., Iovino, A., Carollo, C. M., Contini, T., Kneib, J.-P., Le Fèvre, O., Mainieri, V., Renzini, A., Bongiorno, A., Coppa, G., Cucciati, O., de la Torre, S., de Ravel, L., Franzetti, P., Garilli, B., Kampczyk, P., Le Borgne, J.-F., Le Brun, V., Maier, C., Pello, R., Peng, Y., Perez Montero, E., Ricciardelli, E., Silverman, J. D., Tanaka, M., Tasca, L., Tresse, L., Abbas, U., Bottini, D., Cappi, A., Cassata, P., Cimatti, A., Guzzo, L., Koekemoer, A. M., Leauthaud, A., Maccagni, D., Marinoni, C., McCracken, H. J., Memeo, P., Meneux, B., Oesch, P., Porciani, C., Scaramella, R., Capak, P., Sanders, D., Scoville, N., & Taniguchi, Y. 2010, *A&A*, 509, A42
- Whitaker, K. E., Kriek, M., van Dokkum, P. G., Bezanson, R., Brammer, G., Franx, M., & Labbé, I. 2012, *ApJ*, 745, 179
- Wild, V., Almaini, O., Cirasuolo, M., Dunlop, J., McLure, R., Bowler, R., Ferreira, J., Bradshaw, E., Chuter, R., & Hartley, W. 2014, *MNRAS*, 440, 1880
- Wild, V., Heckman, T., & Charlot, S. 2010, *MNRAS*, 405, 933
- Wild, V., Kauffmann, G., Heckman, T., Charlot, S., Lemson, G., Brinchmann, J., Reichard, T., & Pasquali, A. 2007, *MNRAS*, 381, 543
- Wilson, J. C., Henderson, C. P., Herter, T. L., Matthews, K., Skrutskie, M. F., Adams, J. D., Moon, D.-S., Smith, R., Gautier, N., Ressler, M., Soifer, B. T., Lin, S., Howard, J., LaMarr, J., Stolberg, T. M., & Zink, J. 2004, in *Society of Photo-Optical Instrumentation Engineers (SPIE) Conference Series*, Vol. 5492, *Ground-based Instrumentation for Astronomy*, ed. A. F. M. Moorwood & M. Iye, 1295–1305
- Yagi, M. & Goto, T. 2006, *AJ*, 131, 2050
- Yan, R., Newman, J. A., Faber, S. M., Coil, A. L., Cooper, M. C., Davis, M., Weiner, B. J., Gerke, B. F., & Koo, D. C. 2009, *MNRAS*, 398, 735
- Yan, R., Newman, J. A., Faber, S. M., Konidaris, N., Koo, D., & Davis, M. 2006, *ApJ*, 648, 281
- Yang, Y., Zabludoff, A. I., Zaritsky, D., Lauer, T. R., & Mihos, J. C. 2004, *ApJ*, 607, 258

Yang, Y., Zabludoff, A. I., Zaritsky, D., & Mihos, J. C. 2008, ApJ, 688, 945

Yasuda, N., Fukugita, M., Narayanan, V. K., Lupton, R. H., Strateva, I., Strauss, M. A., Ivezić, Ž., Kim, R. S. J., Hogg, D. W., Weinberg, D. H., Shimasaku, K., Loveday, J., Annis, J., Bahcall, N. A., Blanton, M., Brinkmann, J., Brunner, R. J., Connolly, A. J., Csabai, I., Doi, M., Hamabe, M., Ichikawa, S.-I., Ichikawa, T., Johnston, D. E., Knapp, G. R., Kunszt, P. Z., Lamb, D. Q., McKay, T. A., Munn, J. A., Nichol, R. C., Okamura, S., Schneider, D. P., Szokoly, G. P., Vogeley, M. S., Watanabe, M., & York, D. G. 2001, AJ, 122, 1104

Yesuf, H. M., Faber, S. M., Trump, J. R., Koo, D. C., Fang, J. J., Liu, F. S., Wild, V., & Hayward, C. C. 2014, ApJ, 792, 84

York, D. G., Adelman, J., Anderson, Jr., J. E., Anderson, S. F., Annis, J., Bahcall, N. A., Bakken, J. A., Barkhouser, R., Bastian, S., Berman, E., Boroski, W. N., Bracker, S., Briegel, C., Briggs, J. W., Brinkmann, J., Brunner, R., Burles, S., Carey, L., Carr, M. A., Castander, F. J., Chen, B., Colestock, P. L., Connolly, A. J., Crocker, J. H., Csabai, I., Czarapata, P. C., Davis, J. E., Doi, M., Dombeck, T., Eisenstein, D., Ellman, N., Elms, B. R., Evans, M. L., Fan, X., Federwitz, G. R., Fiscelli, L., Friedman, S., Frieman, J. A., Fukugita, M., Gillespie, B., Gunn, J. E., Gurbani, V. K., de Haas, E., Haldeman, M., Harris, F. H., Hayes, J., Heckman, T. M., Hennessy, G. S., Hindsley, R. B., Holm, S., Holmgren, D. J., Huang, C.-h., Hull, C., Husby, D., Ichikawa, S.-I., Ichikawa, T., Ivezić, Ž., Kent, S., Kim, R. S. J., Kinney, E., Klaene, M., Kleinman, A. N., Kleinman, S., Knapp, G. R., Korienek, J., Kron, R. G., Kunszt, P. Z., Lamb, D. Q., Lee, B., Leger, R. F., Limmongkol, S., Lindenmeyer, C., Long, D. C., Loomis, C., Loveday, J., Lucinio, R., Lupton, R. H., MacKinnon, B., Mannery, E. J., Mantsch, P. M., Margon, B., McGehee, P., McKay, T. A., Meiksin, A., Merelli, A., Monet, D. G., Munn, J. A., Narayanan, V. K., Nash, T., Neilsen, E., Neswold, R., Newberg, H. J., Nichol, R. C., Nicinski, T., Nonino, M., Okada, N., Okamura, S., Ostriker, J. P., Owen, R., Pauls, A. G., Peoples, J., Peterson, R. L., Petravick, D., Pier, J. R., Pope, A., Pordes, R., Prosapio, A., Rechenmacher, R., Quinn, T. R., Richards, G. T., Richmond, M. W., Rivetta, C. H., Rockosi, C. M., Ruthmansdorfer, K., Sandford, D., Schlegel, D. J., Schneider, D. P., Sekiguchi, M., Sergey, G.,

Shimasaku, K., Siegmund, W. A., Smee, S., Smith, J. A., Snedden, S., Stone, R., Stoughton, C., Strauss, M. A., Stubbs, C., SubbaRao, M., Szalay, A. S., Szapudi, I., Szokoly, G. P., Thakar, A. R., Tremonti, C., Tucker, D. L., Uomoto, A., Vanden Berk, D., Vogeley, M. S., Waddell, P., Wang, S.-i., Watanabe, M., Weinberg, D. H., Yanny, B., Yasuda, N., & SDSS Collaboration. 2000, *AJ*, 120, 1579

Zabludoff, A. I., Zaritsky, D., Lin, H., Tucker, D., Hashimoto, Y., Shectman, S. A., Oemler, A., & Kirshner, R. P. 1996, *ApJ*, 466, 104

Post-starburst Galaxies from DR12

1 Introduction

In the previous chapter, we studied the post-starburst galaxy sample and its redshift evolution from the Ninth Release (DR9) of the SDSS spectroscopic sample (Ahn et al., 2012). The sample of more than 6000 objects was found over a range of redshift from the local universe up to $z \sim 1.3$. Out of this sample, about 2000 objects are from the SDSS-I/II spectroscopic database (DR7; Abazajian et al. (2009)). These SDSS-I/II post-starburst galaxies are primarily selected through the Main Galaxy Sample target selection (Strauss et al., 2002). The other 4000 objects are from the SDSS-III Baryon Oscillation Spectroscopic Survey (BOSS) spectra (Dawson et al., 2013), and are primarily selected through the CMASS galaxy sample. The median redshift of the SDSS-I/II post-starburst galaxy sample is $z_{\text{median}} \sim 0.2$, while that of the SDSS-III BOSS sample is $z_{\text{median}} \sim 0.6$.

From this sample, we calculated the luminosity function of these objects for a number of redshift bins ranging from $z \sim 0.8$ down to $z \sim 0.1$. The luminosity functions show a rapid redshift evolution in a downsizing manner, with a larger number density of post-starburst galaxies at fixed luminosity at higher redshift. Through the luminosity functions, we calculated the contribution of post-starburst galaxies to the star-formation quenching that happens in the universe as a function of redshift, and compare this to the amount required by the global decline in star-formation rate presented by Madau & Dickinson (2014). We found that post-starburst galaxies only contribute to about 0.2% of all star-formation quenching at all redshift less than unity (Pattarakijwanich et al., 2014). We concluded that the star-formation quenching must either happen in low-mass galaxies or satellites that are not part of the survey, or that the

quenching must happen gradually enough that the stellar population never has the spectral signature of post-starburst galaxies (similar to the star-formation history of the Milky Way).

Since the time of that study, the SDSS has significantly progressed, and now has made the Twelfth Data Release (DR12) publicly available (Alam et al., 2015). The amount of data has grown by approximately three times, with the effective area with spectroscopic data grown from 3275 square degrees in DR9 to 9376 square degrees in DR12, and the number of unique BOSS spectra from 7.6×10^5 in DR9 to 2.3×10^6 in DR12.

In this section, we repeat the study of post-starburst galaxies from this bigger dataset to update our previous results. Section 2 describes the new post-starburst galaxy selection method which is modified based on lessons learned from last time. Section 3 describes the BOSS DR12 post-starburst galaxy sample. The luminosity function analysis on the new sample is described in Section 4.

2 Modified Selection Method

The selection method used to select the post-starburst galaxies from the SDSS DR12 spectroscopic data is modified slightly from previously, based on lessons learned from last round of selection. The modifications are done in such a way that make the selection faster and easier, while the efficiency and completeness of the final sample are not affected significantly.

The first modification is to use the redshifts as determined from the SDSS spectroscopic pipeline. In the previous work we did not assume any a priori knowledge of redshift and therefore searched the whole possible redshift range. It was found that the redshift accuracy for BOSS galaxies are very high, with an incorrect redshift rate of only about 2%. These objects with wrong redshifts also have ZWARNING flag to mark the uncertainty. As such, in this current selection we simply adopt the redshifts given by the pipeline.

The other major change is to remove all objects classified as stars from consideration. This criteria was not applied in previous work, and we found some objects with star classification which are clearly post-starburst galaxies based on their spectra. However, the number was very small and to improve the ease of the search we simply exclude objects classified as stars this time.

Otherwise, other major selection criteria remain the same. We still require significant absorption H δ line and lack of strong emission in OII λ 3727 lines, which indicate large recent starburst but no ongoing star formation. The exact criteria are $EW(H\delta) > 4.0$, and $EW(OII\lambda 3727) < -2.5$ respectively, where EW denotes the equivalent width, and positive sign means absorption in our convention. The ratio A/Total, defined in the rest-frame wavelength range 4150-4300Å using the K and A stellar spectral template fit with quadratic continuum is still required to be $A/Total > 0.25$, in order to ensure significant amount of contribution from A-star to the spectra. In the end, every object that passes these automated criteria is visually inspected to ensure that the fit is correct and valid.

3 Sample

We applied the automatic selection algorithm described previously in Section 2 to the SDSS DR12 BOSS spectroscopic data, and identified 11665 objects as possible post-starburst galaxy candidates. These objects are then visually inspected, resulting in the final sample of 10889 post-starburst galaxies. The median redshift of this sample is $z_{\text{median}} \sim 0.62$ with the objects ranging from the local universe to redshift as high as $z = 1.318$.

It should also be noted that the modified selection algorithm works very well, with only about 7% of the automatically identified objects being rejected by visual inspection, compared to a factor of more than 2 in the previous attempt on the DR9. The primary reason for this improvement is because we now adopt the redshifts as determined by the SDSS spectroscopic pipeline, and not let the redshift be a free parameter as previously. This shows further the robustness of the SDSS spectroscopic pipeline.

The redshift distribution of the DR12 post-starburst galaxy sample is shown in Figure 3.1 compared to that of the previous DR9 sample. While the number of objects in the DR12 sample is bigger by approximately a factor of 3, the shapes of the two distributions do not differ significantly. The increase in number agrees with the increase in survey area, which has grown by the same factor. We therefore confirm that the selection method used for the DR12 sample,

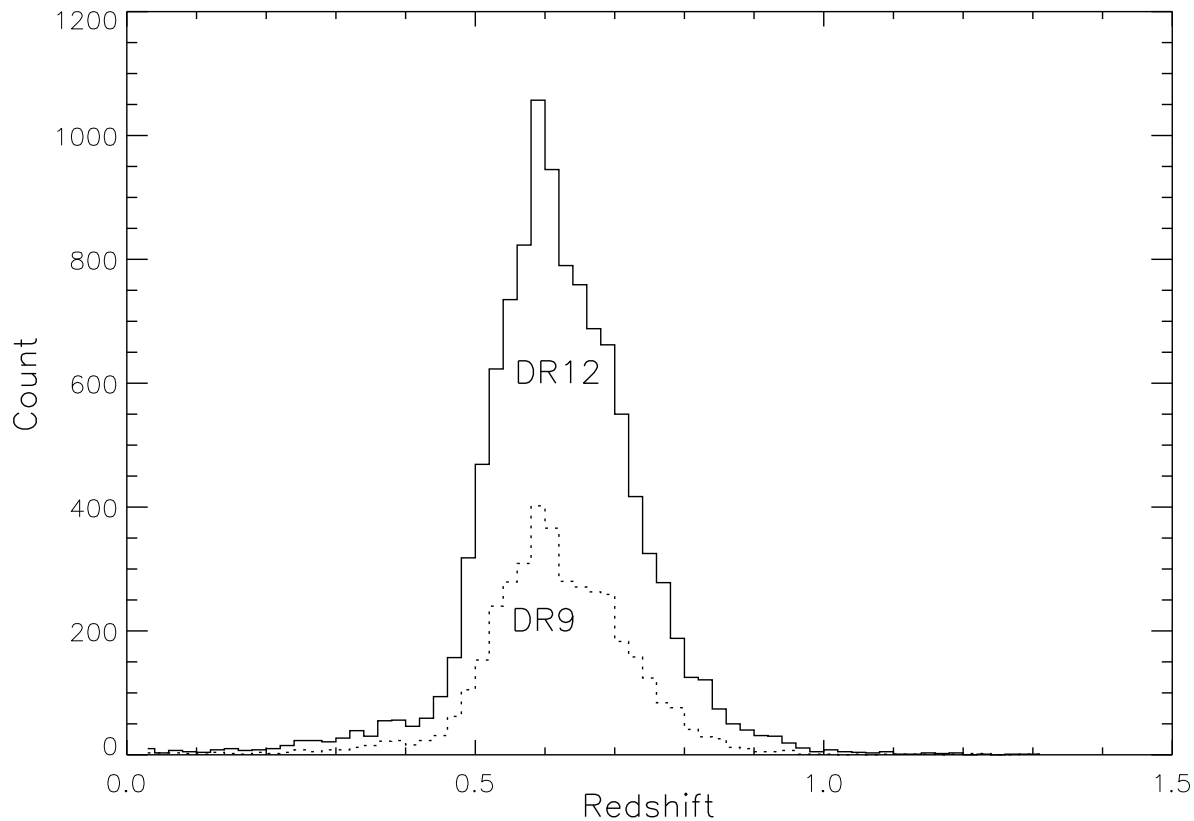


Figure 3.1 Redshift distributions of the post-starburst galaxies selected from the Ninth Data Release (DR9) and the Twelfth Data Release (DR12) of the SDSS spectroscopic data.

despite all the modifications described in the previous section, does not produce a significantly different sample from the previous one.

4 Luminosity Function

Another key result from the DR9 post-starburst galaxy sample is the redshift evolution of the luminosity function. In previous work, we calculated the luminosity function in different redshift bins with various selection biases carefully taken care of. We found a rapid downsizing trend of the luminosity function with redshift, where the number density of post-starburst galaxies at fixed luminosity is larger at higher redshift.

The detailed explanation of the method can be found in previous work, but here we review the important aspects. There are two major selection effects that need to be corrected for. The first is the fact that the CMASS galaxies are selected into the spectroscopic sample using color selection criteria designed to find massive early-type galaxies in the redshift range around $z \sim 0.5$, meaning that an object observed at some redshift might not be selected into the spectroscopic sample had it been placed at some different redshifts. This is corrected by simulating the photometry that would be observed at any redshift from the known spectra, with signal-to-noise effect taken into account using Monte Carlo simulations, by asking what fraction of objects would be selected using our criteria under different noise realizations. This results in the effective cosmological volume V_{\max} that any CMASS object could be selected into the SDSS spectroscopic sample and subsequently our post-starburst galaxy sample. The second effect is the cut in color-magnitude space used to select the CMASS galaxies, which is again originally designed to select early-type galaxies. However, there is no reason that the post-starburst galaxies should not exist in the region excluded by this arbitrary cuts, thus this would bias the resulted distribution. We corrected for this by assuming that the distributions in color and magnitude are independent - an assumption that is supported by the data - and then use the distribution in the region of the color-magnitude space that is complete to estimate the number of post-starburst galaxies in the excluded region. After correcting for these two selection effects, we believe we have derived an unbiased luminosity function.

With the new DR12 sample, we repeat the luminosity function calculation for the CMASS-selected post-starburst galaxies. The number of objects in the sample increases by a factor of about three, with detailed numbers in each redshift bin shown in Table 3.1. The new luminosity functions are shown in Figure 3.2 compared to the ones from the previous work in the same redshift bins. While the error bars are smaller as expected from the larger sample size, the luminosity functions do not change significantly between the DR9 to the DR12 improvement.

The fact that the shape of the post-starburst galaxy luminosity functions do not change significantly with larger sample size is reassuring, in particular because it confirms the previous results that the post-starburst galaxy luminosity function is reasonably well-fitted by log-normal

Redshift Range	DR9		DR12	
	CMASS	All	CMASS	All
$z < 0.55$	364	914	1093	2492
$0.55 < z < 0.65$	1133	1614	3394	4381
$0.65 < z < 0.65$	778	1066	2263	2850
$z > 0.75$	181	370	565	1166

Table 3.1 Number of CMASS-selected post-starburst galaxies from the SDSS DR9 and DR12 that are used to calculate the luminosity function in each redshift bin.

distribution in luminosity. The log-normal luminosity function is somewhat unusual compared to the Schechter function found in most galaxy populations, although it has been found in classical elliptical galaxies (Sandage et al., 1985).

The key results from the previous work are updated to the bigger sample and shown in Figure 3.3 and Figure 3.4. Figure 3.3 shows the luminosity functions as a function of redshift bins, with both the low-redshift bins derived from the unchanged SDSS I/II Main Galaxy Sample, and the high-redshift bins from the updated BOSS CMASS sample. Figure 3.4 shows the A-star mass density in the post-starburst galaxies calculated from the luminosity functions, compared to the amount expected from the decrease in global star formation rate of the universe at different redshifts. The main conclusions of the previous work that the amount of star formation quenching in post-starburst galaxies only represents a small fraction of all star formation quenching in the universe is still valid. It is expected that the rest of the star formation quenching happens in either low-mass galaxies that are not in the survey sample, or in a form of a gradual decrease in star formation without a sharp drop as is the case in our Milky Way.

Bibliography

- Abazajian, K. N., Adelman-McCarthy, J. K., Agüeros, M. A., Allam, S. S., Allende Prieto, C., An, D., Anderson, K. S. J., Anderson, S. F., Annis, J., Bahcall, N. A., & et al. 2009, *ApJS*, 182, 543
- Ahn, C. P., Alexandroff, R., Allende Prieto, C., Anderson, S. F., Anderton, T., Andrews, B. H.,

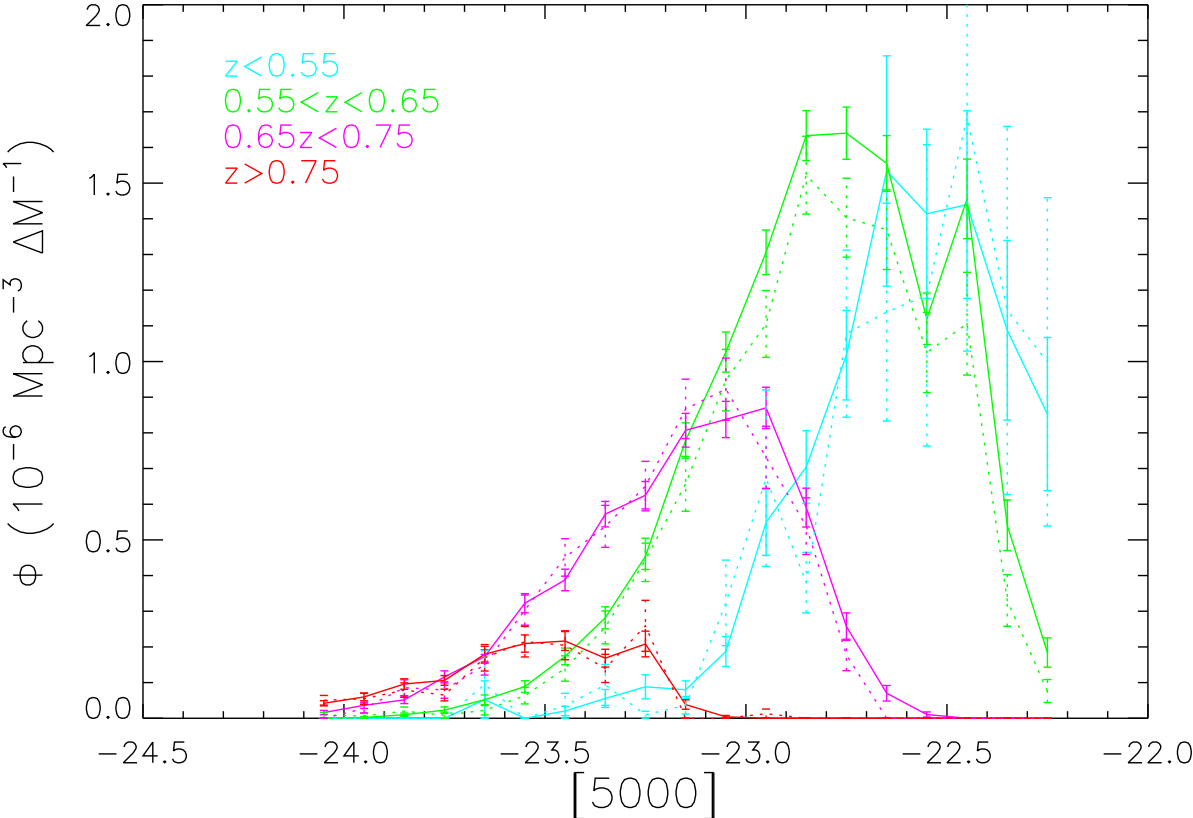


Figure 3.2 The luminosity functions of the post-starburst galaxies selected from SDSS DR12 (solid lines) compared to that from the DR9 from previous work (dotted lines). Different redshift bins are represented by different colors.

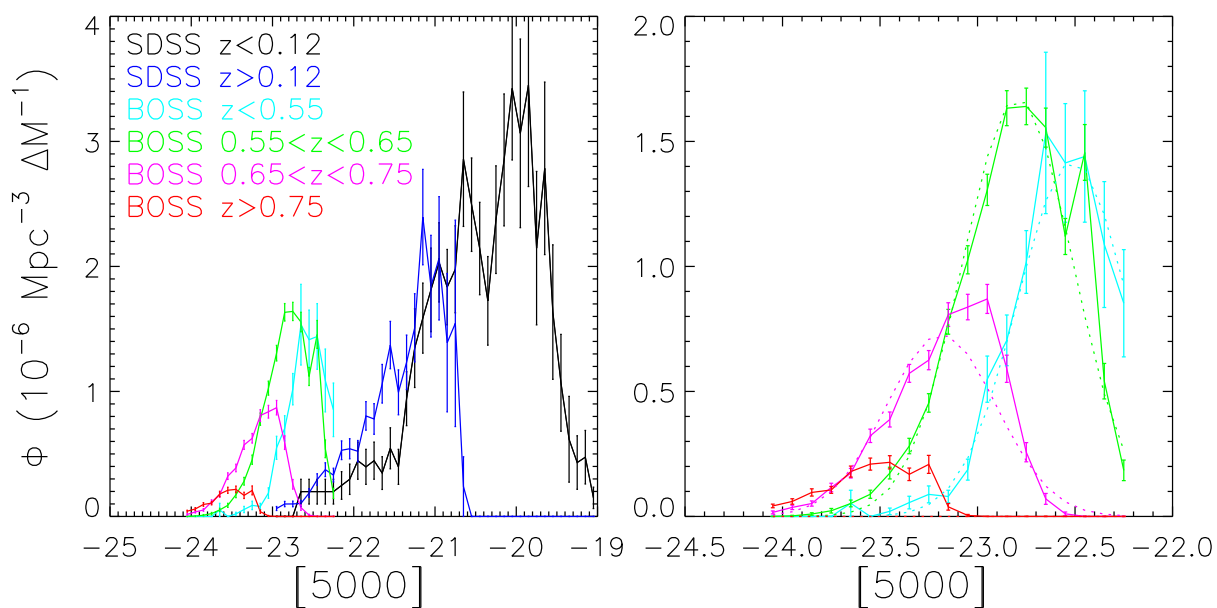


Figure 3.3 Updated luminosity functions as a function of redshift using the new BOSS CMASS sample selected from the SDSS DR12 spectroscopic data. The low-redshift bins from SDSS Main Galaxy Sample remain unchanged. The left panel shows all redshift bins, while the right panel is a zoomed-in version to show the BOSS CMASS bins more clearly.

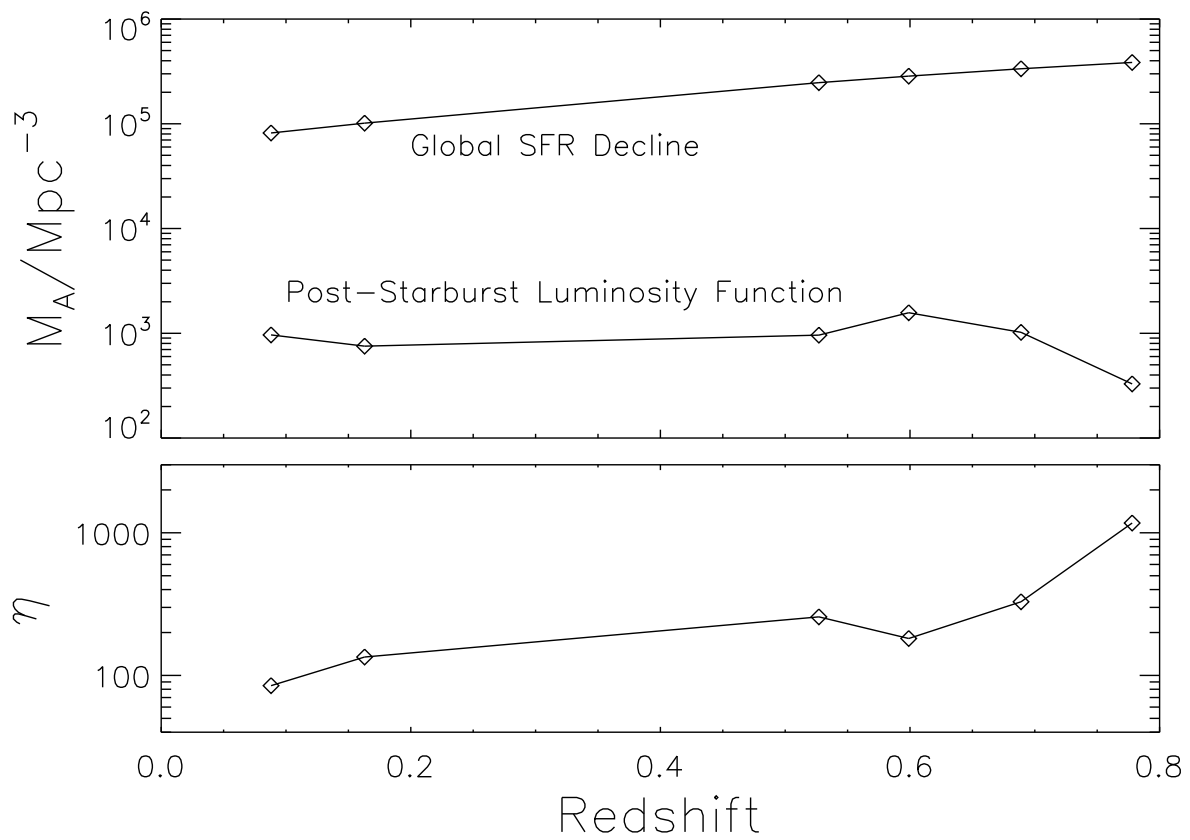


Figure 3.4 Top panel: A-star mass density in post-starburst galaxies as a function of redshift calculated from the luminosity functions, compared to the amount expected to be present based on the decline in the global star formation rate of the universe (Madau & Dickinson, 2014).

- Aubourg, É., Bailey, S., Balbinot, E., Barnes, R., & et al. 2012, *ApJS*, 203, 21
- Alam, S., Albareti, F. D., Allende Prieto, C., Anders, F., Anderson, S. F., Anderton, T.,
Andrews, B. H., Armengaud, E., Aubourg, É., Bailey, S., & et al. 2015, *ApJS*, 219, 12
- Dawson, K. S., Schlegel, D. J., Ahn, C. P., Anderson, S. F., Aubourg, É., Bailey, S., Barkhouser,
R. H., Bautista, J. E., Beifiori, A., Berlind, A. A., Bhardwaj, V., Bizyaev, D., Blake, C. H.,
Blanton, M. R., Blomqvist, M., Bolton, A. S., Borde, A., Bovy, J., Brandt, W. N., Brewington,
H., Brinkmann, J., Brown, P. J., Brownstein, J. R., Bundy, K., Busca, N. G., Carithers, W.,
Carnero, A. R., Carr, M. A., Chen, Y., Comparat, J., Connolly, N., Cope, F., Croft, R. A. C.,
Cuesta, A. J., da Costa, L. N., Davenport, J. R. A., Delubac, T., de Putter, R., Dhital, S.,
Ealet, A., Ebelke, G. L., Eisenstein, D. J., Escoffier, S., Fan, X., Filiz Ak, N., Finley, H.,
Font-Ribera, A., Génova-Santos, R., Gunn, J. E., Guo, H., Haggard, D., Hall, P. B., Hamilton,
J.-C., Harris, B., Harris, D. W., Ho, S., Hogg, D. W., Holder, D., Honscheid, K., Huehnerhoff,
J., Jordan, B., Jordan, W. P., Kauffmann, G., Kazin, E. A., Kirkby, D., Klaene, M. A., Kneib,
J.-P., Le Goff, J.-M., Lee, K.-G., Long, D. C., Loomis, C. P., Lundgren, B., Lupton, R. H.,
Maia, M. A. G., Makler, M., Malanushenko, E., Malanushenko, V., Mandelbaum, R., Manera,
M., Maraston, C., Margala, D., Masters, K. L., McBride, C. K., McDonald, P., McGreer, I. D.,
McMahon, R. G., Mena, O., Miralda-Escudé, J., Montero-Dorta, A. D., Montesano, F., Muna,
D., Myers, A. D., Naugle, T., Nichol, R. C., Noterdaeme, P., Nuza, S. E., Olmstead, M. D.,
Oravetz, A., Oravetz, D. J., Owen, R., Padmanabhan, N., Palanque-Delabrouille, N., Pan, K.,
Parejko, J. K., Pâris, I., Percival, W. J., Pérez-Fournon, I., Pérez-Ràfols, I., Petitjean, P.,
Pfaffenberger, R., Pforr, J., Pieri, M. M., Prada, F., Price-Whelan, A. M., Raddick, M. J.,
Rebolo, R., Rich, J., Richards, G. T., Rockosi, C. M., Roe, N. A., Ross, A. J., Ross, N. P.,
Rossi, G., Rubiño-Martín, J. A., Samushia, L., Sánchez, A. G., Sayres, C., Schmidt, S. J.,
Schneider, D. P., Scóccola, C. G., Seo, H.-J., Sheldon, A., Sheldon, E., Shen, Y., Shu, Y.,
Slosar, A., Smee, S. A., Snedden, S. A., Stauffer, F., Steele, O., Strauss, M. A., Streblyanska,
A., Suzuki, N., Swanson, M. E. C., Tal, T., Tanaka, M., Thomas, D., Tinker, J. L., Tojeiro, R.,
Tremonti, C. A., Vargas Magaña, M., Verde, L., Viel, M., Wake, D. A., Watson, M., Weaver,

- B. A., Weinberg, D. H., Weiner, B. J., West, A. A., White, M., Wood-Vasey, W. M., Yeche, C., Zehavi, I., Zhao, G.-B., & Zheng, Z. 2013, *AJ*, 145, 10
- Madau, P. & Dickinson, M. 2014, *ARA&A*, 52, 415
- Pattarakijwanich, P., Strauss, M. A., Ho, S., & Ross, N. P. 2014, ArXiv e-prints
- Sandage, A., Binggeli, B., & Tammann, G. A. 1985, *AJ*, 90, 1759
- Strauss, M. A., Weinberg, D. H., Lupton, R. H., Narayanan, V. K., Annis, J., Bernardi, M., Blanton, M., Burles, S., Connolly, A. J., Dalcanton, J., Doi, M., Eisenstein, D., Frieman, J. A., Fukugita, M., Gunn, J. E., Ivezić, Ž., Kent, S., Kim, R. S. J., Knapp, G. R., Kron, R. G., Munn, J. A., Newberg, H. J., Nichol, R. C., Okamura, S., Quinn, T. R., Richmond, M. W., Schlegel, D. J., Shimasaku, K., SubbaRao, M., Szalay, A. S., Vanden Berk, D., Vogeley, M. S., Yanny, B., Yasuda, N., York, D. G., & Zehavi, I. 2002, *AJ*, 124, 1810

Search for Post-starburst Quasars

1 Introduction

One major mechanism potentially responsible for quenching star formation in galaxies is the feedback from the activity of the central supermassive black hole. In this crude picture, gas accretion or a major galaxy merger starts an episode of both star-formation activity and gas accretion to the central super-massive black hole, fueling the AGN activity. These activities eventually cease due to either feedback from the star formation or AGN, or simply by gas exhaustion, and the galaxies enter the evolutionary track to becoming quiescent. However, the order and timescale of star formation and AGN activity that are triggered are not well understood.

A detailed theoretical study by Cen (2012) suggests that a starburst episode is triggered right after the merger and lasts for about a million years. During this time, the main feedback mechanism that keeps the gas hot is from the starburst itself. The central black hole has low gas accretion rate and stays relatively quiet. After this episode of starburst stops is the prime growth period for the central black hole, when it starts growing rapidly by feeding on recycled gas from the aging bulge stars. This period of strong AGN activity, happening at several million years after the starburst, would coincide with the stellar population being in the post-starburst phase.

Given this scenario, one class of object of interest is the so-called post-starburst quasar. These are objects that have both a post-starburst stellar population and the central supermassive black hole in an active phase. By identifying a sample of post-starburst quasars and studying them, we can learn potentially important insights about the evolution track from starburst to quiescent elliptical galaxies.

The study of post-starburst quasars began when Brotherton et al. (1999) discovered the post-starburst quasar prototype UN J1025-0040 at redshift $z = 0.634$. This object has strong Balmer series absorption indicative of intermediate age stellar population, with a broad MgII emission line from AGN activity. Canalizo et al. (2000) confirmed that the visual companion of this object is at the same redshift, and Brotherton et al. (2002) obtained high-resolution HST images of this object showing disturbed morphology. Together these papers painted the coherent picture that the interaction with the companion triggers both the starburst and AGN activity in this object.

A number of authors have studied different aspects of individual post-starburst quasars in small samples. Wei et al. (2013) obtained Spitzer mid-infrared spectra of 16 post-starburst quasars. Their infrared properties are between that of the ULIRGs and quasars, suggesting they might be the intermediate step between the two in the evolution sequence. Hiner et al. (2012) measured the stellar velocity dispersion of 6 post-starburst quasars and the black hole mass from the broad line emission, and found that their locations on the $M_{\text{BH}} - \sigma$ relation and the Faber-Jackson relation suggests that their bulges might be dynamically peculiar. Sanmartim et al. (2013) and Sanmartim et al. (2014) obtained IFU spectra of the inner kpc region for two post-starburst quasars. For both objects, the old stellar population dominates the inner 250 pc while the starburst and post-starburst stellar populations dominate the region outside this central core. This result suggests that the starburst is triggered at the circumnuclear ring (~ 500 pc) following a major merger.

Another coherent picture that has emerged is the dichotomy of post-starburst quasars in early and late-type host galaxies. Cales et al. (2011) studied morphologies of 29 post-starburst quasars with high-resolution HST images. They found roughly equal number of host galaxies with elliptical or spiral morphologies, and roughly half of each type show sign of recent mergers. They also found that the AGNs in the elliptical hosts are significantly brighter than the ones in spiral hosts. Cales et al. (2013) modeled the optical spectra of 38 post-starburst quasars with stellar and AGN components. They found that the post-starburst quasars in elliptical hosts have brighter AGN luminosity, younger starburst age and emission line ratio diagnostics consistent with AGN.

Post-starburst quasars in spiral hosts, on the other hand, have fainter AGN, older starburst populations and line ratios consistent with star-formation. These findings suggest a picture that there are two mechanisms that trigger post-starburst quasars, where those in elliptical host galaxies are associated with major mergers, and those in spiral host galaxies are from milder events such as minor mergers or secular processes. Cales & Brotherton (2015) summed up the situation with a comprehensive study using all available HST imaging of post-starburst quasars, post-starburst galaxies and normal quasars. They found that the post-starburst quasars tend to have older stellar age than post-starburst galaxies. This conclusion led to a proposed picture that a major merger would first lead to a dusty starburst, observationally a ULIRG. Then once the dust is cleared, and the stellar population aged, this becomes a post-starburst galaxy. After time delays also of order 1 Gyr, the gas falls to the central supermassive black hole due to secular processes and lights up the AGN, making the object either a post-starburst quasar or a normal quasar, depending on how prominent the quasar light is compared to the stellar component, before everything fades and eventually becomes an elliptical galaxy.

Despite the recent interesting developments on this topic, most results are based on small sample of objects. The only systematic search of post-starburst quasars in the literature is by Brotherton et al. (2004) which found about 300 post-starburst quasars from the First Data Release of the Sloan Digital Sky Survey (SDSS DR1) and the Two Degree Field (2dF) Quasar Survey. This sample is relatively local, with the median redshift around $z \sim 0.25$. Now that the spectroscopic sample at higher redshift are available, the time is ripe to search for post-starburst quasars among them.

In this chapter, we tackle this very problem by systematically searching for post-starburst quasars in the SDSS/BOSS spectroscopic dataset. The resulting uniform sample can provide the first step toward statistical studies of this type of object and its role in galaxy evolution.

2 Post-starburst Quasar Selection

To explore the importance of post-starburst quasars in galaxy evolution studies, the first important step is to select a large number of these objects. In general, these objects have

spectroscopic signatures of both AGN and post-starburst stellar populations. An unambiguous spectroscopic sign of an unobscured AGN is the presence of broad line emission. The blue power-law continuum blueward of 4000\AA is another possible sign, but is more ambiguous because it can also be caused by younger stellar population. The post-starburst population, as previously, can be seen from strong Balmer series absorption, indicating population dominated by A-stars, and the lack of nebular line from HII regions, indicating the lack of ongoing star formation. However, some nebula emission lines, in particular the $\text{OII}\lambda 3727$, line can also be contributed by the central AGN (e.g. Yan et al. (2006)) and therefore any cuts on these lines should be avoided in order not to bias the sample.

In this section, we select post-starburst quasar samples from various SDSS sources using a variety of methods. The goal of this exercise is to explore the completeness and selection biases of different methods. The first method explored here searches for post-starburst quasars among our existing post-starburst galaxies from the DR12 using MgII line fitting to quantitatively measure the broad line. The second method starts with the existing SDSS DR12 QSO sample (Pâris et al. 2015; in prep) and searches for post-starburst stellar populations in the spectra. Finally, we performed a systematic search for post-starburst quasars from the whole SDSS-III BOSS DR12 spectroscopic dataset. We describe each of these approaches in the following sections.

2.1 Search for Post-starburst Quasars from the Post-starburst Galaxy Sample

This section describes the post-starburst quasar selection from our existing sample of post-starburst galaxies from the SDSS DR12. We develop a method to fit the MgII line that includes the velocity shift and linewidth as free parameters in order to quantify the broad line emission properly. Furthermore, since our method for fitting the MgII line can also be used to detect narrow absorption, we explore the outflow properties of post-starburst galaxies probed by MgII absorption as a by-product.

MgII Doublet Line Fitting Method

This section describes the method we used to fit the MgII doublet line profiles. The fit is done to the spectrum in the rest-frame wavelength range 2400-3200 Å. This wavelength range is chosen to be relatively large so that the pseudo-continuum level can be established even for the broadest broad line emission (with $\sigma \sim 5000$ km/s). We assumed the Gaussian line profile for each of the lines of the doublet, with the strength ratio between the two lines fixed at unity, which is a value expected theoretically for the optically thick case (Zhu et al., 2014). The two Gaussians also share the same velocity shifts and line widths. The pseudo-continuum level does not take the iron emission into account, and is simply assumed to be described by a linear function in wavelength. In total, the model assumed has five free parameters: normalization related to line strength, two parameters describing the continuum, the velocity shift and the line width in velocity units, and can be written by

$$f_{\text{MgII}}(\lambda) = A \left(\frac{1}{\sqrt{2\pi}\sigma_1} \exp \left[-\frac{1}{2} \left(\frac{\lambda - \lambda_1}{\sigma_1} \right)^2 \right] + \frac{1}{\sqrt{2\pi}\sigma_2} \exp \left[-\frac{1}{2} \left(\frac{\lambda - \lambda_2}{\sigma_2} \right)^2 \right] \right) + B\lambda + C, \quad (4.1)$$

where A is proportional to the line strength and $B\lambda + C$ is the pseudo-continuum level assumed to be linear in wavelength. The line centers and line widths in wavelength units $\lambda_{[1,2]}$ and $\sigma_{\lambda[1,2]}$ can be written in term of the rest-frame wavelengths of the doublet, systemic redshift (z), velocity shift with respect to the redshift (v), and velocity dispersion (σ) as

$$\lambda_{[1,2]} = [2796\text{\AA}, 2803\text{\AA}] \times \left(1 + \frac{v}{c} + z \right) \quad (4.2)$$

$$\sigma_{\lambda[1,2]} = [2796\text{\AA}, 2803\text{\AA}] \times (1 + z) \times \frac{\sigma}{c}, \quad (4.3)$$

where 1 and 2 subscripts correspond to the 2796Å and 2803Å components. As a potentially confusing terminology, we should make clear that the velocity dispersion σ is in units of velocity (km/s) while the related linewidth σ_λ has a unit of wavelength (Å).

In fitting the line profiles for these objects, it has been found that the normal minimization routine (IDL routine `CURVEFIT`, using the gradient-expansion algorithm, with per-pixel errors taken into account) is not always reliable. The results are sensitive to the initial guesses, and can converge on a local minimum, resulting in a clearly spurious values of velocity and linewidth. To solve this problem, we instead conduct a two-dimensional grid search on velocity-linewidth parameter space, and for each combination of v and σ do a linear fitting for the continuum and the line strength. This effectively reduces the problem to linear fitting for three free parameters at each combination of v and σ . The ranges of the $v - \sigma$ grid are between -2000 to 2000 km/s, and 100 to 5000 km/s respectively, with resolutions of 20 km/s in both quantities. These ranges are large enough to cover broad line AGN emission and relatively high velocity shifts. The overall best fit is then taken at the grid point where the linear fit gives the minimum value of χ^2 .

This fitting approach is applied to every object in our post-starburst galaxy catalog with redshift such that the range 2400-3200Å is covered in the spectrum. The five primary free parameters are found from the fit. The equivalent width of the MgII line is also calculated from these fit parameters.

The signal-to-noise ratio of the equivalent width is defined as the equivalent width divided by the error in equivalent width, which is calculated from the errors in fit parameters. In this definition, the signal-to-noise ratio can be either positive or negative, depending on whether the MgII is in absorption or emission respectively. The distribution of the signal-to-noise ratio of MgII EW of our post-starburst galaxy sample is shown in Figure 4.1.

By extensive visual inspection, we found that the objects with signal-to-noise ratio in equivalent width greater than about 5 (in both directions) always show clear, unambiguous emission or absorption in MgII line, while objects with signal-to-noise ratio lower than this can be ambiguous. Therefore, in the following sections we concentrate on only objects with signal-to-noise ratio $|S/N| > 5$.

It should be noted that the distribution of signal-to-noise ratio of MgII equivalent width is bimodal, and contains very few objects with signal-to-noise ratio close to zero. This seems counterintuitive at first since one expects that any measurement should have some objects at zero

signal-to-noise if their spectra is pure noise. We believe that this is a consequence of the way the equivalent width is calculated, where the errors in line flux and continuum level may combine in such a way that the signal-to-noise ratio can not take value of zero. However, we have not thoroughly investigated this issue and the Figure 4.1 should be interpreted cautiously.

It should also be noted that there are objects with broad MgII emission, with superposed narrow MgII absorption. Our fitting method does not take this possibility into account, since it only assumes one value of velocity shift and velocity dispersion. This is very interesting class of objects because the MgII emission is an indication of quasar activity, while MgII absorption is the outflow, which is driven by either AGN activity or starburst. Therefore objects that show both might give some direct insights into interaction between AGN activity and outflows. Identifying and modeling the MgII with both emission and absorption components will be the topic of a future study.

Post-starburst Quasar Sample

Once we obtain the MgII line profile for all post-starburst galaxies, we identified the post-starburst quasar subset as those objects with significant MgII broad line emission. Using the signal-to-noise ratio cut in MgII equivalent width as $S/N < -5$ (negative sign indicates emission) as described in the previous section, we construct a sample of 73 objects, all of which are visually confirmed to be fitted correctly. Figure 4.2 shows the linewidth distribution of the broad MgII emission, with the velocity dispersion spanning a wide range up to 5000 km/s with median value of about 2250 km/s.

MgII Absorption and Outflows

The other product of the detailed analysis on MgII line of our post-starburst galaxy sample is to study the narrow absorption that can be indicative of outflows from the galaxies. As in the last section, we made the signal-to-noise ratio cut in MgII equivalent width $S/N > 5$ for objects with clear detection of MgII. An additional cut $\sigma < 1500$ km/s is included to remove objects whose line

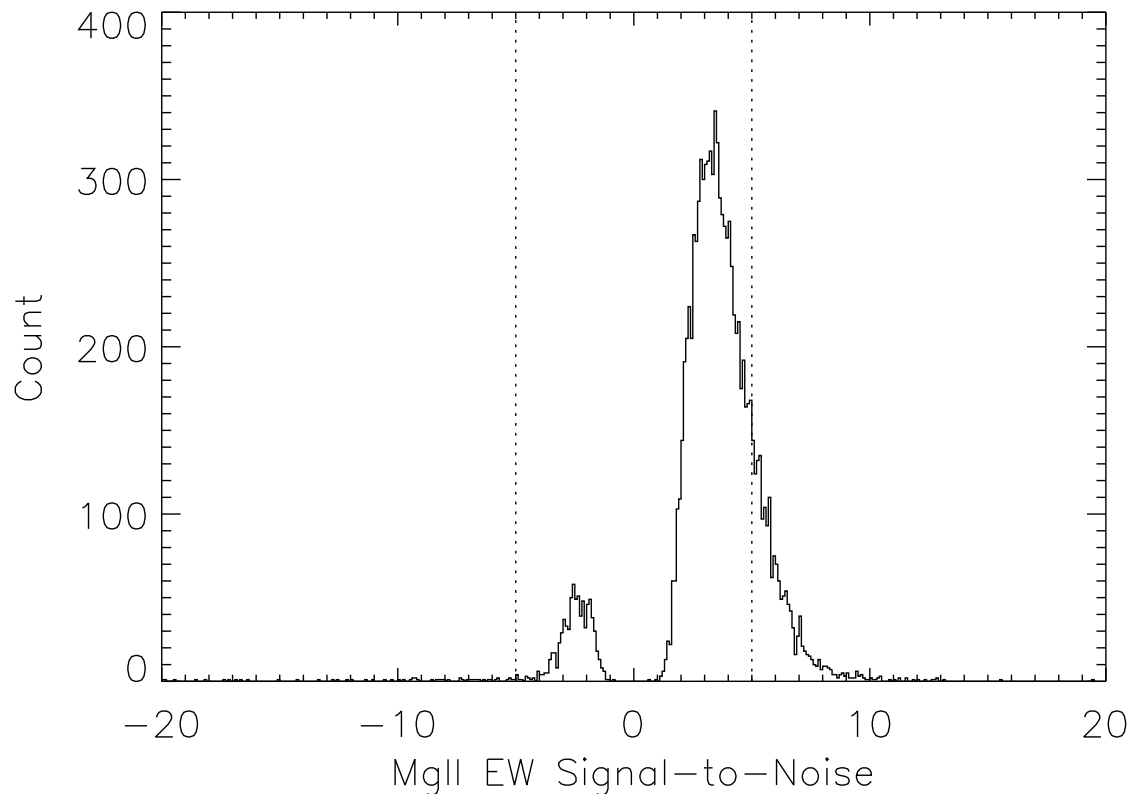


Figure 4.1 Distribution of signal-to-noise of MgII EW of our post-starburst galaxy sample. The signal-to-noise ratio, defined to be the value of signal-to-noise ratio divided by its error, can be either positive (for emission line) or negative (for absorption). The galaxies shown here are only those with the wavelength range $2400\text{--}3200 \text{ \AA}$ covered by the SDSS spectra, which excludes about 400 low-redshift objects from the parent sample. The vertical lines at 5 and -5 indicates the threshold values in signal-to-noise ratio that we found to correspond to clear detection of emission or absorption.

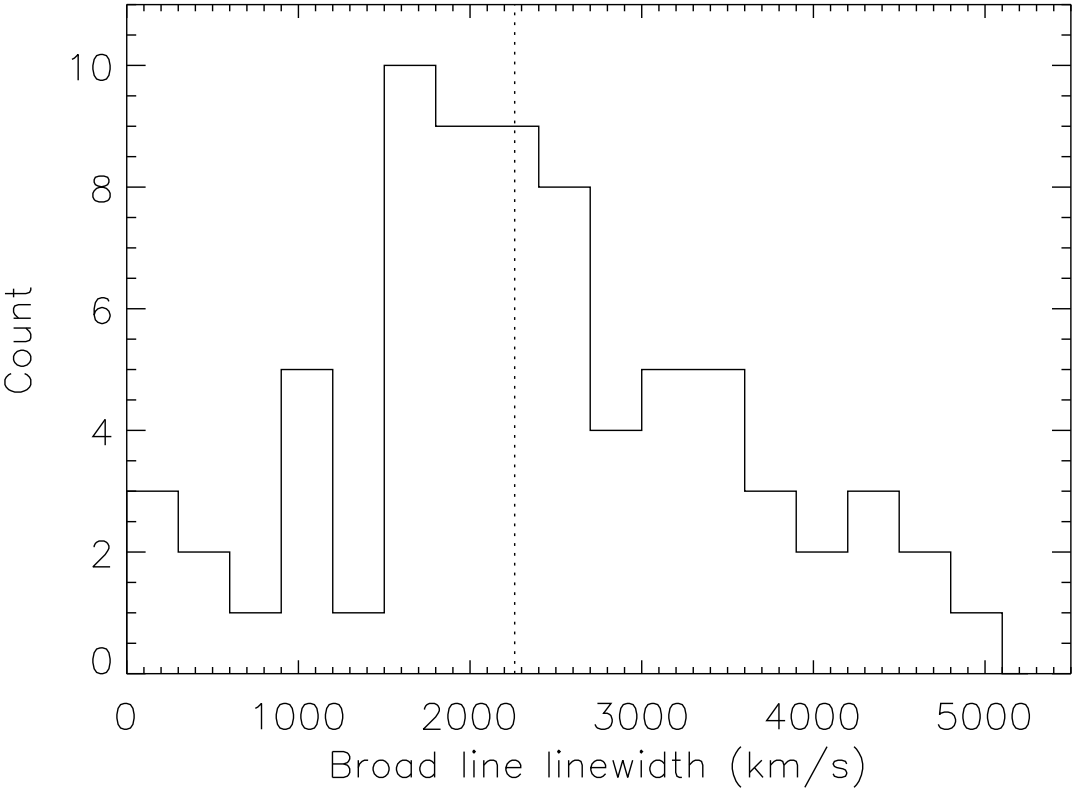


Figure 4.2 The MgII line width of post-starburst galaxies from our DR12 sample which are determined to have unambiguous broad line MgII emission ($S/N < -5$). The line widths are typically wide, with median value of about 2250 km/s.

fits are fit to the general continuum shape rather than the actual line itself. This results in 1242 objects. The distribution of the velocity shift of the MgII absorption line with respect to the systemic redshift is shown in Figure 4.3. The individual objects show a wide range of velocity shifts, filling the whole range of -2000 to 2000 km/s used for fitting the velocity. But on average, the MgII absorption tends to show a blueshift with respect to the systemic velocity, with 934 of these objects (75%) showing blueshifts. The median blueshift velocity is about -400 km/s, with the FWHM of the distribution about 1200 km/s. This trend that most post-starburst galaxies tend to have outflows confirms the general picture that feedback from star formation (which by now has become a post-starburst population) or the AGN activity in the central supermassive black hole drives the outflows. This range of outflow velocities of several hundreds to a few thousands km/s is consistent with what Tremonti et al. (2007) found for a small sample of post-starburst galaxies.

2.2 Search for Post-starburst Quasars from the SDSS Quasar Catalog

In the previous section, we searched for the objects in our post-starburst galaxy sample that show the spectroscopic signature. Another orthogonal approach is to search the SDSS Quasar Catalog to find its subset that show sign of post-starburst stellar population.

To recap, the post-starburst galaxy selection method involved fitting the “A” and “K” stellar population templates and continuum to the spectrum. The redshift output of the spectroscopic pipeline is trusted in the DR12 sample. Cuts are done on the importance of the A-star contribution to the spectrum, denoted by the A/Total ratio, and also on the equivalent widths of H δ and OII λ 3727 lines. All false-positives are then removed through visual inspection at the end.

To apply this method to the search for post-starburst quasars, it is modified in many important aspects to be more suitable and efficient. The first is that now the requirement on the OII λ 3727 equivalent width, which was placed for post-starburst galaxies to remove objects with ongoing star-formation, has now been removed because AGN can also contribute to this line in emission. The requirement on the H δ equivalent width remains the same (H δ EW>4.0), where positive sign corresponds to absorption. It should be noted that this criteria on the H δ EW can

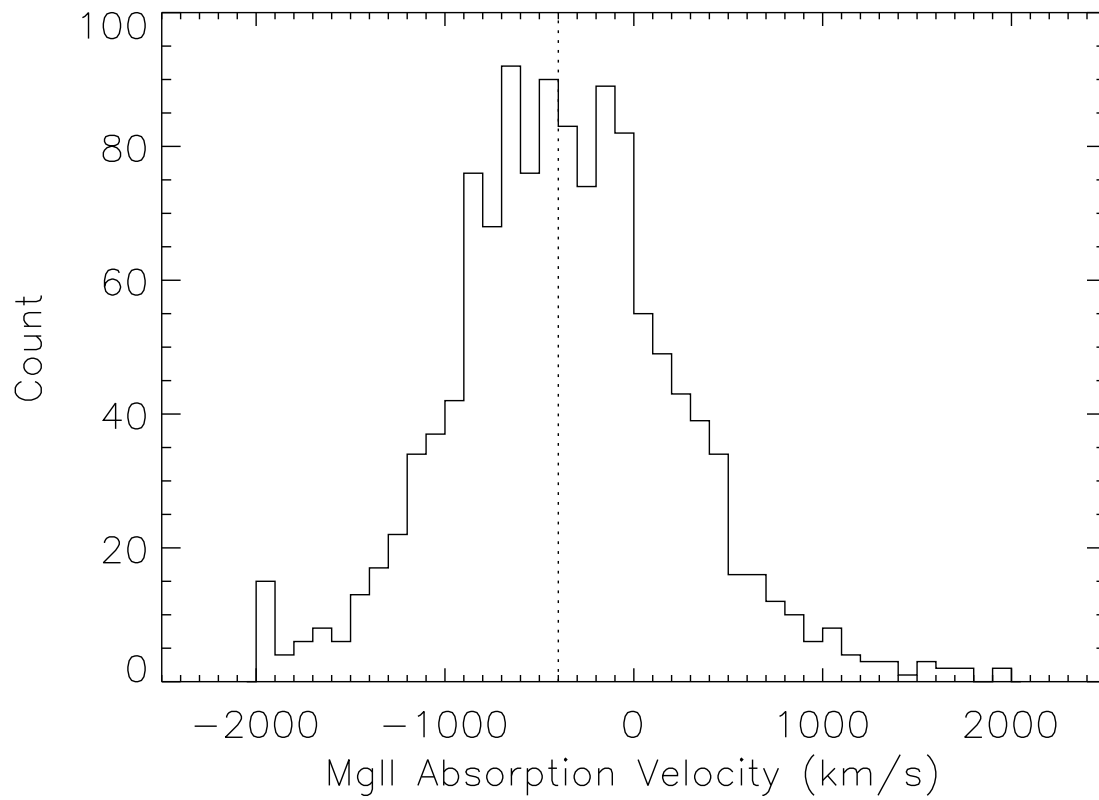


Figure 4.3 The distribution of MgII absorption velocity offset compared to the systemic redshift for objects with unambiguous detection of MgII absorption ($S/N < -5$, where negative sign denotes absorption.) These objects tend to show blueshifts, with median velocity offset at 400 km/s.

bias the final sample toward objects with stronger $H\delta$ absorption compared to the previous post-starburst galaxy selection. This is because the continuum is more dominant in post-starburst quasar spectrum, and therefore the same absorption in $H\delta$ flux will correspond to smaller equivalent width. Another change is that the significance of A-stars that was measured with A/Total ratio is now measured with the A/(K+A) ratio. This is because for normal post-starburst galaxies, the level of continuum is usually negligible, thus the two ratios are very similar. For post-starburst quasars, however, the continuum is largely contributed to by the AGN component, therefore the importance of A-star to total stellar component is better measured without continuum taken into account. The threshold value required for the A/(K+A) ratio is at 0.25 as was the case with the A/Total ratio previously.

This selection algorithm is applied to all spectra in the SDSS DR12 QSO catalog. Out of the 297301 quasars identified in the QSO catalog, 341 objects pass the requirements for the $H\delta$ equivalent width and the A/(K+A) ratio, and are visually inspected to confirm the candidate. The visual inspection process suffers from a fairly large false positive rate (objects identified as post-starburst quasar candidates by the automatic screening, but actually are not). For most of these objects, the reason is due to noisy values of A/(K+A) ratios. This is understandable because the spectra of these objects are dominated by the AGN component, making the contributions from both the A-component and K-component are close to zero and thus meaningless value of A/(K+A). During visual inspection, we also reject objects that do not show any sign of MgII emission, despite not having explicit requirements for this earlier, so that the post-starburst quasars selected here can be compared fairly to those selected from other sections. In the end, this results in the final sample of 213 objects, with redshift span from 0.28-1.36 with median redshift 0.77.

2.3 Search for Post-starburst Quasars from the SDSS-III BOSS Spectroscopic Database

Now that we have looked for the post-starburst quasars using two methods, one looking for the subset of post-starburst galaxies that show AGN, another looking for the subset of known AGNs

and searching for a post-starburst stellar population. It is reasonable to generalize these approaches and search the entire SDSS-III BOSS spectroscopic database in a way similar to that used to identify post-starburst galaxies in previous chapters.

The approach taken here is similar to the one used to look for post-starburst quasars in the SDSS Quasar Catalog. The K and A stellar spectral templates are fitted to all objects with spectra available and redshift such that the rest-frame 3600-4400 Å range is covered in the spectrum. To select the post-starburst quasar candidates, various parameter cuts are modified from the previous post-starburst galaxy selections in a similar manner as used in the previous section. To summarize, we require the A-star contribution to total stellar components to be $A/(K + A) > 0.25$ and the H δ equivalent width to be $H\delta EW > 4 \text{ \AA}$ in absorption. Again, it should be noted that the H δ absorption in post-starburst quasars needs to be stronger than post-starburst galaxies to pass this cut, because the post-starburst quasar spectra are more dominated by the continuum. There is no requirement on the OII λ 3727 equivalent width. An additional requirement for an object to be counted as a post-starburst quasar is the presence of strong MgII emission. For this we require the equivalent width of the MgII line to be $EW < -10 \text{ \AA}$ (negative sign denotes emission.) Also, a lower limit on the continuum level around MgII is placed to help reducing the amount of visual inspection required. This is because the low level of continuum level can drive the equivalent width to arbitrarily large values.

This selection algorithm is applied to all spectra in the SDSS-III BOSS spectroscopic sample (approximately 2.5×10^6 spectra), resulting in 4072 objects identified as post-starburst quasar candidates. These objects are then visually inspected to confirm that the fit is correct. The final sample contains 578 unique objects with redshift ranging between 0.34-1.34 and median redshift 0.67. The false positive rate (objects identified as candidates which are rejected at visual inspection) is large for a number of reasons. The main reason is that for objects whose spectra are dominated by AGN, with low contribution from the stellar components, the $A/(K+A)$ ratio is very noisy since both the A-component and K-component are close to zero. This is the same problem discussed in Section 2.2 where we searched for post-starburst quasars from the QSO catalog, but the false positive rate here is much higher. This is because there are a number of

quasars in redshift range $z \sim 0.6 - 1.0$ that are spectroscopically selected as galaxy, and are not included in the QSO catalog because they have redshift lower than 2.0. This issue is discussed in more detail in Section 3.

A sample of spectra of objects from this sample is shown in Figure 4.4. These spectra show the large diversity in the spectral energy distributions (SEDs) of post-starburst quasars, with some objects showing quasar-dominated spectra, but with significant post-starburst stellar components visible. Other objects, on the other hand, are dominated by stellar component, with small flux density blueward of 4000\AA , except for significant MgII line in broad emission. It should also be noted that the MgII line can show structure such as superimposed absorptions, sometimes blueshifted, indicative of outflows, or asymmetric line profiles.

3 Comparing Different Post-starburst Quasar Samples

In this section, we compare the three methods of selecting post-starburst quasars presented in the previous sections. To summarize, we selected post-starburst quasars from three different parent samples as follows:

1. From the post-starburst galaxies (73 objects)
2. From the SDSS Quasar Catalog (213 objects)
3. From the SDSS-III BOSS spectroscopic database (578 objects)

Figure 4.5 shows the redshift distribution of the post-starburst quasars in the three samples respectively. Each of these selections have somewhat different criteria, and therefore produce different final samples. Out of these, the smallest sample is the sample number (1) (selected from known post-starburst galaxies). This sample requires a lack of OII λ 3727 emission, and also uses the A/Total ratio to measure the contribution of the A-star component. These two criteria, which are relics of the post-starburst galaxy selection, together reject a large number of objects, leading to a small sample size. The requirement on OII line removes a large number of objects that have strong emission in this line, potentially due to the AGN instead of star formation. The criteria on

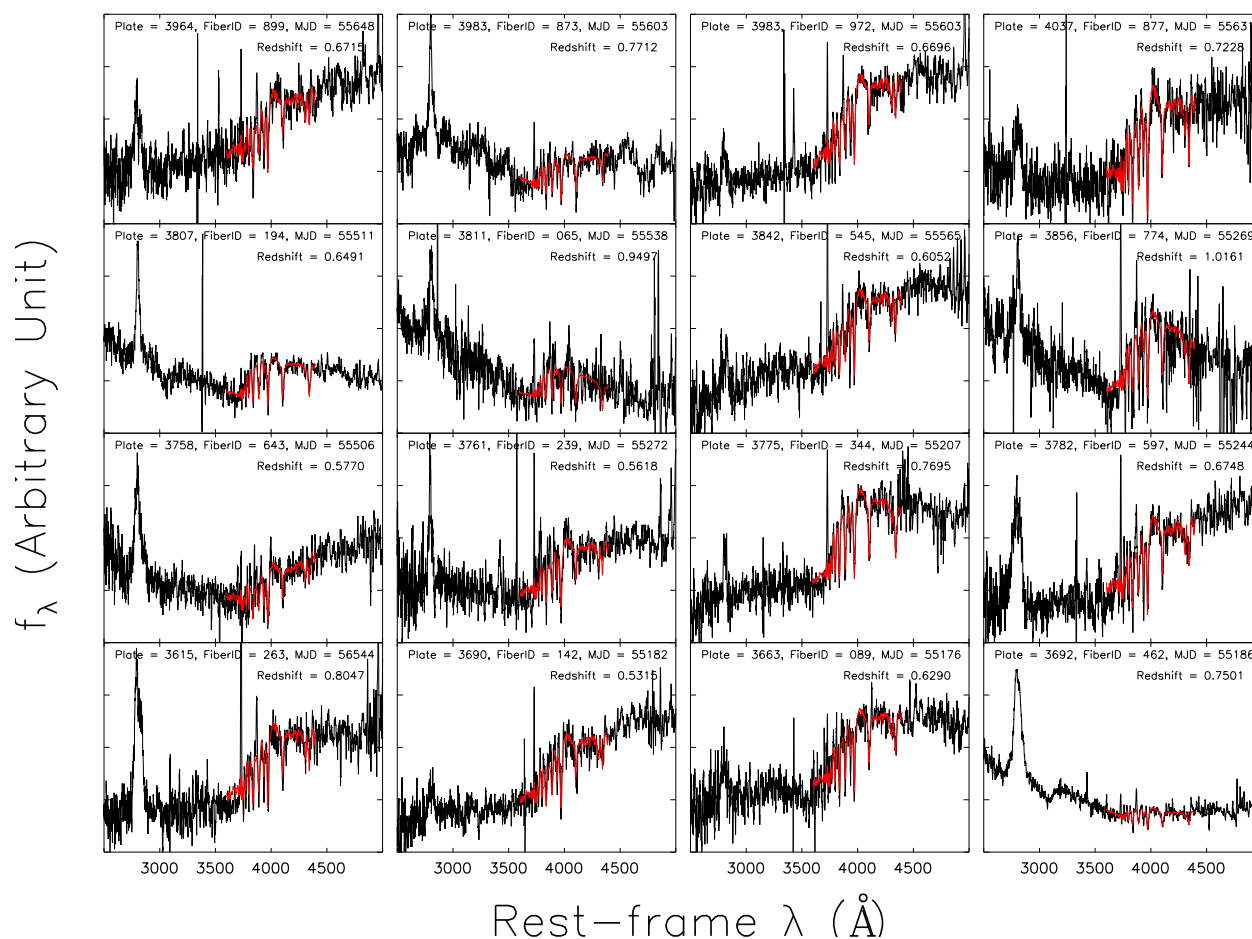


Figure 4.4 Example spectra of post-starburst quasars. The spectra of this class of objects show spectroscopic signatures of both post-starburst stellar population and broad line MgII emission. The red lines show the K+A template fit to the 3600-4400 \AA range, where the components used to fit the spectra are the “K”, “A”, and the quadratic continuum.

A/Total in the post-starburst quasar context, where the continuum is usually strong, also requires the A-star contribution to be unusually strong to meet the criteria, further excluding objects from this sample. In a sense, post-starburst quasars in this sample can be considered special, since they have stronger A-star components than the other two samples. The lack of OII emission also ensures that no ongoing star formation is present. It is unclear whether this lack of OII line means anything about the properties of AGN in these objects.

The sample number (2) (selected from known quasars) is more inclusive than the one selected from the known post-starburst galaxies, in large part because of the lack of OII criteria, and a less stringent requirement on the A-star strength (by using $A/(K+A)$ instead of A/Total). However, this sample still does not include everything in sample number (1) because many objects from the post-starburst galaxy sample are not selected or classified as quasars, and therefore never enters the SDSS Quasar Catalog.

The sample number (3) (selected from the whole SDSS-III BOSS spectroscopic database) is the largest as expected, since in theory it should encompass both the sample (1) and (2). In practice, there are about 50 objects that are present in either sample (1) or (2), but are missing from this sample. The main reasons for this is the requirement on continuum level around the MgII line. This requirement was applied in order to reduce the number of objects needed to be visually confirmed, since if the continuum level is low, the equivalent width can be arbitrarily high. Another reason that the sample (3) misses some objects in sample (2) is due to the requirement for reliable redshift ($Z_{\text{WARNING}}=0$), while some objects in the Quasar Catalog are all visually confirmed despite having non-zero Z_{WARNING} initially. Currently, these problems combined contribute to about 10% incompleteness rate for the post-starburst quasars. In principle, these incompleteness can be fixed by removing the requirement on the continuum flux level around MgII and the requirement for Z_{WARNING} , however this will come at a cost of significantly more visual inspection required.

Another important implication of this exercise is that by comparing the sample (2) and (3), we can assess the completeness of the SDSS DR12 Quasar Catalog (Pâris et al. 2015; in prep.) In particular, we found nearly 500 objects that are in sample (3) but not (2), which is puzzling

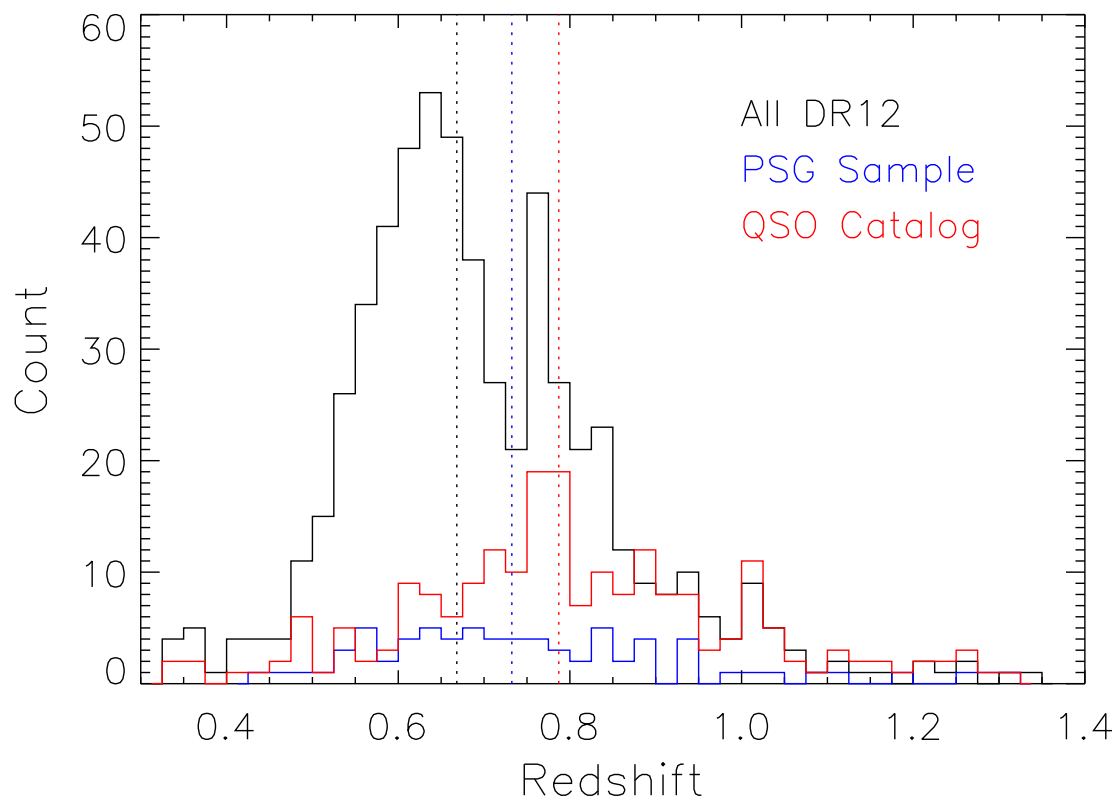


Figure 4.5 Redshift distributions of post-starburst quasars selected from three different samples: known post-starburst galaxies (blue), known quasars (red) and the entire SDSS-III BOSS spectroscopic sample (black). The dashed lines show the median redshifts of each sample respectively.

because these objects obviously have AGN activity from the broad MgII lines, and should therefore be in the Quasar Catalog, yet they are not. Figure 4.6 shows examples of objects in this category. The spectra of these objects have a wide variety of SED shapes, ranging those dominated by stellar spectra but with MgII emission. Given that their SEDs and broad-band colors are similar to normal galaxies, it is conceivable that these objects might be missed by the Quasar Catalog. The more surprising cases are those objects whose spectra are dominated by AGN light, with blue continuum and strong broad line emission, with stellar component visible.

We investigated the reasons why these objects, despite being post-starburst quasars, are not in the QSO Catalog. We found that a large fraction of these objects are spectroscopically selected and classified as galaxies, which naturally explains this. Some objects are selected as galaxies, and classified by the pipeline as QSO at the correct redshift. These objects are not included in the DR12 QSO Catalog because the catalog is designed to visually inspect objects with QSO classification only if they have redshift $z > 2.0$, which is set to select objects that can be used for BAO analysis with Lyman- α forest. The rest of these objects are selected by QSO target selection flags, and classified as QSO by the pipeline, but apparently was determined at the visual inspection step as objects with unsecured redshift identifications, thus excluded from the final QSO Catalog. These objects are in the “superset” catalog, which contains every object that has been visually inspected.

4 SDSS J125942.80+121312.5: A Quasar with Strange Spectroscopic Properties

In this section, we digress to take note of an object with extremely peculiar spectroscopic properties, which we founded serendipitously while searching for post-starburst quasars from the SDSS DR12 QSO Catalog. This object passed the automatic fitting algorithm, and subsequently got visually inspected and rejected from the final post-starburst quasar sample. However, its spectrum is peculiar enough that it is worth being mentioned here.

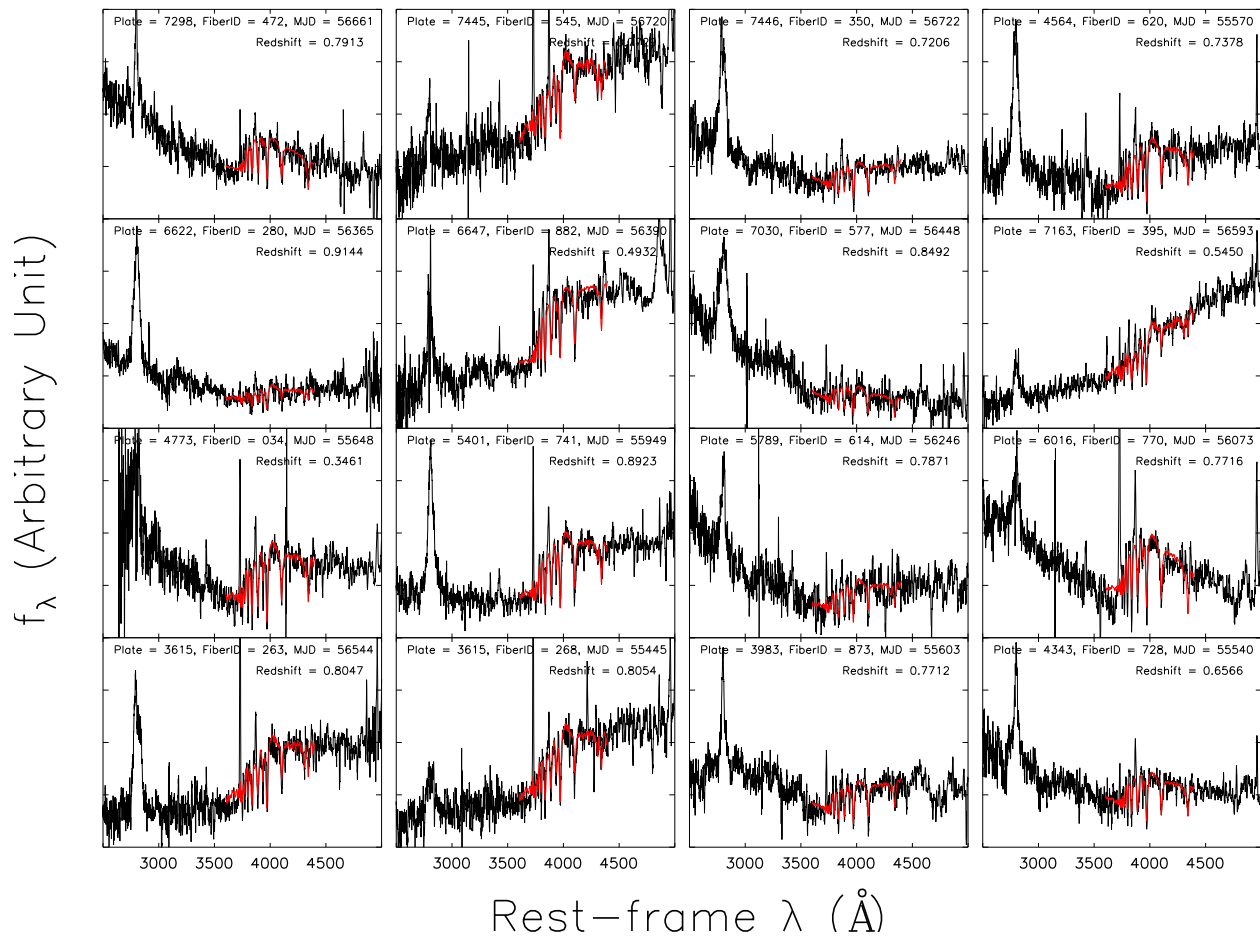


Figure 4.6 Example of spectra of post-starburst galaxies that are identified in the SDSS-III BOSS DR12 spectroscopic data (sample 3), but not in the SDSS DR12 Quasar Catalog (sample 2.) The red lines show the K+A template fit to the 3600-4400Å range, where the components used to fit the spectra are the “K”, “A”, and the quadratic continuum. The SEDs have a wide variety from those dominated by AGN light to those dominated by stellar light.

SDSS J1259+1213 (RA=194.92834, DEC=12.22017) was observed twice by the SDSS, first in the SDSS-I/II (Plate=1695, FiberID=75, MJD=53473), and subsequently as part of the BOSS program in SDSS-III (Plate=5419, FiberID=618 and MJD=55983). The SDSS spectroscopic pipeline measured its redshift to be $z = 0.7473$ and $z = 0.7298$ for both observations respectively. The slight difference is due to whether the redshift is centered on the emission or absorption components of the P-Cygni line profile, which we will discuss later. We adopt the fiducial redshift value of $z = 0.7298$ which agrees well with Balmer series absorption.

SDSS J1259+1213 was first selected into the spectroscopic target as a color-selected quasar candidate with detection in radio (target selection flags QSO_CAP and QSO_FIRST_CAP). It was then determined to be a Broad Absorption Line (BAL) quasar (Gibson et al., 2009) and observed again in BOSS under the ancillary program VARBAL, which was designed to obtain repeated observation to study BAL variability. This BOSS spectrum is part of the SDSS DR12 QSO Catalog, which led to this discovery. The rest-frame optical spectra of this object from both observations, taken nearly seven years apart, are shown in the top two panels of Figure 4.7.

SDSS J1259+1213 was noticed and reported by Hall (2007) and in the SDSS DR5 QSO Catalog (Schneider et al., 2007) as an unusual FeLoBAL (BAL with low-ionization and iron emission lines), based on the spectrum from the first epoch alone. This object was one of only four objects that had been found by then to have Balmer series in broad absorption, and was speculated to represent a rare physical conditions where thick ionize HI is present and Ly α trapping leads to a significant amount of $n = 2$ hydrogen population responsible for Balmer absorption.

SDSS J1259+1213 clearly shows P-Cygni line profiles in Hydrogen Balmer series, where the emission is accompanied by blueshifted absorption. This line profile is usually associated with winds, outflows, or expanding envelope in stellar spectroscopy. However, it should be noted that in stellar spectroscopy, the P-Cygni profiles usually have strong emission, accompanied by weak, blueshifted absorption. In this case, on the other hand, the P-Cygni profiles in hydrogen Balmer series is dominated by absorption, except for the H β line which arguably have equally strong emission and absorption.

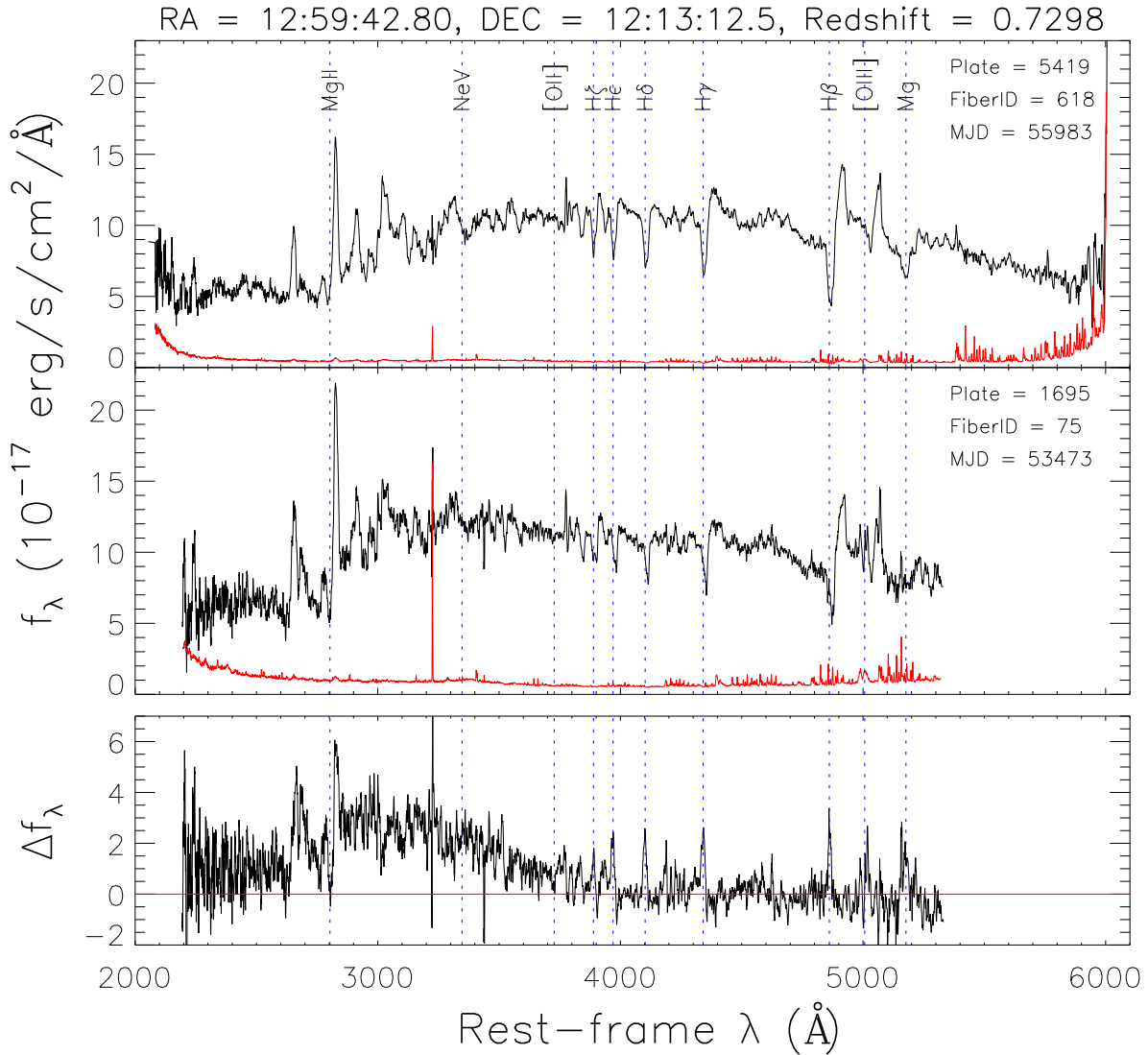


Figure 4.7 Top two panels: The rest-frame optical spectra of SDSS J125942.80+121312.5 from the SDSS-III BOSS observation (Plate=5419, FiberID=618, MJD=55983), and the SDSS-I/II observation (Plate=1695, FiberID=75, MJD=53473) respectively. The BOSS pipeline measured the redshift of this object to be $z = 0.7298$, agreeing with absorptions in Balmer series. The red lines show per-pixel errors. The spectrum is boxcar-smoothed with the box size 5 pixels to improve visibility. Bottom panel: the difference between the SDSS-I/II spectrum and the SDSS-III BOSS spectrum in the overlapping region. The red horizontal line shows zero level as a reference. The vertical blue dotted lines show the expected wavelengths of key spectral features in all three panels.

The MgII λ 2803 line shows prominent narrow emission slightly redshifted from the systemic redshift derived from the Balmer absorption. It is also conceivable that MgII line might have similar P-Cygni line profile to the hydrogen Balmer lines, with the small but visible absorption component exactly agreeing with those of Balmer absorption. The [OIII] λ 5007 line also shows similar P-Cygni profile. However, on closer inspection it seems that the wavelength of both the absorption and emission components of this line is redder than the expected position based on the redshift measured from Balmer absorption.

Other spectral features includes the strong absorption in Mg λ 5177 and some features that might be related to NeV λ 3347. There is no clear absorption or emission associated with the [OII] λ 3727 line. There are also unidentified narrow emissions (not coincides with anything in the line list used by the SDSS pipeline) at approximately 2650Å, 2910Å, 3030Å and less significantly at approximately 2240Å.

The spectral changes between the first observation (SDSS-I/II) and the second observation (SDSS-III) BOSS observations, taken nearly seven years apart, are also shown in Figure 4.7. The continuum shape redward of 4000Å does not change between the two observations. In contrast, the continuum level blueward of 4000Å drops from the first to the second observation, and the change peaks at about 3000Å. The first observation has stronger emission in MgII and unidentified features at 2240Å and 2650Å, and shallower Balmer series absorptions, than the second observation, as indicated by the peaks in the difference between the two spectra. Moreover, the line profile of the unidentified feature at 2650Å changes significantly between the two observations, with the red wing present in the former absent in the latter.

We investigated potential biases that could compromise the data quality and explain the strange SED shape of SDSS J1259+1213, and conclude that this object is likely genuine. First, the ZWARNING flag of this object is non-zero, and set to NEGATIVE_EMISSION. This is understandable because this flag is set on QSO spectra with, among other lines, H β in absorption, and so is triggered for this object naturally. After all, it is evident from many lines that the redshift of this object is identified correctly. We also checked spectra from the neighboring fibers, because if they are extremely bright, light can spill across the CCD causing the SED shape to be distorted. This

is also not the case. Finally, the per-pixel errors, also shown in Figure 4.7, are much smaller than the spectrum itself for most of the wavelength range. We therefore conclude that, with such high signal-to-noise ratio of the spectrum, the peculiar properties of this object is likely genuine.

As for the true physical nature of this object, we speculate that it might be a special phase in evolution of BAL quasar, when the absorption starts to occur, thus the P-Cygni line profiles, but before the absorption becomes too prominent and saturated as is the case in normal BAL quasars. However, this picture does not explain a number of spectral features such as the lack of power-law continuum, the lack of prominent broad-line emissions, and some unidentified narrow emission lines. More works, in term of both data and modeling, are warranted to study this object further.

There are many possible future directions that will be useful for unveiling the true nature of this object. The first is to obtain the spectrum in other wavelengths such as UV and Near-IR, which will allow access to other lines not covered in the optical spectrum such as Ly α , CIV or H α . Repeated spectroscopic observations will also be useful, since they can shed light on the evolution. Finally, it might be possible to search for other objects similar to this from the SDSS spectroscopic database. Bigger sample will allow for statistical statements to be made, and also to put limit on the rarity of this class of objects.

5 Discussions and Conclusions

In this chapter we explored different ways to select post-starburst quasars using the spectroscopic dataset from the Twelfth Data Release of the Sloan Digital Sky Survey (SDSS DR12). The post-starburst quasars are selected from different parent samples: the post-starburst galaxy sample presented in the previous chapter, the SDSS QSO sample and the entire SDSS-III BOSS dataset itself. The post-starburst quasar sample that is selected from the BOSS dataset is the most complete one and encompasses the other two samples, as expected. The post-starburst quasar samples selected from either our previous post-starburst galaxy sample or the SDSS QSO sample are significantly smaller in number due to various selection effects that were applied to the parent samples. We therefore call the post-starburst quasar sample selected from the BOSS dataset the “final” post-starburst quasar sample.

This sample contains 578 objects. The redshifts of objects in this sample range from $z = 0.34 - 1.34$ with median redshift $z_{\text{median}} \sim 0.67$. All objects are confirmed visually that the identifications and redshifts are correct. As such, this sample is the largest sample of post-starburst quasars in the literature.

It should be noted that our post-starburst quasar search presented in this chapter only uses the SDSS-III BOSS spectroscopic dataset, but does not cover the SDSS-I/II spectroscopic dataset. We can estimate the number of extra post-starburst quasars we would find if this portion of the spectroscopic dataset is taken into account from the post-starburst quasar sample Brotherton et al. (2004). Out of about 200 post-starburst quasars in this sample (from SDSS DR1), about 20 have redshift larger than $z \sim 0.35$, which allows the MgII λ 2803 line to be clearly seen in the early SDSS spectral coverage, and meets our sample requirement that broad line MgII is seen. The spectroscopic sample of SDSS had grown by a factor of 10 from DR1 to DR7, where the SDSS-I/II phase ended, thus we expect about 200 extra objects. The search for post-starburst quasars using the SDSS-I/II phase spectroscopic data will be the topic of future research.

An obvious extension to our post-starburst quasar study is to search for low-redshift objects, whose MgII emission is out of the wavelength coverage. In this case an object could be classified to be post-starburst quasar based on the H α broad line emission instead. Brotherton et al. (2004) did this to SDSS DR1 and found almost 200 objects in this redshift range. We expect to find a significantly larger sample due to the growth in the spectroscopic database size in the meantime. This sample would be valuable for studying redshift evolution of the post-starburst quasars, and will be a topic of future work.

Bibliography

- Brotherton, M., Diamond-Stanic, A., vanden Berk, D., Burton, R., & Croom, S. 2004, in
Astronomical Society of the Pacific Conference Series, Vol. 311, AGN Physics with the Sloan
Digital Sky Survey, ed. G. T. Richards & P. B. Hall, 285
- Brotherton, M. S., Grabelsky, M., Canalizo, G., van Breugel, W., Filippenko, A. V., Croom, S.,

- Boyle, B., & Shanks, T. 2002, *PASP*, 114, 593
- Brotherton, M. S., van Breugel, W., Stanford, S. A., Smith, R. J., Boyle, B. J., Miller, L., Shanks, T., Croom, S. M., & Filippenko, A. V. 1999, *ApJ*, 520, L87
- Cales, S. L. & Brotherton, M. S. 2015, *MNRAS*, 449, 2374
- Cales, S. L., Brotherton, M. S., Shang, Z., Bennert, V. N., Canalizo, G., Stoll, R., Ganguly, R., Vanden Berk, D., Paul, C., & Diamond-Stanic, A. 2011, *ApJ*, 741, 106
- Cales, S. L., Brotherton, M. S., Shang, Z., Runnoe, J. C., DiPompeo, M. A., Bennert, V. N., Canalizo, G., Hiner, K. D., Stoll, R., Ganguly, R., & Diamond-Stanic, A. 2013, *ApJ*, 762, 90
- Canalizo, G., Stockton, A., Brotherton, M. S., & van Breugel, W. 2000, *AJ*, 119, 59
- Cen, R. 2012, *ApJ*, 755, 28
- Gibson, R. R., Jiang, L., Brandt, W. N., Hall, P. B., Shen, Y., Wu, J., Anderson, S. F., Schneider, D. P., Vanden Berk, D., Gallagher, S. C., Fan, X., & York, D. G. 2009, *ApJ*, 692, 758
- Hall, P. B. 2007, *AJ*, 133, 1271
- Hiner, K. D., Canalizo, G., Wold, M., Brotherton, M. S., & Cales, S. L. 2012, *ApJ*, 756, 162
- Sanmartim, D., Storchi-Bergmann, T., & Brotherton, M. S. 2013, *MNRAS*, 428, 867
- Sanmartim, D., Storchi-Bergmann, T., & Brotherton, M. S. 2014, *MNRAS*, 443, 584
- Schneider, D. P., Hall, P. B., Richards, G. T., Strauss, M. A., Vanden Berk, D. E., Anderson, S. F., Brandt, W. N., Fan, X., Jester, S., Gray, J., Gunn, J. E., SubbaRao, M. U., Thakar, A. R., Stoughton, C., Szalay, A. S., Yanny, B., York, D. G., Bahcall, N. A., Barentine, J., Blanton, M. R., Brewington, H., Brinkmann, J., Brunner, R. J., Castander, F. J., Csabai, I., Frieman, J. A., Fukugita, M., Harvanek, M., Hogg, D. W., Ivezić, Ž., Kent, S. M., Kleinman, S. J., Knapp, G. R., Kron, R. G., Krzesiński, J., Long, D. C., Lupton, R. H., Nitta, A., Pier, J. R., Saxe, D. H., Shen, Y., Snedden, S. A., Weinberg, D. H., & Wu, J. 2007, *AJ*, 134, 102
- Tremonti, C. A., Moustakas, J., & Diamond-Stanic, A. M. 2007, *ApJ*, 663, L77

Wei, P., Shang, Z., Brotherton, M. S., Cales, S. L., Hines, D. C., Dale, D. A., Ganguly, R., & Canalizo, G. 2013, *ApJ*, 772, 28

Yan, R., Newman, J. A., Faber, S. M., Konidaris, N., Koo, D., & Davis, M. 2006, *ApJ*, 648, 281

Zhu, G., Ménard, B., Bizyaev, D., Brewington, H., Ebelke, G., Ho, S., Kinemuchi, K., Malanushenko, V., Malanushenko, E., Marchante, M., More, S., Oravetz, D., Pan, K., Petitjean, P., & Simmons, A. 2014, *MNRAS*, 439, 3139

Clustering Analysis of Post-starburst Galaxies

1 Introduction

The primordial density perturbations of the universe are believed to be from quantum fluctuations that are inflated to cosmological scales by inflation, which is then imprinted on the Cosmic Microwave Background (CMB) at the epoch of recombination. Studies of these fluctuations in the CMB have been very successful and have provided a cornerstone to cosmological studies (e.g. Spergel et al. (2003); Hinshaw et al. (2013); Planck Collaboration et al. (2014, 2015)). At later times, these primordial fluctuations grow further under self-gravity and form dark matter halos, providing sites into which baryonic matter will fall and form galaxies.

It was realized early on that the galaxy distribution does not necessarily follow the underlying dark matter distribution (Kaiser, 1984; Davis et al., 1985), in other words, galaxies are “biased” tracers of dark matter halos. The offset of the baryon distribution from that of dark matter is a result of baryonic physics that dictates the galaxy formation. It was shown by Bardeen et al. (1986) that the biases are consistent with the scenario in which galaxies form at the peaks of the density distribution, which are more clustered than the overall dark matter distribution. It was also shown that the bias is a function of dark matter halo mass and the epoch of galaxy formation (Mo & White, 1996). Therefore, by measuring the clustering properties of a given galaxy population, one can infer statistically the mass of the dark matter halos this galaxy population resides in.

On large scale, clustering can be used to constrain the cosmological parameters themselves through the measurement of Baryon Acoustic Oscillation (BAO). This is the acoustic wave in the coupled baryon-photon fluid before recombination, which freezes at the sound horizon at

recombination when the baryons become neutral and uncoupled from photons, leading to an enhanced number of galaxy pairs at distance ~ 150 Mpc. This extra clustering signal at 150 Mpc can be measured at different redshifts and used as a standard ruler (e.g. Eisenstein et al. (1998b,a); Glazebrook & Blake (2005); Sánchez et al. (2008)). On smaller scales, clustering analyses can constrain the formation and merger history of dark matter halos using, for example, the quasar population (Myers et al., 2007).

The Baryon Oscillation Spectroscopic Survey (BOSS) is a component of the SDSS-III survey aiming at accurately measuring the BAO. Three populations are spectroscopically observed over a large area of the sky (~ 10000 deg²) to measure BAO at different redshift ranges. The LOWZ and CMASS galaxy samples are selected to be massive early-type galaxies over the redshift range $0.2 < z < 0.4$ and $0.4 < z < 0.7$ respectively (e.g. White et al. (2011); Nuza et al. (2013)), and are extensions to the SDSS LRG sample in earlier SDSS phase at lower redshifts (Eisenstein et al., 2001; Tegmark et al., 2006). The third population is high-redshift active galactic nuclei, which serve as background light sources for Lyman- α absorption from the neutral hydrogen in the line-of-sight (Lyman- α forest), which can be used to probe BAO at larger redshift (e.g. Slosar et al. (2011); Delubac et al. (2015)). Thanks to large, statistical samples provided by large galaxy redshift surveys like SDSS, accurate measurements allow important discoveries such as color and luminosity dependence of the correlation functions, and the departure of the usually-assumed power law correlation functions (Zehavi et al., 2004, 2011).

In this chapter, we study the clustering properties of post-starburst galaxies by cross-correlating them with the SDSS CMASS galaxy sample. The post-starburst galaxy sample and the CMASS galaxy sample are described in section 2. Section 3 describes the method used to calculate the redshift-space correlation function and the semi-projected correlation function. A crude redshift evolution study of clustering properties is described in section 4. The clustering bias of the post-starburst galaxy sample, and the implication of the dark matter halo mass they reside, are discussed in section 5. Finally, we discuss the results and present conclusions in section 6.

2 Sample

The post-starburst galaxy sample used in the clustering analysis is selected from the Twelfth Data Release of the Sloan Digital Sky Survey (SDSS DR12) which is presented in Chapter 3 of this thesis. To limit the sample to the objects with uniform selection, we only use the objects that are selected into the spectroscopic sample via the CMASS criteria. This yields the final number of post-starburst galaxies used in this clustering analysis to be 9155 objects, with median redshift of $z_{\text{median}} \sim 0.62$. The normalized redshift distribution of this galaxy sample is shown in Figure 5.1. It should be noted that, even though the sample of more than 9000 post-starburst galaxies is considered quite large for galaxy evolution studies, this sample spreading over the 10000 deg² SDSS footprint is very sparse and is not suitable for clustering analysis on its own. This leads us to perform cross-correlation between this sample and the full CMASS galaxy sample which is much denser.

The CMASS galaxy sample we use is also from the SDSS DR12. This galaxy sample was selected spectroscopically for the primary purpose of doing BAO analysis. The color selection for this sample is designed to select massive early-type galaxies in the redshift range $0.4 < z < 0.7$ with stellar mass nearly complete above $M_{\star} > 10^{11} M_{\odot}$. The details on the selection can be found in B. Reid et al. (2015; in prep.) In total, there are 836347 CMASS galaxies over an effective area of 9376 deg², which is the same area as our post-starburst galaxy sample. The median redshift of this sample is $z_{\text{median}} \sim 0.52$, and the normalized redshift distribution of this sample is shown in Figure 5.1.

Another sample important for the clustering analysis is the CMASS random catalog, which is a mock sample generated with the same angular and redshift distributions as the real CMASS galaxy sample, but with no clustering signal. The size of this sample is about 50 times the CMASS sample, and it is used to correct for any systematic effects caused by variation in depth, completeness or observational conditions in the CMASS sample. The detailed method on the generation of the CMASS random catalog are described in B. Reid et al. (2015: in prep.)

In the following cross-correlation function calculations, the error bars are always estimated using the Jackknife resampling technique. This is done by dividing the sample into 10 contiguous

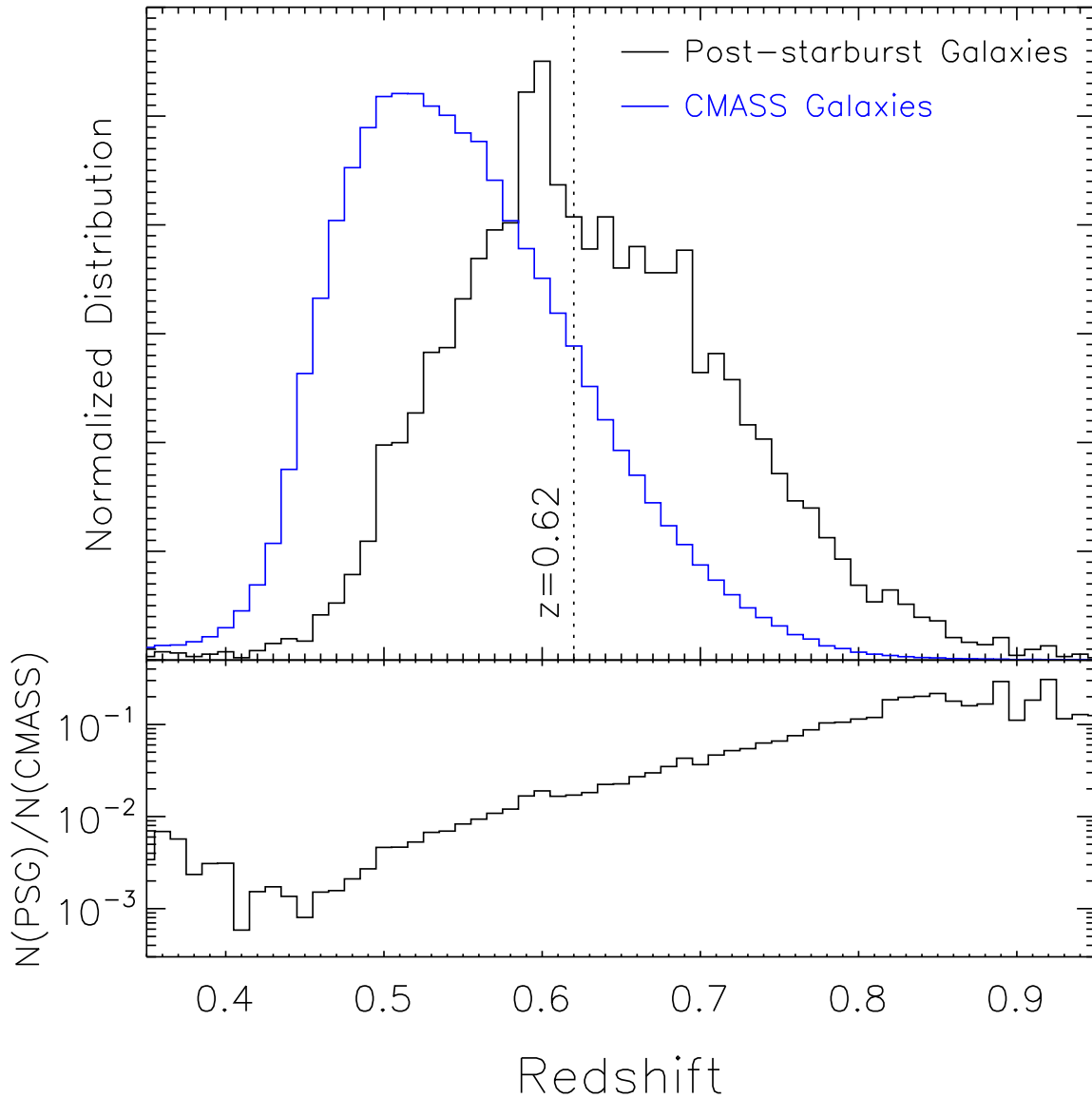


Figure 5.1 Top panel: Normalized redshift distributions of the CMASS-selected post-starburst galaxy sample (black) compared to that of the parent CMASS sample (blue). The two distributions are normalized to the total number of objects in the respective sample, so the total areas under the curves are the same. The dotted vertical line is at redshift $z = 0.62$ which roughly split the post-starburst sample in half. This value is used to split the clustering analysis into two redshift bins. Bottom panel: Ratio between the number of CMASS-selected post-starburst galaxy sample to the parent CMASS sample as a function of redshift.

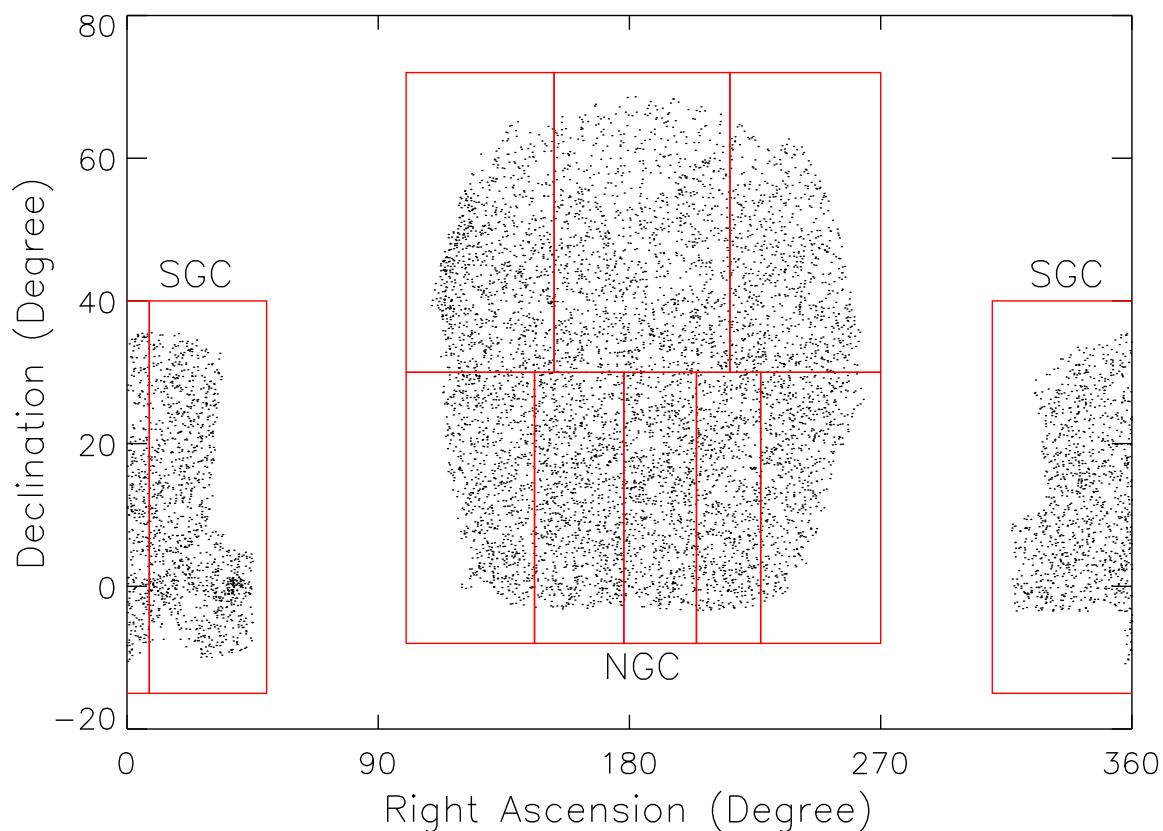


Figure 5.2 This plot shows how the SDSS footprint is divided into 10 parts for the purpose of using Jackknife resampling to estimate error bars. The black dots show the distribution of the CMASS-selected post-starburst galaxy sample. The Northern Galactic Cap region (NGC) is divided into 8 parts, while the Southern Galactic Cap region (SGC) is divided into 2 parts. Note that one part in the SGC region straddles the boundary of the plot.

parts on the sky, and sequentially removing each part from from the calculations. Figure 5.2 shows the way the SDSS footprint is divided into 10 parts. The division is such that each area contains roughly the same number of objects, but is otherwise arbitrary. Each of the two areas in the Southern Galactic Cap contains about 30% more objects than the areas in the Northern Galactic Cap region.

3 Cross-correlation Function

3.1 Redshift-space Cross-correlation Function

The redshift-space cross-correlation function between the post-starburst galaxies and the CMASS galaxies is calculated using the estimator

$$\xi(s) = \frac{DD(s)}{DR(s)} \frac{N_{\text{random}}}{N_{\text{CMASS}}} - 1, \quad (5.1)$$

following Davis & Peebles (1983); Mountrichas et al. (2009); Shen et al. (2013), where N_{CMASS} and N_{random} are the number of objects in the CMASS and random catalogues respectively. $DD(s)$ and $DR(s)$ are the post-starburst galaxy – CMASS galaxy pairs, and post-starburst galaxy – random object pairs counted at redshift-space separation s respectively. We calculate the cross-correlation function using 20 bins in logarithmic distance, in the range $s = 0.5 - 100 h^{-1}\text{Mpc} \sim 0.71 - 142 \text{ Mpc}$ with logarithmic spacing $\Delta \log s = 0.12 \text{ Mpc}$.

Figure 5.3 shows the cross-correlation function between post-starburst galaxies and the CMASS galaxy sample. The error bars are estimated using Jackknife resampling. The correlation between these two samples can be well-detected out to 100 Mpc. We fit a power-law of the form $\xi(s) = (s/s_0)^{-\gamma}$ to the correlation function and found the best-fit parameters to be $s_0 \sim 11.2 \pm 0.4 \text{ Mpc}$ and $\gamma \sim 1.60 \pm 0.04$.

3.2 Semi-projected Cross-correlation Function

We calculated the two-dimensional and semi-projected cross-correlation functions between the post-starburst and the CMASS samples as follows. If the redshift-space distances to two objects are s_1 and s_2 , and θ is the angular distance between them, the perpendicular and line-of-sight distance r_p and π are defined as

$$\pi = |s_2 - s_1| \quad (5.2)$$

$$r_p = \frac{1}{2}(s_2 + s_1)\theta \quad (5.3)$$

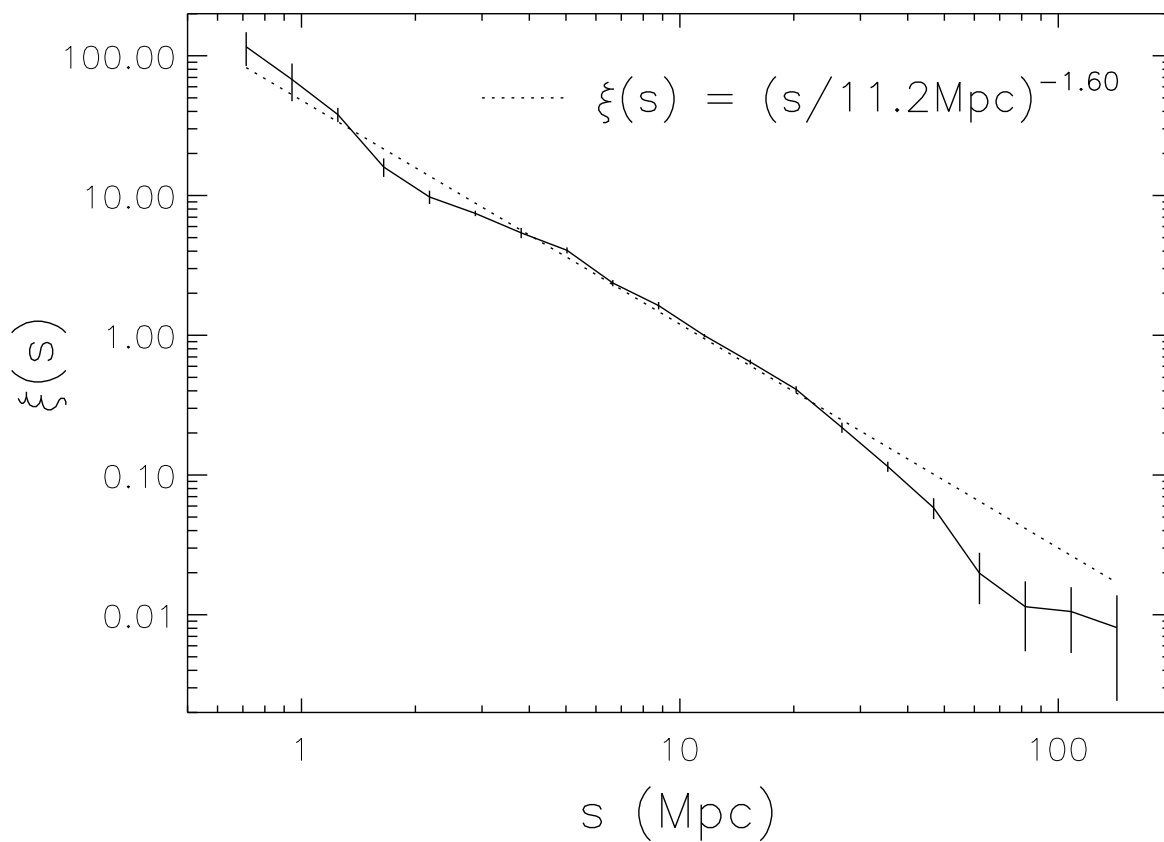


Figure 5.3 Redshift-space cross-correlation function between the CMASS-selected post-starburst galaxies and the CMASS galaxy sample. The dotted line shows the power-law fit of the form $\xi(s) = (s/s_0)^{-\gamma}$, with the best-fit parameters to be $s_0 \sim 11.2 \pm 0.4$ Mpc and $\gamma \sim 1.60 \pm 0.04$.

The two-dimensional cross-correlation function $\xi(r_p, \pi)$ is calculated from pair counting with the same Davis & Peebles (1983) estimator described in the previous section. The small angle approximation is valid in this case since the typical pairs separated by ~ 100 Mpc are never more than 5° apart at the typical CMASS redshift of $z \sim 0.5$. In calculating $\xi(r_p, \pi)$, the parameters r_p and π are binned in two different ways: linear binning between $0 - 70$ Mpc with step size $\Delta\pi = \Delta r_p = 0.5$ Mpc, and logarithmic binning in the range $0.5 - 100 h^{-1}$ Mpc with $\Delta \log r_p = \Delta \log \pi = 0.12$. The linear binning is used for the two-dimensional contour of $\xi(r_p, \pi)$ (Figure 5.4), while the logarithmic binning is used to calculate the projected correlation function in all subsequent figures (Figure 5.5, 5.7 and 5.8.) We have verified that the projected correlation function calculated with the linear binning agrees perfectly with that calculated with logarithmic binning. Figure 5.4 shows the two-dimensional cross-correlation function $\xi(r_p, \pi)$ on scales up to 20 Mpc. Although the signal-to-noise of this plot is not great, the general oval shape in correlation function and the hint of redshift space distortion at small r_p can be seen.

To reduce the effect of redshift space distortion to first order, the semi-projected correlation function $w_p(r_p)$ is calculated by integrating over the π direction, and is given by the expression

$$w_p(r_p) = 2 \int_0^\infty \xi(r_p, \pi) d\pi. \quad (5.4)$$

In practice the upper limit of integration is limited to ~ 50 Mpc, where the result converges to a stable value. Changing this limit has little effect on the final result. The resulted projected correlation function is shown in Figure 5.5, with logarithmic binning in r_p . A functional fit of the form $w_p(r_p) = r_p(r_p/r_{p,0})^{-\gamma}$ is fitted to the correlation function, and the best-fit parameters are found to be $r_{p,0} \sim 18.7 \pm 0.9$ Mpc and $\gamma \sim 1.81 \pm 0.07$. The errors are again estimated by jackknife resampling.

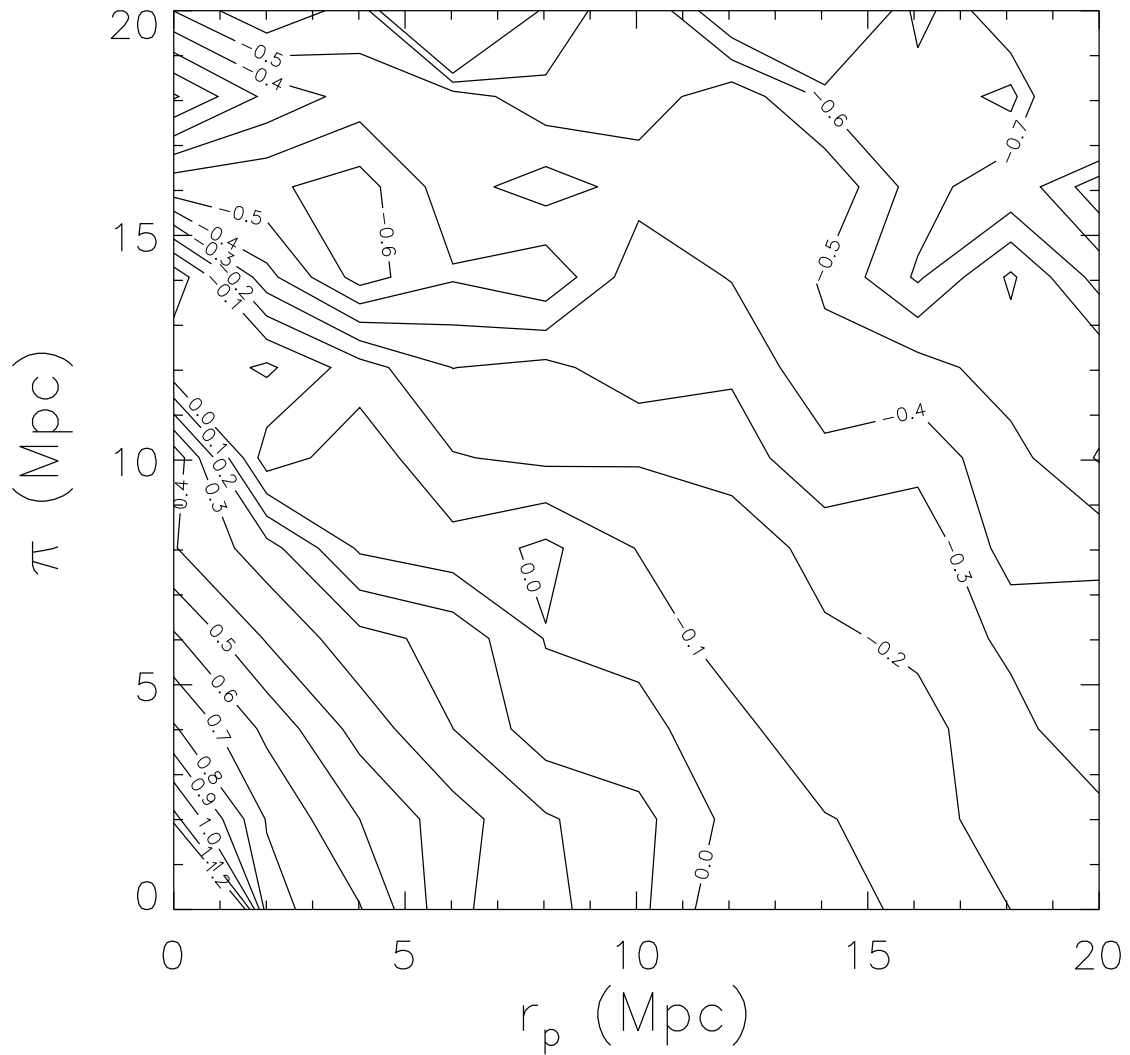


Figure 5.4 Contour showing the two-dimensional cross-correlation function between the CMASS-selected post-starburst galaxies and the CMASS galaxy sample. The grid of r_p and π used to calculate this is linear. The contour lines are chosen to be linear in $\log \xi$, and labeled with corresponding values of $\log \xi$.

3.3 Real-space Correlation Function

Following Davis & Peebles (1983), the real-space correlation function, once a functional form is assumed, can be inferred from the measured semi-projected correlation function. This can be done as follows.

The projected correlation function can be written in term of the measured two-dimensional correlation function as

$$w_p(r_p) = 2 \int_0^\infty \xi(r_p, \pi) d\pi \quad (5.5)$$

$$= 2 \int_{r_p}^\infty \frac{r\xi(r) dr}{\sqrt{r^2 - r_p^2}}, \quad (5.6)$$

where the second line is obtained by coordinate transformation to replace the line-of-sight and transverse distance π and r_p to the real-space distance r .

If the real-space correlation function is assumed to take a power-law form $\xi = (r/r_0)^{-\gamma}$, then the integral in equation 5.6 can be performed analytically. The result can be shown to be

$$w_p(r_p) = r_p \frac{\Gamma\left(\frac{1}{2}\right) \Gamma\left(\frac{\gamma-1}{2}\right)}{\Gamma\left(\frac{\gamma}{2}\right)} \left(\frac{r_p}{r_0}\right)^{-\gamma}. \quad (5.7)$$

The measured projected correlation function was fitted with the functional form $w_p(r_p) = r_p(r_p/r_{p,0})^{-\gamma}$, where $r_{p,0} = 18.7 \pm 0.9$ Mpc and $\gamma = 1.81 \pm 0.07$ respectively. These two expressions can be compared to the analytical result in equation 5.7 to obtain the correlation scale length in real-space to be $r_0 = 9.15 \pm 0.53$ Mpc.

To put these numbers in context, we compare them to various other clustering measurements from other galaxy and QSO samples. In early days of this field, Davis & Peebles (1983) found the clustering signal for the galaxies in the CfA redshift survey at low redshift to be well-described by $r_0 \sim 7.7$ Mpc with $\gamma \sim 1.77$. Guo et al. (2013) found $r_0 \sim 11.3$ Mpc with $\gamma \sim 1.85$ for the autocorrelation measurement of CMASS galaxy sample from the SDSS DR9. Mountrichas et al. (2009) found $r_0 \sim 9.9$ Mpc and $\gamma \sim 1.75$ for the QSO-LRG cross-correlation between various QSO

samples (2SLAQ, 2QZ and SDSS) with the 2SLAQ LRG sample at redshift $z \sim 0.5$. Shen et al. (2013) found similar value of $r_0 \sim 9.4$ Mpc and $\gamma \sim 1.69$ in another study of cross-correlation between QSOs and early-type galaxies, with both samples from the SDSS. Tentatively, the values of r_0 and γ we measure in this work are crudely in the same ballpark as other works. It might be noted that the works that studied cross-correlation functions between QSOs and early-type galaxies (Mountrichas et al., 2009; Shen et al., 2013) have similar values of both parameters, which are quite different from the values found from autocorrelation of early-type galaxies (Guo et al., 2013). The sense of difference is that the QSO-LRG cross-correlation function has both r_0 and γ smaller than LRG autocorrelation. Since our values of r_0 and γ are more similar to the QSO-LRG cross-correlation studies, we suggest that the post-starburst galaxies might reside in dark matter halos similar to those of QSOs.

4 Evolution of Clustering Properties with Redshift

In addition to studying the clustering properties of the whole post-starburst galaxy sample, it would be interesting to study clustering properties as a function of redshift, and to detect any evolution in such properties. To do this, we split the galaxy samples into high-redshift and low-redshift bins. The redshift boundary between these two redshift bins is chosen at $z = 0.62$, which splits the post-starburst galaxy sample roughly in half. The CMASS galaxy sample and the mock sample are also split at the same redshift.

Redshift distributions of the CMASS-selected post-starburst galaxy sample and the parent CMASS sample are shown in Figure 5.1. It should be noted that the distributions are shifted with respect to each other, with post-starburst galaxies tending to be at higher redshifts. The reason for this is that the CMASS galaxies are selected with specific color selection designed to select an approximately mass-limited sample of early-type galaxies between redshift range $z \sim 0.4 - 0.6$. The post-starburst galaxies have intrinsically different SEDs, but can still leak into the CMASS color selection if at higher redshift, thus the difference in the redshift distributions. The fraction of CMASS galaxies that are also post-starburst galaxies is shown in the bottom panel of Figure 5.1 as a function of redshift. This ratio ranges from 0.1% at redshift $z \sim 0.4$ where CMASS

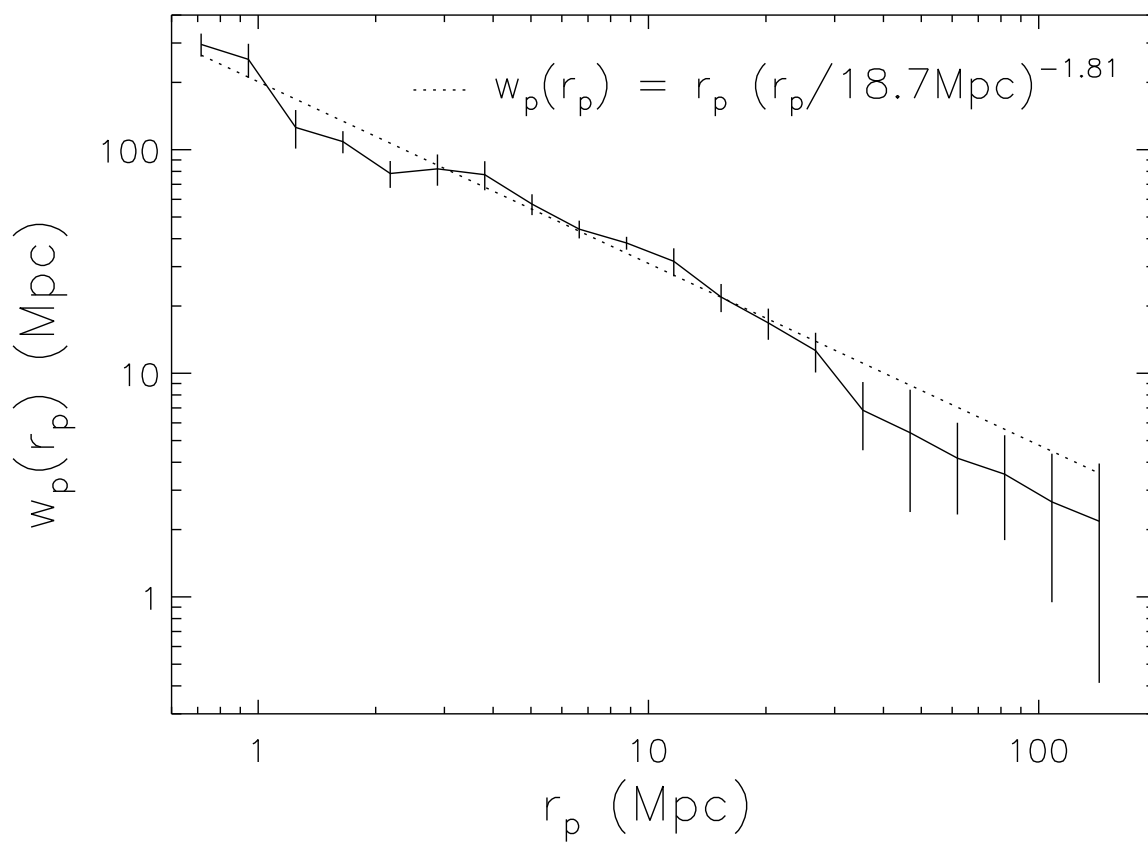


Figure 5.5 Semi-projected cross-correlation function between CMASS-selected post-starburst galaxies and CMASS galaxies. The dotted line shows the functional fit of the form $w_p(r_p) = r_p (r_p/r_{p,0})^{-\gamma}$, where the best-fit parameters are $r_{p,0} \sim 18.7 \pm 0.9$ Mpc and $\gamma \sim 1.81 \pm 0.07$.

distribution starts to rise, but post-starburst galaxies are still rare, to more than 10% at redshift $z \sim 0.9$ which is past the bulk of the CMASS sample, but still with relatively large number of post-starburst galaxies. By splitting the post-starburst galaxy sample in half, the higher redshift bin for CMASS galaxies would contain significantly smaller number of objects than the low redshift bin. However, since the CMASS sample has much larger number of objects than the post-starburst galaxy sample, we expect the number to still be sufficient for good statistics for the higher redshift bin.

The redshift-space cross-correlation functions between the post-starburst galaxy sample and the CMASS sample for two redshift bins and whole sample are calculated and shown in Figure 5.6, along with the respective power-law fits. The error bars are again calculated from jackknife resampling. Power laws of the form $\xi(s) = (s/s_0)^{-\gamma}$ are fitted to the correlation functions in both redshift bins, and the results are tabulated in Table 5.1. There is a hint that the high-redshift portion of the sample (red line) have consistently higher clustering measurement than the low-redshift portion (blue line), although the difference is smaller than the error bars. Therefore, we conclude that the clustering properties of post-starburst galaxies do not evolve with redshift significantly, at least not at the level we can distinguish given our error bars.

The semi-projected correlation functions for the two redshift bins are calculated from the two-dimensional correlation function as described in Section 3.2. The results are shown in Figure 5.7. It should be noted that for the high-redshift portion of the sample, two data points at small scales are missing. This is because some bins in (r_p, π) corresponding to these points have zero number of pairs, rendering the calculation invalid. This only happens at the high-redshift bin because, as shown in Figure 5.1, there are fewer CMASS galaxies in this redshift bin due to the difference in redshift distribution between the post-starburst galaxy and the CMASS galaxy sample. Power laws of the form $w_p(r_p) = r_p(r_p/r_{p,0})^{-\gamma}$ are fitted to both redshift bins, and the results are tabulated in Table 5.1. The projected correlation functions in the two redshift bins are almost identical within the error bars, without any weak hint seen in the redshift-space correlation that the higher redshift bin clusters more strongly than the lower redshift bin. It is also curious to note that in both the semi-projected correlation functions shown here, and the

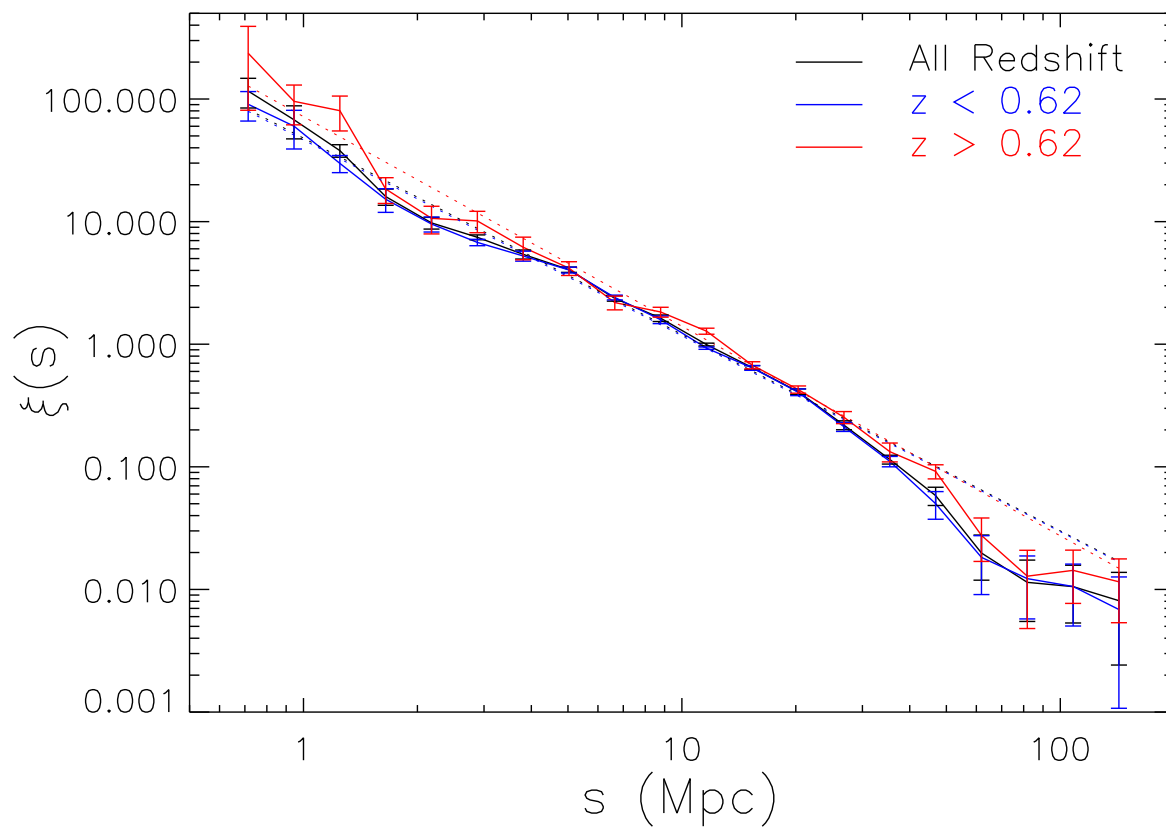


Figure 5.6 The redshift-space cross-correlation function of the CMASS-selected post-starburst galaxies with the CMASS galaxies separated into redshift bins (black: full sample, red: high redshift and blue: low redshift). The dotted lines of corresponding colors show the power-law fits to the cross-correlation functions.

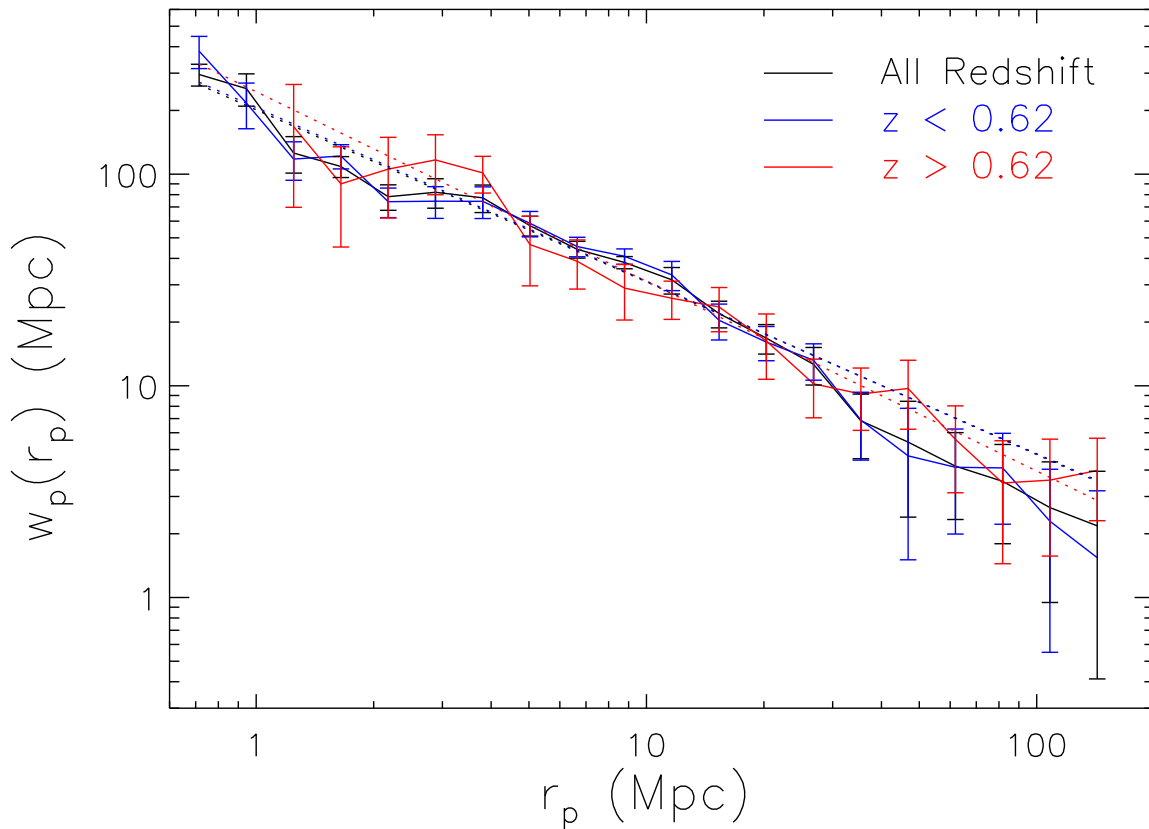


Figure 5.7 The semi-projected cross-correlation function of the CMASS-selected post-starburst galaxies with the CMASS galaxy sample separated into redshift bins. (black: full sample, red: high redshift and blue: low redshift). The dotted lines of corresponding colors show the power-law fits to the cross-correlation functions.

redshift-space correlation functions shown in Figure 5.6, the high-redshift bin has a slightly steeper power-law. This difference is small and insignificant given our large error bars.

We also calculate the real-space correlation function for different redshift bins from the measured semi-projected correlation functions, following the calculation shown in Section 3.3. This calculation assumes that the real-space correlation functions are represented by power-laws. The correlation lengths r_0 for each redshift bins are tabulated in Table 5.1. The correlation lengths between different redshift bins do not differ significantly, and are consistent with being constant to well within the error bars.

Redshift Range	$\xi(s) = (s/s_0)^{-\gamma}$		$w_p(r_p) = r_p(r_p/r_{p,0})^{-\gamma}$		$\xi = (r/r_0)^{-\gamma}$	
	s_0	γ	$r_{p,0}$	γ	r_0	γ
All z	11.2 ± 0.4	1.60 ± 0.04	18.7 ± 0.9	1.81 ± 0.07	9.15 ± 0.5	1.81 ± 0.07
$z < 0.62$	11.2 ± 0.5	1.59 ± 0.05	18.6 ± 1.1	1.82 ± 0.09	9.23 ± 0.7	1.82 ± 0.09
$z > 0.62$	12.1 ± 0.9	1.71 ± 0.09	18.2 ± 2.0	1.90 ± 0.15	9.58 ± 1.3	1.90 ± 0.15

Table 5.1

5 Bias and Dark Matter Halo Mass

Finally, with the semi-projected correlation function we can measure the linear bias of the post-starburst galaxy population and infer the dark matter halo mass they reside. We start with the expression for linear bias

$$w_{p,\text{PSG-CMASS}}(z = 0.62) = w_{p,\text{matter}}(z = 0.62) b_{\text{PSG-CMASS}}^2, \quad (5.8)$$

where $w_{p,\text{PSG-CMASS}}$ represents the semi-projected cross-correlation function that we measured in Section 3.2 at redshift $z = 0.62$ representative of the post-starburst galaxy sample, $w_{p,\text{matter}}$ the correlation function of underlying matter density at the same redshift, and $b_{\text{PSG-CMASS}}^2$ the linear bias. The linear bias factor can be written in terms of biases of the different population as

$$b_{\text{PSG-CMASS}}^2 = b_{\text{PSG}} b_{\text{CMASS}}. \quad (5.9)$$

In order to find the bias factor of the post-starburst galaxy population, we can compare the cross-correlation function to the CMASS autocorrelation function. In the same way, the CMASS autocorrelation can be written in terms of the bias of the CMASS population as

$$w_{p,\text{CMASS}}(z = 0.52) = w_{p,\text{matter}}(z = 0.52) b_{\text{CMASS}}^2, \quad (5.10)$$

where the equation is now written at redshift $z = 0.52$, which is the median for the CMASS galaxy population. We can now take the ratio of the equation 5.8 and 5.10 to get

$$b_{\text{PSG}} = b_{\text{CMASS}} \frac{w_{p,\text{matter}}(z = 0.52)}{w_{p,\text{matter}}(z = 0.62)} \frac{w_{p,\text{PSG-CMASS}}}{w_{p,\text{CMASS}}}. \quad (5.11)$$

The value of b_{CMASS} has been measured in the literature to be in the range $b_{\text{CMASS}} \sim 1.8 - 2.1$ (White et al., 2011; Nuza et al., 2013; Guo et al., 2013; Shen et al., 2013). The discrepancies between these values are largely due to different methodologies in obtaining the biases, and also to different galaxy weights assigned in some of these works for better BAO measurement. For our purpose, we take a fiducial value of CMASS linear bias to be $b_{\text{CMASS}} \sim 2.0 \pm 0.02$. The ratio between matter correlation functions at different redshift can be found from the growth factors of the matter power spectrum, given by

$$\frac{w_{p,\text{matter}}(z = 0.52)}{w_{p,\text{matter}}(z = 0.62)} = \frac{D^2(z = 0.52)}{D^2(z = 0.62)}, \quad (5.12)$$

where

$$D(z) = \frac{\int_0^{a(z)} [aH(a)]^{-3} da}{\int_0^1 [aH(a)]^{-3} da} \frac{H(z)}{70 \text{ kms}^{-1}\text{Mpc}^{-1}}. \quad (5.13)$$

Figure 5.8 shows the PSG-CMASS cross-correlation and the CMASS autocorrelation functions measured in the same way as described in Section 3.2. Following Shen et al. (2013), the ratio between these two is measured over the range $r_p = 5.7 - 22.9 \text{ Mpc}$ ($4 - 16 h^{-1}\text{Mpc}$). The reason for this range is that for scales smaller than $4 h^{-1}\text{Mpc}$, the bias is affected by non-linearity and the one-halo term, while on scales larger than $16 h^{-1}\text{Mpc}$, the residual redshift space distortion (RSD) starts to become important. This ratio is well-defined in this range since the two functions have similar power-law slopes, and is averaged over these 5 data points to be 0.79 ± 0.05 . With all the relevant ingredients we measure the linear bias factor for the post-starburst galaxy population at $z \sim 0.62$ to be $b_{\text{PSG}} = 1.74 \pm 0.11$.

Using the measured value of linear bias, we can estimate the associated dark matter halo mass. There are many ways to do this in the literature, ranging in sophistications from simple spherical collapse model to more realistic models with help of N-body simulations (Cole & Kaiser, 1989; Mo & White, 1996; Sheth & Tormen, 1999; Sheth et al., 2001; Tinker et al., 2010; Ma et al., 2011). The most common way to express the mapping between the bias b and the halo mass is through $b(\nu)$, where ν is the ‘‘peak height’’ in linear density field, defined as $\nu = \delta_c/\sigma(M)$. The parameter

δ_c is the critical density for collapse, and usually takes value of $\delta_c = 1.686$ based on the spherical collapse model. σ is the linear matter variance on the scale of the halo $R = (3M/4\pi\rho_m)^{1/3}$, defined as

$$\sigma^2(R) = \frac{1}{2\pi^2} \int P(k, z) \hat{W}^2(k, R) k^2 dk, \quad (5.14)$$

where $P(k, z)$ is the matter power spectrum at redshift z and $\hat{W}(k, R)$ is the Fourier transform of the top-hat window function of radius R . In this work, we use the $b(\nu)$ expression by Tinker et al. (2010)

$$b(\nu) = 1 - A \frac{\nu^a}{\nu^a + \delta_c^a} + B\nu^b + C\nu^c, \quad (5.15)$$

where A , a , B , b , C and c are fit parameters that best described the relationship found by simulations, and are written as $A = 1.0 + 0.24y \exp[-(4/y)^4]$, $a = 0.44y - 0.88$, $B = 0.183$, $b = 1.5$, $C = 0.019 + 0.107y + 0.19 \exp[-(4/y)^4]$, $c = 2.4$, and $y = \log_{10} \Delta$ where Δ is the virial value, which we used $\Delta = 200$ (i.e. the dark matter halo mass we calculate corresponds to the mass enclosed in the radius such that the average density is 200 times the mean matter density of the universe). Using this recipe, we convert our measured bias $b_{\text{PSG}} = 1.74 \pm 0.11$ to the corresponding dark matter halo mass of $M_{\text{halo}} \sim (1.6 \pm 0.3) \times 10^{13} M_{\odot}$.

6 Discussion and Conclusions

In this chapter, we explore the clustering properties of our post-starburst galaxy sample by calculating the cross-correlation between this sample and the BOSS CMASS galaxy sample. The cross-correlation is performed instead of the autocorrelation because of the low density of our sample, and the CMASS sample is used because it is in the same redshift range and is a parent sample where most of our post-starburst galaxies are spectroscopically selected.

We directly measure the redshift-space correlation function and the semi-projected correlation function between the two samples. Both correlation functions are fitted reasonably well with power laws. From the semi-projected correlation function, we calculated the clustering length r_0

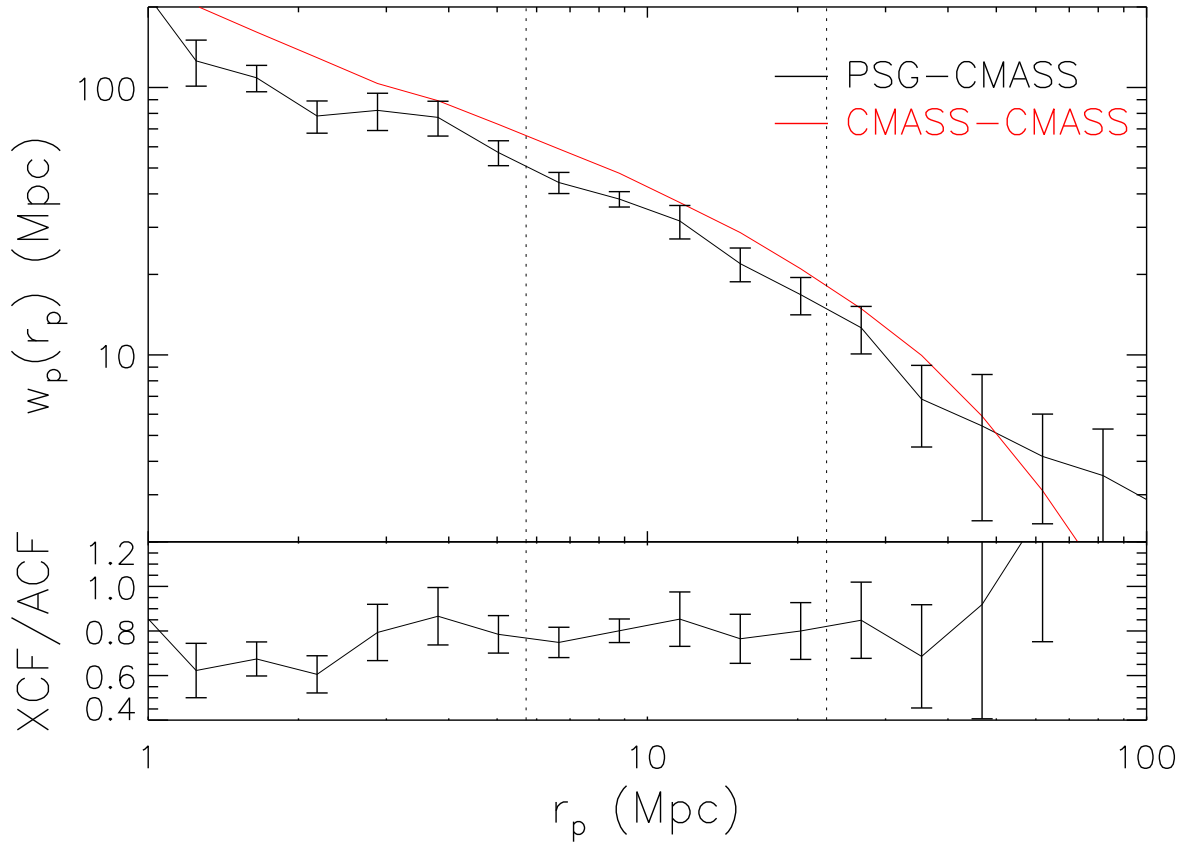


Figure 5.8 Top panel: the semi-projected cross-correlation function of the post-starburst galaxy sample with the CMASS sample (XCF; black, also shown in Figure 5.5), compared to the autocorrelation function of the CMASS sample (ACF; red). Bottom panel: the ratio between the cross-correlation and autocorrelation functions shown in the top panel. The two vertical lines denote the range $r_p = 5.7 - 22.9$ Mpc ($4 - 16 h^{-1}$ Mpc) used to find the average ratio between the two curves, which is used in calculating the linear bias of post-starburst galaxies (see text for details.)

and the power-law index γ of the real-space correlation function under the assumption that the real-space correlation function can be written as a power law. We found the values of these parameters to be $r_0 = 9.15 \pm 0.53$ Mpc and $\gamma = 1.81 \pm 0.07$ respectively.

We also explored the redshift evolution of the clustering properties by splitting the post-starburst galaxy sample into two equal-sized subsamples. The redshift cut separating the high-redshift and low-redshift bins is at $z = 0.62$. The correlation functions are calculated separately for the two subsamples, and to the size of the error bars, we found no significant difference in the clustering properties across these subsamples. However, in the redshift-space correlation function there is a slight hint that the high-redshift bin might be more strongly clustered on all scale, although the difference is well within the uncertainty. If this difference is true, the difference would be consistent with the expectation that the equal-size peaks in density field are more strongly clustered at higher redshift. In order for this explanation to hold, we have to assume that the dark matter halos in which the post-starburst galaxies reside do not change significantly over the same redshift range. Overall, the redshift evolution, if there is any, is too small to be distinguished given our relatively large error bars, and we cannot draw any strong conclusions.

Finally, we calculate the linear clustering bias of the post-starburst galaxy sample by comparing the cross-correlation function between post-starburst galaxies and CMASS galaxies to the autocorrelation function of the CMASS population. We found the linear bias factor to be $b_{\text{PSG}} = 1.74 \pm 0.11$. This value of linear bias at the redshift of the post-starburst galaxy sample ($z = 0.62$) corresponds to a dark matter halo mass of about $M_{\text{halo}} \sim (1.6 \pm 0.3) \times 10^{13} M_{\odot}$.

Bibliography

Bardeen, J. M., Bond, J. R., Kaiser, N., & Szalay, A. S. 1986, ApJ, 304, 15

Cole, S. & Kaiser, N. 1989, MNRAS, 237, 1127

Davis, M., Efstathiou, G., Frenk, C. S., & White, S. D. M. 1985, ApJ, 292, 371

Davis, M. & Peebles, P. J. E. 1983, ApJ, 267, 465

- Delubac, T., Bautista, J. E., Busca, N. G., Rich, J., Kirkby, D., Bailey, S., Font-Ribera, A., Slosar, A., Lee, K.-G., Pieri, M. M., Hamilton, J.-C., Aubourg, É., Blomqvist, M., Bovy, J., Brinkmann, J., Carithers, W., Dawson, K. S., Eisenstein, D. J., Gontcho, S. G. A., Kneib, J.-P., Le Goff, J.-M., Margala, D., Miralda-Escudé, J., Myers, A. D., Nichol, R. C., Noterdaeme, P., O'Connell, R., Olmstead, M. D., Palanque-Delabrouille, N., Pâris, I., Petitjean, P., Ross, N. P., Rossi, G., Schlegel, D. J., Schneider, D. P., Weinberg, D. H., Yèche, C., & York, D. G. 2015, *A&A*, 574, A59
- Eisenstein, D. J., Annis, J., Gunn, J. E., Szalay, A. S., Connolly, A. J., Nichol, R. C., Bahcall, N. A., Bernardi, M., Burles, S., Castander, F. J., Fukugita, M., Hogg, D. W., Ivezić, Ž., Knapp, G. R., Lupton, R. H., Narayanan, V., Postman, M., Reichart, D. E., Richmond, M., Schneider, D. P., Schlegel, D. J., Strauss, M. A., SubbaRao, M., Tucker, D. L., Vanden Berk, D., Vogeley, M. S., Weinberg, D. H., & Yanny, B. 2001, *AJ*, 122, 2267
- Eisenstein, D. J., Hu, W., Silk, J., & Szalay, A. S. 1998a, *ApJ*, 494, L1
- Eisenstein, D. J., Hu, W., & Tegmark, M. 1998b, *ApJ*, 504, L57
- Glazebrook, K. & Blake, C. 2005, *ApJ*, 631, 1
- Guo, H., Zehavi, I., Zheng, Z., Weinberg, D. H., Berlind, A. A., Blanton, M., Chen, Y., Eisenstein, D. J., Ho, S., Kazin, E., Manera, M., Maraston, C., McBride, C. K., Nuza, S. E., Padmanabhan, N., Parejko, J. K., Percival, W. J., Ross, A. J., Ross, N. P., Samushia, L., Sánchez, A. G., Schlegel, D. J., Schneider, D. P., Skibba, R. A., Swanson, M. E. C., Tinker, J. L., Tojeiro, R., Wake, D. A., White, M., Bahcall, N. A., Bizyaev, D., Brewington, H., Bundy, K., da Costa, L. N. A., Ebelke, G., Malanushenko, E., Malanushenko, V., Oravetz, D., Rossi, G., Simmons, A., Snedden, S., Streblyanska, A., & Thomas, D. 2013, *ApJ*, 767, 122
- Hinshaw, G., Larson, D., Komatsu, E., Spergel, D. N., Bennett, C. L., Dunkley, J., Nolte, M. R., Halpern, M., Hill, R. S., Odegard, N., Page, L., Smith, K. M., Weiland, J. L., Gold, B., Jarosik, N., Kogut, A., Limon, M., Meyer, S. S., Tucker, G. S., Wollack, E., & Wright, E. L. 2013, *ApJS*, 208, 19

- Kaiser, N. 1984, *ApJ*, 284, L9
- Ma, C.-P., Maggiore, M., Riotto, A., & Zhang, J. 2011, *MNRAS*, 411, 2644
- Mo, H. J. & White, S. D. M. 1996, *MNRAS*, 282, 347
- Mountrichas, G., Sawangwit, U., Shanks, T., Croom, S. M., Schneider, D. P., Myers, A. D., & Pimblet, K. 2009, *MNRAS*, 394, 2050
- Myers, A. D., Brunner, R. J., Richards, G. T., Nichol, R. C., Schneider, D. P., & Bahcall, N. A. 2007, *ApJ*, 658, 99
- Nuza, S. E., Sánchez, A. G., Prada, F., Klypin, A., Schlegel, D. J., Gottlöber, S., Montero-Dorta, A. D., Manera, M., McBride, C. K., Ross, A. J., Angulo, R., Blanton, M., Bolton, A., Favole, G., Samushia, L., Montesano, F., Percival, W. J., Padmanabhan, N., Steinmetz, M., Tinker, J., Skibba, R., Schneider, D. P., Guo, H., Zehavi, I., Zheng, Z., Bizyaev, D., Malanushenko, O., Malanushenko, V., Oravetz, A. E., Oravetz, D. J., & Shelden, A. C. 2013, *MNRAS*, 432, 743
- Planck Collaboration, Ade, P. A. R., Aghanim, N., Armitage-Caplan, C., Arnaud, M., Ashdown, M., Atrio-Barandela, F., Aumont, J., Baccigalupi, C., Banday, A. J., & et al. 2014, *A&A*, 571, A16
- Planck Collaboration, Ade, P. A. R., Aghanim, N., Arnaud, M., Ashdown, M., Aumont, J., Baccigalupi, C., Banday, A. J., Barreiro, R. B., Bartlett, J. G., & et al. 2015, *ArXiv e-prints*
- Sánchez, A. G., Baugh, C. M., & Angulo, R. E. 2008, *MNRAS*, 390, 1470
- Shen, Y., McBride, C. K., White, M., Zheng, Z., Myers, A. D., Guo, H., Kirkpatrick, J. A., Padmanabhan, N., Parejko, J. K., Ross, N. P., Schlegel, D. J., Schneider, D. P., Streblyanska, A., Swanson, M. E. C., Zehavi, I., Pan, K., Bizyaev, D., Brewington, H., Ebelke, G., Malanushenko, V., Malanushenko, E., Oravetz, D., Simmons, A., & Snedden, S. 2013, *ApJ*, 778, 98
- Sheth, R. K., Mo, H. J., & Tormen, G. 2001, *MNRAS*, 323, 1

Sheth, R. K. & Tormen, G. 1999, MNRAS, 308, 119

Slosar, A., Font-Ribera, A., Pieri, M. M., Rich, J., Le Goff, J.-M., Aubourg, É., Brinkmann, J., Busca, N., Carithers, B., Charlassier, R., Cortês, M., Croft, R., Dawson, K. S., Eisenstein, D., Hamilton, J.-C., Ho, S., Lee, K.-G., Lupton, R., McDonald, P., Medolin, B., Muna, D., Miralda-Escudé, J., Myers, A. D., Nichol, R. C., Palanque-Delabrouille, N., Pâris, I., Petitjean, P., Piškur, Y., Rollinde, E., Ross, N. P., Schlegel, D. J., Schneider, D. P., Sheldon, E., Weaver, B. A., Weinberg, D. H., Yèche, C., & York, D. G. 2011, *J. Cosmology Astropart. Phys.*, 9, 1

Spergel, D. N., Verde, L., Peiris, H. V., Komatsu, E., Nolta, M. R., Bennett, C. L., Halpern, M., Hinshaw, G., Jarosik, N., Kogut, A., Limon, M., Meyer, S. S., Page, L., Tucker, G. S., Weiland, J. L., Wollack, E., & Wright, E. L. 2003, *ApJS*, 148, 175

Tegmark, M., Eisenstein, D. J., Strauss, M. A., Weinberg, D. H., Blanton, M. R., Frieman, J. A., Fukugita, M., Gunn, J. E., Hamilton, A. J. S., Knapp, G. R., Nichol, R. C., Ostriker, J. P., Padmanabhan, N., Percival, W. J., Schlegel, D. J., Schneider, D. P., Scoccimarro, R., Seljak, U., Seo, H.-J., Swanson, M., Szalay, A. S., Vogeley, M. S., Yoo, J., Zehavi, I., Abazajian, K., Anderson, S. F., Annis, J., Bahcall, N. A., Bassett, B., Berlind, A., Brinkmann, J., Budavari, T., Castander, F., Connolly, A., Csabai, I., Doi, M., Finkbeiner, D. P., Gillespie, B., Glazebrook, K., Hennessy, G. S., Hogg, D. W., Ivezić, Ž., Jain, B., Johnston, D., Kent, S., Lamb, D. Q., Lee, B. C., Lin, H., Loveday, J., Lupton, R. H., Munn, J. A., Pan, K., Park, C., Peoples, J., Pier, J. R., Pope, A., Richmond, M., Rockosi, C., Scranton, R., Sheth, R. K., Stebbins, A., Stoughton, C., Szapudi, I., Tucker, D. L., vanden Berk, D. E., Yanny, B., & York, D. G. 2006, *Phys. Rev. D*, 74, 123507

Tinker, J. L., Robertson, B. E., Kravtsov, A. V., Klypin, A., Warren, M. S., Yepes, G., & Gottlöber, S. 2010, *ApJ*, 724, 878

White, M., Blanton, M., Bolton, A., Schlegel, D., Tinker, J., Berlind, A., da Costa, L., Kazin, E., Lin, Y.-T., Maia, M., McBride, C. K., Padmanabhan, N., Parejko, J., Percival, W., Prada, F., Ramos, B., Sheldon, E., de Simoni, F., Skibba, R., Thomas, D., Wake, D., Zehavi, I., Zheng, Z.,

- Nichol, R., Schneider, D. P., Strauss, M. A., Weaver, B. A., & Weinberg, D. H. 2011, *ApJ*, 728, 126
- Zehavi, I., Weinberg, D. H., Zheng, Z., Berlind, A. A., Frieman, J. A., Scoccamarro, R., Sheth, R. K., Blanton, M. R., Tegmark, M., Mo, H. J., Bahcall, N. A., Brinkmann, J., Burles, S., Csabai, I., Fukugita, M., Gunn, J. E., Lamb, D. Q., Loveday, J., Lupton, R. H., Meiksin, A., Munn, J. A., Nichol, R. C., Schlegel, D., Schneider, D. P., SubbaRao, M., Szalay, A. S., Uomoto, A., York, D. G., & SDSS Collaboration. 2004, *ApJ*, 608, 16
- Zehavi, I., Zheng, Z., Weinberg, D. H., Blanton, M. R., Bahcall, N. A., Berlind, A. A., Brinkmann, J., Frieman, J. A., Gunn, J. E., Lupton, R. H., Nichol, R. C., Percival, W. J., Schneider, D. P., Skibba, R. A., Strauss, M. A., Tegmark, M., & York, D. G. 2011, *ApJ*, 736, 59